Characterisations of EM Waves in Canonical structures with Radomes or Coating Shells

Li Zhong-Cheng

A Thesis Submitted

for the Degree of Doctor of Philosophy

Department of electrical and Computer Engineering

National University of Sinapore

2009

Acknowledgments

I would like to take this opportunity to convey my deepest and sincere gratitude to people without whom I would not have completed this project successfully.

First of all, I wish to extend my heartfelt appreciation to my project main supervisor Professor Li Le-Wei and co-supervisor Professor Leong Mook-Seng for their invaluable contributions and guidance throughout the entire course of the project. Special thanks to my immediate project supervisor Professor Li Le-Wei for his patient guidance and encouragement in times of overcoming difficulties, to which I am very grateful. I would also like to sincerely thank other faculty staff members from Microwave and RF group: Professor Yeo Tat-Soon and Associate Professor Ooi Ban-Leong for their help and suggestions.

Secondly, I would like to thank the supporting staff in NUS Microwave and RF group: Mr. Sing Cheng-Hiong and Mr. Ng Chin Hock. With their kind help and support, it is thus possible for me to carry out the research and obtain good results of simulations in this thesis. In addition, I would like to thank all my friends in NUS Microwave Research Lab for their invaluable advice and assistance. It is my great pleasure to work with them in the past six years. I am grateful to Dr. Sun Jin, Mr.

Wang Yao-Jun, Mr. Pan Shu-Jun, Mr. Chen Yuan, Mr. Lu Lu, Mr. Yao Ji-Jun, Dr. Gao Yuan, Dr. Ewe Wei-Bin, Dr. Ng Tiong-Hua and Mr. She Hao-Yuan for being my most reliable consultants.

Last but not least, I would like to thank my family members who had been a constant source of encouragement especially during the most difficult period of the project. Specifically I would like to thank my wife, Huang Yan, whose kindness, patience and support help me get through the hardest time and make my life more meaningful.

Contents

Acknowledgments **i**

Contents **iii**

Summary **viii**

List of Figures **xi**

List of Tables **xv**

1 Introduction **1**

1.1 Background 2

1.2 Motivation for the Project 8

1.3 Concept Outline 11

1.4 Layout of the Thesis 15

1.5 Publications 16

1.5.1 Journal Papers 17

1.5.2 Conference Presentations 18

2 A 3D Discrete Analysis of Cylindrical Radome Using DGF's 19

2.1 Introduction 20

2.2 Formulation of the Discrete Method 23

2.2.1 Concept Outline 23

2.2.2 Application of the Dyadic Green's Functions 24

2.2.3 Unbounded Dyadic Green's Functions 26

2.2.4 Scattered Dyadic Green's Functions 28

2.2.5 Correction Factor 29

2.2.6 Equivalent Current Source 31

2.2.7 Transmitted Field 31

2.3 Application to 2D Elliptical Radome 32

2.3.1 Implementation 32

2.3.2 Numerical Results 34

2.4 Discussion 35

2.5 Conclusions 44

3 Discrete Analysis of a 3D Airborne Radome of Superspheroidal Shapes 45

3.1 Introduction 46

3.2 Formulation of the Problem 47

3.2.1 Concept Outline 48

3.2.2 Analysis of a 3D Superspheroidal Radome 48

3.2.3 General Formulation of the Electromagnetic Fields 51

3.2.4 Boundary Condition and the Method of Moments 54

3.3 Numerical Results 56

3.4 Conclusions 59

4 Radiation Due to an Infinitely Transmission Line Near a Dielectric Elliptical Waveguide 60

4.1 Introduction 61

4.2 Coordinate System and Mathematical Functions 63

4.3 Dyadic Green's Functions 67

4.4 Equations Satisfied by Scattering Coefficients 71

4.5 Far Field Expressions 75

4.6 Numerical Results 77

4.7 Conclusions 85

5 Closed-Form Eigenfrequencies in Prolate Spheroidal Conducting Cavity 88

5.1 Introduction 89

5.2 Spheroidal Coordinates and Spheroidal Harmonics 90

5.3 Theory and Formulation 92

5.3.1 Background Theory 92

5.3.2 Derivation 93

5.4 Numerical Results for TE Modes 96

5.4.1 Numerical Calculation 96

5.4.2 Results and Comparison 99

5.5 Numerical Results for TM Modes 102

5.5.1 Numerical Calculation 102

5.5.2 Results and Comparison 103

5.6 Conclusion and Discussion 104

6 A New Closed Form Solution to Light Scattering by Spherical Nanoshells 108

6.1 Introduction 109

6.2 Basic Formulas 112

6.3 New Closed Form Solution to Intermediate Coefficients A_n and B_n . . 117

6.3.1 Approximate Expression of Coefficient A_n 118

6.3.2 Approximate Expression of Coefficient B_n 120

6.3.3 Validations and Accuracy 122

6.4 New Closed Form Solutions to Scattering Coefficients a_n and b_n . . . 123

6.4.1 Approximate Expression of Coefficient a_n 123

6.4.2 Approximate Expression of Coefficient b_n 134

6.5 Discussions and Conclusions 135

7 Conclusions and Future Work 138

Summary

In this thesis, a new discrete method, by making use of cylindrical dyadic Green's functions, has been presented in the study of electromagnetic transmission through a cylindrical radome having arbitrary cross sections. By virtue of using the dyadic Green's functions, this method takes into consideration the curvature effect of the radome's layer, which is partially ignored in classical approaches such as the ray-tracing method and the plane wave spectrum analysis. Numerical results are compared with those obtained using the plane wave spectrum method and model cylindrical wave-spectrum method.

Also outlined in this thesis is the concept of the Method of Moments(MoM) applied to study electromagnetic transmission through a superspheroidal radome with dielectric layer. By means of the inner product, the method effectively takes into account the continuity of the surface, instead of discretizing it as in the MoM. This proposed method is thus able to make a more accurate analysis of the electromagnetic transmission problem with a superspheroidal radome. Numerical results on the far field radiation pattern are obtained for various geometrical parameters of the superspheroidal radome, and also compared.

Next, electromagnetic radiation by an infinitely long transmission line analyzed using the dyadic Green's function technique is presented. The transmisison line is located in the vicinity of an elliptic dielectric waveguide. The dyadic Green's functions inside and outside of the elliptic waveguide are formulated first in terms of the elliptical vector wave functions which are in turn expressed as Mathieu functions. Using the boundary conditions, we derived a set of general equations governing the scattering and transmitting coefficients of the dyadic Green's functions. From the integral equations, the scattered and total electric fields in far-zone are then derived analytically and computed numerically.

An efficient approach is also proposed to analyse the interior boundary value problem in a spheroidal cavity with perfectly conducting wall. Then a closed-form solution has been obtained for the eigenfrequencies based on TE and TM cases. By means of least squares fitting technique, the values of the coefficients are determined numerically.

Finally, a new set of closed form expressions of the classic Mie scattering coefficients of a spherical nanoshell using a power series up to order 6. This set of approximate expressions is found to be very accurate in the large range of various potential engineering applications including optical nanoparticle characterizations and other nanotechnology applications, validated step by step along the derivation procedure. Computations using this closed form solutions are very fast and accurate for both lossy and lossless media, and requires very little effort in the calculations of the cross section results. Although examples are limited to nano-scattered appli-

cations, the general theory is applicable to a large frequency spectrum ranging from radio frequency waves to optical waves.

List of Figures

2.1 Illustrating the discretization of a radome. 24

2.2 Geometry of the elliptical radome used in the study. 33

2.3 Radiation pattern for $\epsilon_n = 1$ 34

2.4 Radiation patterns for various thicknesses at a scan angle of 0^o. . . . 36

2.5 Radiation patterns for various thicknesses at a scan angle of 6^o. . . . 36

2.6 Radiation patterns for various thicknesses at a scan angle of 18^o. . . . 37

2.7 Radiation patterns for various thicknesses at a scan angle of 24^o. . . . 37

2.8 Boresight error for a thickness of λ. 38

2.9 Peak-gain attenuation for a thickness of λ. 38

2.10 Boresight error for a thickness of 2λ. 39

2.11 Peak-gain attenuation for a thickness of 2λ. 39

2.12 Radiation pattern for a thickness of λ at a scan angle of 0^o. 40

2.13 Radiation pattern for a thickness of λ at a scan angle of 6^o. 40

2.14 Radiation pattern for a thickness of λ at a scan angle of 18^o. 41

2.15 Radiation pattern for a thickness of λ at a scan angle of 24^o. 41

3.1 Geometry of the elliptical radome used in the study. 49

3.2 Comparison of the MoM result with the exact result for the radiation pattern of a dipole array with a spherical dielectric shell. 57

3.3 Comparison of the MoM result with the AIM result for the radiation pattern of a dipole array with an ogive radome. 57

3.4 Boresight error for various thickness of radome. 58

3.5 Peak-gain attenuations for various thickness of radome. 58

4.1 A cross section view of the elliptical coordinate system. 63

4.2 Radiation by an infinitely long transmission line in the presence of an elliptical dielectric cylinder. 64

4.3 Normalized scattered and total electric fields for $u_s = 2a$, $\epsilon_r = 2.0$ and $\alpha = 180^o$. 79

4.4 Normalized scattered and total electric fields for $u_s = 2a$, $\epsilon_r = 2.0 + i2.0$ and $\alpha = 180^o$. 81

4.5 Normalized scattered and total electric fields for $u_s = 1.2a$, $\epsilon_r = 2.0$ and $\alpha = 180^o$. 82

4.6 Normalized scattered and total electric fields for $u_s = 2b$, $\epsilon_r = 2.0$ and $\alpha = 270^o$. 84

4.7 Normalized scattered and total electric fields for $u_s = 1.2b$, $\epsilon_r = 2.0$ and $\alpha = 270^o$. 86

5.1 Prolate spheroidal coordinates (η, ξ, ϕ) and a conducting cavity. . . . 90

5.2 The values of $c\xi$ (vertical axis) satisfying (i) $R_{11}^{(1)}(c, \xi) = 0$ and (ii) the fitted equation with g_0, g_1 and g_2 determined against ξ (horizontal axis). 99

5.3 The values of $c\xi$ (vertical axis) satisfying (i) $\partial/(\partial\xi)(R_{11}^{(1)}(c, \xi)\sqrt{\xi^2 - 1}) = 0$ and (ii) the fitted equation with g_0, g_1 and g_2 determined against ξ (horizontal axis). 104

6.1 Geometry of light scattering by a spherical nanoshell in hosting medium. 112

6.2 The relative errors of coefficients A_1, A_2, and B_1 obtained in this paper and also in Ref. [59], all compared with the exact solution obtained using the Mie scattering theory. The bullet-dotted curve "$--\bullet--$" denotes the results in [59] while the solid curve "——" stands for the result in this chapter. 124

6.3 The exact coefficient a_1 versus the spherical core radius $x \in (0.01, 1.0)$ and the spherical nanoshell thickness $t \in (0.01, 0.4)$. The other electrical parameters are $\epsilon_1 = (5.44/1.78)\epsilon_0$, $\epsilon_3 = \epsilon_0$, and $\epsilon_2 = (\epsilon_1 + \epsilon_3)/2$ while $\mu_1 = \mu_2 = \mu_3 = \mu_0$. 128

6.4 The relative errors of approximate coefficient a_1 formulas derived here in this chapter and in the existing work [59] versus the spherical core radius $x \in (0.01, 1.0)$ and the spherical nanoshell thickness $t \in (0.01, 0.4)$. 131

6.5 The variation of $|a_2|$ and the relative errors of the formulas derived in this chapter and in the existing work [59] versus the spherical core radius $x \in (0.01, 1.0)$ and the spherical nanoshell thickness $t \in (0.01, 0.4)$. 133

6.6 The relative errors of the formulas $|b_1|$ derived in this chapter and in the existing work [59] versus the spherical core radius $x \in (0.01, 1.0)$ and the spherical nanoshell thickness $t \in (0.01, 0.4)$. 136

List of Tables

5.1 Expansion Coefficients g_0, g_1, g_2, and g_3 for TE_{ns0} Modes ($s = 1$, 2, and 3) 100

5.2 Expansion Coefficients g_0, g_1, g_2, and g_3 for TE_{ns0} Modes ($s = 4$, 5, and 6) 101

5.3 Expansion Coefficients g_0, g_1, g_2, and g_3 for TM_{ns0} Modes ($s = 1$, 2, and 3) 105

5.4 Expansion Coefficients g_0, g_1, g_2, and g_3 for TM_{ns0} Modes ($s = 4$, 5, and 6) 106

Chapter 1

Introduction

In this thesis, new methods or concepts have been proposed to analyze some specifically shaped canonical objects. One method is proposed to analyze transmission effects of the electromagnetic field through a cylinder radome whose cross-section can be non-circular. The other method, which makes use of the spherical dyadic Green's functions (DGF's), is developed to study the electromagnetic transmission through an axis-symmetric radome of superspheroidal shapes. Next, the elliptical dyadic Green's function technique has been employed to characterize electromagnetic radiation of an imposed current line source in the presence of a two layered isotropic dielectric elliptical cylinder. Then, an efficient approach is proposed to analyse the interior boundary value problem in a spheroidal cavity with perfectly conducting wall. Finally, a new set of closed form expressions of the classic Mie scattering coefficients of a spherical nanoshell is derived a power series. To start off this introductory chapter, a brief background on the antenna-radome problem and on the existing methods that had been used in analyzing such a problem are

discussed. After which the motivation for this project will be highlighted. This is followed by a brief presentation on the outline of the concepts or methods used in this project. At the end of this chapter, the organization layout of the remaining part of the thesis will be given.

1.1 Background

Airborne radar antennas are enclosed in dielectric radomes for protection from a variety of environmental and aerodynamic effects. The geometry of airborne radome, being largely determined by aerodynamic considerations, often leads to degradation of the electromagnetic performance of any enclosed antenna. A good design of antenna radome system can minimize such undesirable effects. This relies on an accurate analysis of the effect of a radome on the penetration of electromagnetic wave. A radome is a dielectric shell that protects the radar antenna while at the same time tries not to interfere with its operation [1]. Ideally the radome should appear transparent to radio frequency so as not to degrade the electrical performance of the enclosed antenna. Unfortunately, due to a dielectric shell that encloses the antenna, it is inevitable that the wavefront of the electromagnetic wave from the antenna will be distorted by the radome. This distortion would cause the radome to adversely affect the operation of the radar system that it intends to protect. For example, the radome can produce boresight error, which is an apparent change in the angular position of a radar source or target. In a modern radar system, a small boresight error may result in a serious degradation of the radar's performance.

In addition, part of the radiation energy is lost as a consequence of the scattering of electromagnetic wave from the radome surface. This will result in peak-gain attenuation, which is the loss of peak gain. As a consequence of these two effects, a radome can reduce both the accuracy in determining the angular position of a target and the range at which the target can be detected. The boresight error and the peak-gain attenuation are therefore usually the electrical parameters that are of greatest concern in any radome design. These two parameters can be obtained by knowing the characteristic of the electromagnetic field both inside and outside the radome. A radome can also change the sidelobe level of an antenna.

A precise analysis of radome performance is difficult, and nearly impossible in practice [2], because the general shape of a radome layer usually does not fit into a frame suitable for an exact analysis. This is especially so for an airborne radome in which, due to the need for aerodynamic requirements, it's shapes are not quite regular. For such a radome, there is no suitable frame that can be used for exact analysis. To analyze such a radome, one must resort to some approximation methods. The usual basic principle of approximation is to find a canonical configuration to approximate the surface of the dielectric layer locally, such that from this local point of view, the problem can be solved rigorously by analytic means. The accuracy of such an approximation depends on how closely the canonical problem resembles the original one.

In order to analyse accurately and improve the performance of the radome, there are many studies those have been done in this area [3]. One of the tradi-

tional techniques is the ray tracing method which traces a ray in the direction of propagation through the radome wall [4–6]. As a widely used method, it provides accurate results for large radomes, but becomes complicated and less accurate for rapidly curved shells which may have sharp edges or corners [7]. It makes use of many approximations, such as treating the radome wall at each intercept point as locally plane, and assuming that the inner and outer radome walls are parallel at the intercept point. As a result, the method has limited accuracy.

A closely related method is the Geometrical Optics (GO) method, which treats electromagnetic propagation as being "light-like" in behaviour. For large radomes, the method produces a good boresight error prediction accuracy, but it becomes largely inaccurate for radomes smaller than five wavelengths in diameter. This is because it makes the assumption that the electromagnetic wave propagates as a plane wave confined to a cylinder whose cross section the antenna aperture defines. However this is not true in practice.

A more accurate ray tracing method would be that of the Physical Optics (PO) technique [8, 9]. This method is based on the Huygen's principle which states that each point on a primary wavefront can be considered as a new source of secondary spherical waves, and that a secondary wavefront can be constructed at the envelope of these spherical waves. Hence the PO method can be employed in surface integration formulations that produce better accurate results than the GO method.

Beside the various ray tracing techniques, other methods include the plane-wave spectrum [10, 11], modal cylindrical-wave spectrum [12], and the Geometrical

theory of diffraction [13] each applying its own approximations to solve the radome problem. The finite element method was also used, where the radome does not affect the antenna current distribution, in order for the model to work [14]. For any of these approaches, the multiple scattering among the source, reflector and radome is ignored.

The method of moments (MoM) technique [15, 16] is understood to be more accurate than ray tracing as it takes into consideration any corners or edges on the surface of the radomes. This is possible as the surface of the radomes are approximated by numerous planar triangular patches [7,17]. This approach, due to the manipulation of large dimensional matrices where electric size of the problem is large, becomes computationally heavy, hence limiting its application to small radomes only. Giuseppe and Giorgio [18] proposed an alternative approach to the MoM technique when they computed the resistance of a dielectric-covered inclined series slot, but the loss in accuracy is thus encountered. Based on the MoM, the Conjugate Gradient - Fast Fourier Transform (CG-FFT) method [19,20] has a much lower memory requirement and accelerates its computations. This is because the use of the Fast Fourier Transform results in less operations required, and this in turn also leads to less errors associated with rounding off during computations.

Electromagnetic scattering of a normal incident plane wave by an elliptical cylinder was considered by Yeh [21] and Burke [22]. For the oblique incident case, the equations needed to solve for the scattering and transmission coefficients were formulated by Yeh [23]. The method in those works is to express the incident, scattered

and transmitted plane waves in terms of vector wave eigenfunctions obtained using the separation of variables method. These eigenfunctions are expressed usually in terms of Mathieu functions. The continuity boundary conditions were then implemented in determination of the coefficients in the scattered and transmitted waves. Numerical computations were presented in [21, 22, 24, 25] for the normal incident plane waves. For the oblique incident plane waves, numerical computations were presented by Kim [26]. Up to now, a generalized analysis of electromagnetic radiation problems involving dielectric elliptical cylinders has not been well-documented yet. This motivates the present work which considers electromagnetic radiation due to an infinitely transmission line near a dielectric elliptical cylinder.

Calculation of eigenfrequencies in electromagnetic cavities is useful in various applications such as the design of resonators. However, analytical calculation of these eigenfrequencies is severely limited by the boundary shape of these cavities. In this thesis, the interior boundary value problem in a prolate spheroidal cavity with perfectly conducting wall is solved analytically.

Light or electromagnetic scattering by composite spheres is another interest in the scientific and engineering communities [27–34]. Electromagnetic scattering by a plasma anisotropic sphere was analyzed [27]. The analysis was extended to Mie scattering by an uniaxial anisotropic sphere [28]. Furthermore, scattering by an inhomogeneous plasma anisotropic sphere of multilayers was also formulated and investigated [29]. It can be easily extended to light scattering by an inhomogeneous plasma anisotropic sphere where the exact solutions could be applied to obtain the

field distributions in the multilayered spherical structures. Along the analysis line of [27–29], the standard eigenfucntion expansion technique is utilized and the theory for the anisotropic media can still follow closely to theory used for the isotropic media. To characterize eigenvalues in the anisotropic media different from those in the isotropic media, potential formulation and parametric studies for scattering by rotationally symmetric anisotropic spheres were also carried out recently [30]. In addition, Sun discussed light scattering by coated sphere immersed in absorbing medium and compared finite-difference time-domain (FDTD) method with analytic solutions [31]. Scatterers consisting of concentric and nonconcentric multilayered spheres were also considered [32]. An improved algorithm for electromagnetic scattering of plane wave and shaped beams by multilayered spheres was developed [33] and the geometrical-optics approximation of forward scattering by coated particles was then discussed [34]. With new developments of nanoscience and nanotechnology, it becomes desirable to investigate the microcosmic world of the scattering problems. Nano-scaled objects have thus attracted considerable attentions recently, primarily because they have shown some interesting optical properties and are found to be important for modern photonic applications [35–38]. Nano-scaled metallic particles exhibit interesting optical characteristics and behave differently from those of normal-scaled dimensions. Interactions of collective and individual particles of metals (such as copper, silver and gold) were studied long time ago [39, 40]. Johnson and Christy plotted both the real and imaginary parts of relative permittivities of copper, silver and gold nanoparticles as a function of photon energy in a large range according to different frequencies [41].

1.2 Motivation for the Project

Over the past few decades, the dyadic Green's function technique has been widely employed to investigated the interaction of the electromagnetic waves with the layered media in the boundary-value problem [42, 43]. Dyadic Green's function is a very powerful technique for analyzing electromagnetic transmission through dielectric shell [42]. Li et al. [44–46] has derived the general expression of the dyadic Green's function for multi-layered planar medium, multi-layered spherical medium and multi-layered cylindrical medium. By using these dyadic Green's functions, we are able to obtain a rigorous analysis of the electromagnetic transmission problem through these media (i.e. planar, spherical and cylindrical). This includes the multiple reflection effects and the curvature effects of the mediums (spherical and cylindrical) which are taken care of by these dyadic Green's functions.

As the dyadic Green's functions are able to give a rigorous analysis of the transmission problem by taking curvature into consideration, it is therefore the intentions of this project to be able to make use of such a property of the dyadic Green's function in the analysis of the antenna-radome whose structure can be arbitrary. Unfortunately, for a radome in general, its dyadic Green's function cannot be obtained. This is because the shape of the radome will not fit into a suitable frame such that the derivation of its dyadic Green's function can be carried out. For the first method, the existing cylindrical dyadic Green's functions that had already been derived by Li et al. will be used in the analysis of a cylindrical radome of arbitrary cross-section. This will be done "indirectly" through some discretization of the radome surface. In

this way, the curvature effect of the radome surface can be accounted for and hence it will lead to a much better analysis of the antenna-radome problem as compared to the methods that uses the plane-slab approximation. The outline of this "discrete" method or concept is discussed in the next section.

As mentioned above, most of these methods involve some form of approximations in the process of solving the antenna-radome problem, like discretizing the surface into small components for easier analysis. For the second method, the method of moments is a unifying concept that is often applied to solve complex electromagnetic problems. Its basic idea is to reduce a functional equation to a matrix equation, and then to solve the matrix equation by known techniques. These techniques include point-matching, and approximate operators. The choice of the technique to be used depends largely on the problem set as well as the type of solutions desired. In the light of the ability of the method of moments to make a continuous instead of a discrete analysis of the antenna-radome problem, it will be interesting to make use of this property in our study of the far field radiation in the presence of a superspheroidal radome.

To obtain general characteristics of the electromagnetic radiation in the presence of dielectric elliptical cylinders, the dyadic Green's function is an important kernel of the integral equations [47–55]. Also, the dyadic Green's functions are quite important kernels used in numerical techniques such as the Method of Moments and the Boundary Element Method. The free space dyadic Green's function has already been available in terms of the elliptical vector wave functions. In this work,

the dyadic Green's functions for inside and outside of the elliptical cylinder are formulated first and the scattering superposition principle is employed. Then, the scattering coefficients of dyadic Green's functions are formulated by employing the boundary conditions.

For a spheroidal cavity, calculation of eigenfrequencies in electromagnetic cavities is useful in various applications such as the design of resonators. However, analytical calculation of these eigenfrequencies is severely limited by the boundary shape of these cavities. In this work, the interior boundary value problem in a prolate spheroidal cavity with perfectly conducting wall is solved analytically. By applying boundary conditions, it is possible to obtain an analytical expression of the base eigenfrequencies f_{ns0} using spheroidal wave functions [56, 57, 49] regardless of whether the parameter $c = kd/2$ is small or large where k denotes the wave number while d stands for the interfocal distance. An inspection of the plot of a series of f_{ns0} values (confirmed in [58]) indicates that variation of f_{ns0} with the coordinate parameter ξ is of the form $f_{ns0}(\xi) = f_{ns}(0)[1+g^{(1)}/\xi^2+g^{(2)}/\xi^4+g^{(3)}/\xi^6+\ \cdots]$ when c is small. By fitting the f_{ns0}, ξ evaluated onto an equation of its derived form, the first four expansion coefficients — $g^{(0)}$, $g^{(1)}$, $g^{(2)}$ and $g^{(3)}$ are determined numerically using the least squares method. The method used to obtain these coefficients is direct and simple, although the assumption of axial symmetry may restrict its applications to those eigenfrequencies $f_{nsm'}$, where $m' = 0$.

Recently, a closed form analytical model of the scattering cross section of a single spherical nanoshell has been considered [59], while some fine experimental works

were conducted in [60,61]. The results given in [59] seemed to agree with the exact solutions very well. Our recent careful investigations show that the relative errors in their results are not so small, especially when the electric size of the nano shell is not large. The present work is therefore to derive another different closed form solution for describing the light wave scattered by the nanoshells using a polynomial of up to order 6. Validation will be made by comparing the present closed form solution to the exact Mie scattering solution and also to the other closed form solution by Alam and Massoud.

1.3 Concept Outline

In this thesis, new methods or concepts are proposed in the analysis of radome.

One concept, which involves the use of the cylindrical dyadic Green's functions in the analysis of an arbitrary cylindrical radome with non-circular cross-section, is presented. Basically, the radome is first divided/discretized into several small sections. Each of these sections will then be modeled by an appropriate cylinder and the dyadic Green's functions corresponding to this cylinder will then be used to find the fields on the outer surface of these section which is also the outer surface of the radome. In other words, at each point on the radome, it is treated locally as belonging to some part of a circular cylinder. The dyadic Green's functions that characterized this circular cylinder is then used to find the fields that resides at the particular point on the outer surface of the circular cylinder at which the

section belongs to. In this way, the fields on the outer surface of the radome can be obtained but in discrete form. From these discrete fields, its equivalent discrete current sources can be easily found. Thus, the antenna-radome problem can then be effectively represented by this set of discrete equivalent current sources alone. From these equivalent current sources, the transmitted fields outside the radome can then be obtained via the unbounded dyadic Green's function. The radiation pattern of the transmitted antenna's field is then plotted from which the boresight error and peak-gain attenuation can be obtained.

The second concept is presented in this thesis, the electromagnetic fields in the inner and outer regions of the radomes, as well as that within the dielectric radome layer are first formulated in terms of the unbounded dyadic Green's function and the vector wave functions, together with unknown coefficients to be determined. Then by making use of the boundary conditions for the electromagnetic fields on both the inner and outer surfaces, a coupled set of integral equations are generated. These unknown coefficients are solved using the Method of Moments. Knowledge of the unknown coefficients will allow the determination of the far field radiation pattern.

The third concept, the dyadic Green's function technique has been employed to characterize electromagnetic radiation of an imposed current line source in the presence of an isotropic dielectric elliptical cylinder. The current density along the infinitely long wire has a constant amplitude but a varying phase. The elliptical cylinder is considered to be infinite in length. In order to analyze the problem, the dyadic Green's functions are expressed in terms of elliptical vector wave functions

and the general equations needed to solve for the reflection and transmission coefficients are derived from the boundary conditions. These derived equations are transformed into, and solved using, a linear equation system. Numerically, the radiation patterns of the infinitely long wire are computed, plotted, and shown for various cases where the position and distance of the line source are varied. Both lossy and lossless dielectric media for the elliptical cylinder are considered. The results are believed to be very useful to many practical problems, and especially to characterize cable radiation or transmission line power leakage in tunnels.

The fourth concept, an efficient approach is proposed to analyse the interior boundary value problem in a spheroidal cavity with perfectly conducting wall. Since the vector wave equations are not fully separable in spheroidal coordinates, it becomes necessary to double-check validity of the vector wave functions employed in analysis of the vector boundary problems. A closed-form solution has been obtained for the eigenfrequencies f_{ns0} based on TE and TM cases. From a series of numerical solutions for these eigenfrequencies, it is observed that the f_{ns0} varies with the parameter ξ among the spheroidal coordinates (η, ξ, ϕ) in the form of $f_{ns0}(\xi) = f_{ns}(0)[1+g^{(1)}/\xi^2+g^{(2)}/\xi^4+g^{(3)}/\xi^6+\cdots]$. By means of least squares fitting technique, the values of the coefficients, $g^{(1)}$, $g^{(2)}$, $g^{(3)}$, $\cdots$, are determined numerically. It provides analytical results, and fast computations, of the eigenfrequencies and the results are valid if ξ is large (e.g. , $\xi \geq 100$).

The last concept describes a new set of closed form expressions of the classic Mie scattering coefficients of a spherical nanoshell using a power series up to order 6.

This set of approximate expressions is found to be very accurate in the large range of various potential engineering applications including optical nanoparticle characterizations and other nanotechnology applications, validated step by step along the derivation procedure. Computations using the closed form solutions are very fast and accurate for both lossy and lossless media, but it requires very little effort in the calculations of the cross sections. Light or electromagnetic wave scattered by a single sphere or a coated sphere has been considered as a classic Mie theory. There have been some further extensions which were made further based on the Mie theory. Recently, a closed form analytical model of the scattering cross section of a single nanoshell has been considered. The present paper is documented further, based on the work in 2006 by Alam and Massoud, to derive another different closed form solution to the problem of light scattered by the nanoshells using polynomials of up to order 6. Validation is made by comparing the present closed form solution to the exact Mie scattering solution and also to the other closed form solution by Alam and Massoud. The present work is found to be, however, more generalized and also more accurate for the coated spheres of either tiny/small or medium sizes than that of Alam and Massoud. Therefore, the derived formulas can be used for accurately characterizing both surface plasmon resonances of nanoparticles (of small sizes) or nano antenna near-field properties (of medium sizes comparable with half wavelength).

1.4 Layout of the Thesis

The layout of the remaining part of this thesis is outlined as follows:

In Chapter 2, a discrete method, which makes use of the cylindrical dyadic Green's functions (DGF) together with the field equivalence principle, is developed in this thesis for characterizing the electromagnetic transmission through a cylindrical antenna radome of arbitrary cross sections. With the developed discrete method, results of radiation power patterns of antennas, boresight errors, and peak-gain attenuations are obtained and compared with some existing results.

In Chapter 3, the method of moments, which makes use of the spherical dyadic Green's functions (DGF's), is developed to study the electromagnetic transmission through an axil-symmetric radome of superspheroidal shapes. Numerical results on power patterns and boresight errors are obtained and compared for various geometrical parameters of a superspheroidal radome.

In Chapter 4, the dyadic Green's function technique has been employed to characterize electromagnetic radiation of an imposed current line source in the presence of an 2 layered isotropic dielectric elliptical cylinder. The dyadic Green's functions inside and outside of the elliptic cylinder are formulated in terms of the elliptical vector wave functions which are in turn expressed as Mathieu functions. Using the boundary conditions, we derive a set of general equations governing the scattering and transmitting coefficients of the dyadic Green's functions. The scattered and total electric fields in far-zone are then derived analytically and computed numeri-

cally..

In Chapter 5, an efficient approach is proposed to analyse the interior boundary value problem in a spheroidal cavity with perfectly conducting wall. A closed-form solution has been obtained for the eigenfrequencies based on TE and TM cases. By means of least squares fitting technique, the values of the coefficients are determined numerically.

In Chapter 6, a new set of closed form expressions of the classic Mie scattering coefficients of a spherical nanoshell using a power series up to order 6. This set of approximate expressions is found to be very accurate in the large range of various potential engineering applications including optical nanoparticle characterizations and other nanotechnology applications, validated step by step along the derivation procedure. Computations using this closed form solution are very fast and accurate for both lossy and lossless media, but it requires very little effort in the calculations of the cross section results.

In Chapter 7, conclusions and a brief description of future works will be given.

1.5 Publications

The candidate has so far published the following papers in international peer-reviewed journals and international conferences.

1.5.1 Journal Papers

1. Le-Wei Li, Zhong-Cheng Li, Tat-Soon Yeo, and Mook-Seng Leong, "Extinction Cross Sections of Realistic Raindrops: Data-Bank Established Using T-Matrix Method and Non-linear Fitting Technique", *Journal of Electromagnetic Wave and Applications*, vol. 16, no. 7, pp. 1021-1039, 2002.

2. Le-Wei Li, Zhong-Cheng Li, and Mook-Seng Leong, "Closed-Form Eigenfrequencies in Prolate Spheroidal Conducting Cavity", *IEEE Transactions on Microwave Theory and Techniques*, vol. 51, no. 3, pp. 922-927, March 2003.

3. Le-Wei Li, Zhong-Cheng Li, and Mook-Seng Leong, "Radiation due to an Infinitely Long Transmission Line near a Dielectric Elliptical Waveguide: A dyadic Green's function approach", *Radio Science*, vol. 39, no. 1, pp. 1-10, 2004.

4. Le-Wei Li, Zhong-Cheng Li, Hao-Yuan She, Said Zouhdi, Juan R. Mosig, and Olivier J.F. Martin, "A New Closed Form Solution to Light Scattering by Spherical Nanoshells", *IEEE Transactions on Nanotechnology*, accepted and to appear, vol. 8, 2009.

5. Zhong-Cheng Li, Le-Wei Li, and Mook-Seng Leong, "A 3D Discrete Analysis of Cylindrical Radome Using DGF's", submitted to *IEEE Transactions on Antennas and Propagation*, USA, 2009.

6. Zhong-Cheng Li, Le-Wei Li, and Mook-Seng Leong, "A Moment Method Analysis of a Superspheroidal Airborne Radome", submitted to *IEEE Trans-*

actions on Antennas and Propagation, USA, 2009.

1.5.2 Conference Presentations

1. Le-Wei Li, Zhong-Cheng Li, Tat-Soon Yeo, and Mook-Seng Leong, "Extinction Cross Sections of Realistic Raindrops: Data-Bank Established Using T-Matrix Method and Non-linear Fitting Technique", *Proc. of 2002 China-Japan Joint Meeting on Microwaves (CIMW'2002) in Xi'an*, China, pp. 317-320, 2002.

2. Le-Wei Li, Zhong-Cheng Li, and Mook-Seng Leong, "Closed-Form Eigenfrequencies in Prolate Spheroidal Conducting Cavity", *Proc. of 2002 China-Japan Joint Meeting on Microwaves (CIMW'2002) in Xi'an*, China, pp. 333-236, 2002.

3. Le-Wei Li, Zhong-Cheng Li, and Mook-Seng Leong, "A Moment Method Analysis of a Superspheroidal Airborne Radome Excited by a Wire Antenna", *Proc. of 2003 Progress in Electromagnetics Research Symposium (PIERS 2003) in Hawaii*, USA, 2003.

Chapter 2

A 3D Discrete Analysis of Cylindrical Radome Using DGF's

A discrete method, which makes use of the cylindrical dyadic Green's functions (DGF) together with the field equivalence principle, is developed in this chapter for characterizing the electromagnetic transmission through a cylindrical antenna radome shell with arbitrary curved surface. By use of the dyadic Green's functions for multilayered circular cylinders, this discrete method takes into consideration curvature effects of the radome shell, which is usually ignored in classical approaches such as the ray-tracing method and the plane wave spectrum analysis technique. First, the discretized field distribution elements on the outer surface of the cylindrical radome shell are obtained from an arbitrarily distributed source. Then, the re-radiation of these elements are analyzed. With the developed discrete method, results of radiation power patterns of antennas, boresight errors, and peak-gain attenuations are obtained and compared with some existing results.

2.1 Introduction

The effect of a dielectric layer on the penetration of electromagnetic waves is always an interesting subject that has found many applications such as in the studies of the performance of a radar antenna enclosed by a radome. A radome is a dielectric shell that protects the radar antenna system against the environmental effects while at the same time tries not to interfere with its operation [1]. Being a dielectric shell that encloses the antenna, unfortunately, it becomes inevitable that the wavefront of the electromagnetic wave radiated from the antenna will be distorted by the radome. This distortion would cause the radome to adversely affect the operation of the radar system that it intends to protect. For example, radome can produce boresight error, which is an apparent change in the angular position of a radar source or target. In a modern radar system, a small boresight error may result in a serious degradation of the radar's performance. In addition, part of the radiation energy is lost as a consequence of the scattering of the wave from the radome surface. This will results in peak-gain attenuation, which is the loss of peak gain. As a consequence of these two effects, a radome can reduce both the accuracy in determining the angular position of a target and the range at which the target can be detected. The boresight error and the peak-gain attenuation are therefore usually the electrical parameters that are of the greatest concern in any radome design. These two parameters can be obtained by knowing the characteristic of the electromagnetic field both inside and outside the radome.

The ray tracing technique has traditionally been the most widely used method

for describing propagation through a radome. Unfortunately, several approximations are made, with the main simplification being to treat the radome as locally plane. Because of these approximations, the results obtained have limited validity. Several factors such as the antenna size and radome curvature (in wavelength) have been found to influence discrepancies. A thorough examination of this plane-slab approximation method and its validity were done by Subramaniam [62]. To improve on this ray tracing method, Einziger and Felsen [63, 64] presented a general hybrid ray-optical formulation procedure that takes multiple reflection and curvature correction into consideration. Chang and Chan [2] also introduced an alternative approach, which is an extension of the work by Einziger and Felsen [63,64], in their analysis of a two-dimensional radome of arbitrarily curved surface.

Many studies have been done in this area, in order to analyse accurately and improve the performance of the radome [3]. One of the traditional techniques is the ray tracing method which traces a ray in the direction of propagation through the radome wall [4–6]. Arvas et al. [65, 66] have presented a three-dimensional method of moments solution based on the use of the surface equivalence principle. Wu and Rudduck [67] have presented the Plane Wave Spectrum-Surface Integration techniques for boresight analysis of a three-dimensional antenna-radome systems. Finite element analysis of axisymmetric radome has been presented by Gordon and Mittra [68]. Paris [69] has presented a procedure for predicting by computer the radiation pattern of an antenna in the presence of a radome. Jeng [70] has employed three methods which are the Plane Wave Spectrum-Surface Integration [67,70], Single Plane Wave-Surface Integration [70] and Geometric Optics-Monopulse Tracking

techniques [70], in his study of electromagnetic transmission through a 2-dimensional elliptical dielectric shell in his Master degree thesis. In [67, 69, 70], local plane-slab approximation (the same as that applied in the traditional ray-tracing method) has been assumed in the analysis and hence, these methods do not take into consideration the effects of the curvature of the radome shell.

Over the past few decades, the dyadic Green's function (DGF) technique has been widely employed to investigate the interaction of the electromagnetic waves with the layered media in the boundary-value problem [42,43]. Dyadic Green's function is a very powerful technique in analyzing electromagnetic transmission through dielectric shell [42]. Li et al. [44–46] have derived the general expression of the dyadic Green's functions for multi-layered planar medium, multi-layered spherical medium and multi-layered cylindrical medium.

By using these dyadic Green's functions, we are able to conduct a rigorous three-dimensional analysis of the electromagnetic transmission problem through these media (i.e. planar, spherical and cylindrical geometries). This includes the multiple reflection effects and the curvature effects of the medium (spherical and cylindrical) which are taken care of by these dyadic Green's functions. As the DGF is able to give a rigorous analysis of the transmission problem and to take curvature into consideration, it is therefore the intentions of this chapter to make use of such a property of the DGF in the analysis of the antenna-radome problem whose radome shape can be arbitrary. This will ensures a more accurate analysis of the antenna-radome problem as compared to methods that used the plane-slab approximation [67,69,70].

Unfortunately, for a radome in general, its dyadic Green's function cannot be obtained. This is because, in general, the shape of the radome will not fit into a suitable frame such that the derivation of its dyadic Green's function can be carried out. Thus, in this chapter, the existing dyadic Green's functions that have already been derived by Li et at. [46] will be used in the three-dimensional discrete analysis of a cylindrical radome having an arbitrary cross-section.

2.2 Formulation of the Discrete Method

In this section, the general formulation of the discrete method in the analysis of a 3-dimensional cylindrical radome will be presented. This includes the concepts and theories that underly the 3-D discrete method.

2.2.1 Concept Outline

In this discrete analysis, the radome is divided into several discrete sections. Each of these sections is then modeled to be part of an imaginary cylinder (see Fig. 2.1). Using the cylindrical dyadic Green's function associated with this imaginary cylinder, the electromagnetic fields on the outer surface of each of these discrete sections can be found using the appropriate scattered DGF. From these discrete outer surface fields, a set of discrete equivalent current sources that resides on the outer radome surface can be obtained. By using these discrete equivalent sources and the un-

bounded DGF, the transmitted far fields, from which boresight error and peak-gain attenuation can be easily obtained, can then be calculated.

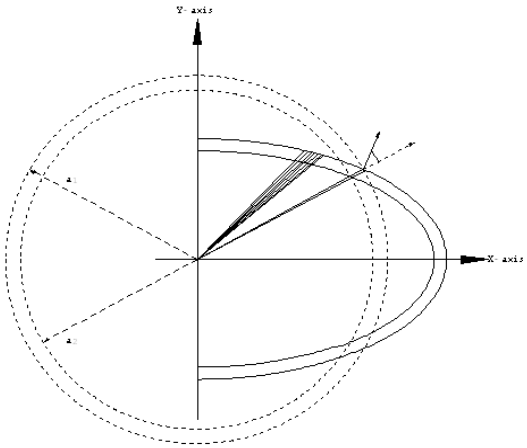

Figure 2.1: Illustrating the discretization of a radome.

2.2.2 Application of the Dyadic Green's Functions

When the dyadic Green's function for a medium is known, its electromagnetic fields can be formulated easily in terms of an integral containing the Green's function and an arbitrary current distribution of the excitation source [46]. Thus, the electromagnetic fields $\boldsymbol{E}_f$ and $\boldsymbol{H}_f$ in the f^{th} layer due to an electric current source $\boldsymbol{J}_s$ in the s^{th} layer can be obtained in terms of its corresponding Green dyadic $\overline{\boldsymbol{G}}_e^{(fs)}(\boldsymbol{r}, \boldsymbol{r'})$ as follows:

$$\boldsymbol{E}_f(\boldsymbol{r}) = i\omega\mu_0 \iiint_{V_s} \overline{\boldsymbol{G}}_e^{(fs)}(\boldsymbol{r}, \boldsymbol{r'}) \cdot \boldsymbol{J}_s(\boldsymbol{r'}) dV', \tag{2.1a}$$

$$\boldsymbol{H}_f(\boldsymbol{r}) = \iiint_{V_s} \left[\boldsymbol{\nabla} \times \overline{\boldsymbol{G}}_e^{(fs)}(\boldsymbol{r}, \boldsymbol{r'})\right] \cdot \boldsymbol{J}_s(\boldsymbol{r'}) dV', \tag{2.1b}$$

where V_s identifies the volume occupied by the sources in the s^{th} layer, μ_f represents the permeability of the medium, and $\overline{\boldsymbol{G}}_e^{(fs)}$ identify the electric types of the dyadic

Green's functions that correspond to the field point in the f-layer and the source point in the s-layer.

Similarly, the electromagnetic fields $\boldsymbol{E}_f$ and $\boldsymbol{H}_f$ in the f^{th} layer due to a magnetic current source $\boldsymbol{M}_s$ in the s^{th} layer can also be obtained using the magnetic types of the dyadic Green's function $\overline{\boldsymbol{G}}_m^{(fs)}(\boldsymbol{r}, \boldsymbol{r'})$ as follows:

$$\boldsymbol{E}_f(\boldsymbol{r}) = -\iiint_{V_s} \left[\boldsymbol{\nabla} \times \overline{\boldsymbol{G}}_m^{(fs)}(\boldsymbol{r}, \boldsymbol{r'})\right] \cdot \boldsymbol{M}_s(\boldsymbol{r'}) dV', \tag{2.2a}$$

$$\boldsymbol{H}_f(\boldsymbol{r}) = i\omega\epsilon_0 \iiint_{V_s} \overline{\boldsymbol{G}}_m^{(fs)}(\boldsymbol{r}, \boldsymbol{r'}) \cdot \boldsymbol{M}_s(\boldsymbol{r'}) dV'. \tag{2.2b}$$

Here, take note that the electric and magnetic types of dyadic Green's functions $\overline{\boldsymbol{G}}_e^{(fs)}(\boldsymbol{r}, \boldsymbol{r'})$ and $\overline{\boldsymbol{G}}_m^{(fs)}(\boldsymbol{r}, \boldsymbol{r'})$, Eqs. (2.1a) and (2.2b), and Eqs. (2.1b) and (2.2a) are dual [45, 46, 42], respectively. This means that by making the simple replacement $\boldsymbol{E} \to \boldsymbol{H}$, $\boldsymbol{H} \to -\boldsymbol{E}$, $\boldsymbol{J} \to \boldsymbol{M}$, $\boldsymbol{M} \to -\boldsymbol{J}$, $\mu \to \epsilon$, and $\epsilon \to \mu$, one may convert the electric type of dyadic Green's function $\overline{\boldsymbol{G}}_e^{(fs)}(\boldsymbol{r}, \boldsymbol{r'})$ to the magnetic type $\overline{\boldsymbol{G}}_m^{(fs)}(\boldsymbol{r}, \boldsymbol{r'})$, Eq. (2.1a) to Eq. (2.2b), and Eq. (2.1b) to Eq. (2.2a).

In the studies of the antenna radome problems, expressions of the unbounded and scattering dyadic Green's functions which was presented in the article published by Li [46] will be used. In that article, only the dyadic Green's functions of the electric type were derived. However, to obtain the magnetic type of the dyadic Green's functions from the already derived electric type dyadic Green's function, one can apply the electromagnetic duality property.

2.2.3 Unbounded Dyadic Green's Functions

The unbounded cylindrical dyadic Green's functions $\overline{\boldsymbol{G}}_{e0}(\boldsymbol{r}, \boldsymbol{r'})$ for $r \overset{>}{<} r'$ was given in [42,46]. In the case of our analysis of the transmission problem, $r > r'$. Therefore, the unbounded DGF is given below:

$$\overline{\boldsymbol{G}}_{e0}(\boldsymbol{r}, \boldsymbol{r'}) = \frac{i}{8\pi} \int_{-\infty}^{\infty} dh \sum_{n=0}^{\infty} \frac{(2-\delta_n^0)}{\eta_s^2} \cdot \left[\boldsymbol{M}^{(1)}_{\substack{e \\ o}n\eta_s}(h) \boldsymbol{M}'_{\substack{e \\ o}n\eta_s}(-h) + \boldsymbol{N}^{(1)}_{\substack{e \\ o}n\eta_s}(h) \boldsymbol{N}'_{\substack{e \\ o}n\eta_s}(-h) \right], \tag{2.3}$$

where the prime denotes the coordinates (r', ϕ', z') of the current source $\boldsymbol{J}_s$ or $\boldsymbol{M}_s$ and the superscript (1) of the vector wave functions denotes that the third-type cylindrical Bessel function or the first-type cylindrical Hankel function $H_n^{(1)}(\eta_f r)$ is to be used in the expression for the vector wave function.

The expression for the cylindrical vector wave functions are:

$$\boldsymbol{M}_{\substack{e \\ o}n\eta_f}(h) = \boldsymbol{\nabla} \times \left[z_n(kr) \begin{matrix} \cos \\ \sin \end{matrix} (n\phi) e^{ihz} \hat{\boldsymbol{z}} \right], \tag{2.4a}$$

$$\boldsymbol{N}_{\substack{e \\ o}n\eta_f}(h) = \frac{1}{\sqrt{h^2+\eta_f^2}} \boldsymbol{\nabla} \times \boldsymbol{\nabla} \times \left[z_n(kr) \begin{matrix} \cos \\ \sin \end{matrix} (n\phi) e^{ihz} \hat{\boldsymbol{z}} \right], \tag{2.4b}$$

where n and η_f are the eigenvalues, and $Z_n(\eta_f r)$ represents the Bessel function used in the expression. If there is a superscript (1), $Z_n(\eta_f r)$ is replaced by the cylindrical Hankel function of the first-type $H_n^{(1)}(\eta_f r)$, otherwise, cylindrical Bessel function $J_n(\eta_f r)$ of the first-type is assumed.

The eigenvalue, η_f, and the propagation constant, k_f, in the f^{th} layer, are related by the following relation:

$$h^2 = (k_f)^2 - (\eta_f)^2 , \tag{2.5a}$$

$$k_f^2 = \omega^2 \mu_f \varepsilon_f \left(1 + \frac{i\sigma_f}{\omega \varepsilon_f}\right), \tag{2.5b}$$

where ε_f and σ_f denote the permittivity and conductivity of the medium (in the fth region), respectively.

To find the unbounded electromagnetic fields due to an excitation source, Eq. (2.1a) to Eq. (2.2b) can be used with the Green dyadic being the unbounded dyadic Green's function. If the equivalent current sources residing on the outer surface of the radome are known, then the unbounded dyadic Green's function can be used on these equivalent surface current to find the transmitted electromagnetic fields outside the radome. The volume integral will be reduced to a surface integral since these equivalent current sources are assumed to reside only on the radome surface. In addition, if these equivalent current sources are known only at discrete locations on the outer surface of the radome (i.e. it is discrete), then numerical integration such as the trapezoidal or Simpson's integration can be used to evaluate the integral involving these discrete sources. To compute these equivalent sources, the outer surface fields on the radome surface need to be known and they are obtained by using the scattered DGF.

2.2.4 Scattered Dyadic Green's Functions

In [46], the electric DGF corresponding to the transmitted field (i.e. $f = 1$ and $s = 3$) are given:

$$\begin{aligned}\overline{\boldsymbol{G}}_{es}^{(13)}(\boldsymbol{r},\boldsymbol{r'}) = \frac{i}{8\pi}\int_{-\infty}^{\infty} dh \sum_{n=0}^{\infty} \frac{(2-\delta_n^0)}{\eta_3^2} \\ \times \Big[\mathcal{C}_{1H}^{13}\boldsymbol{M}_{\substack{e\\o}n\eta_1}^{(1)}(h)\boldsymbol{M}'_{\substack{e\\o}n\eta_3}(-h) \\ + \mathcal{C}_{1V}^{13}\boldsymbol{N}_{\substack{e\\o}n\eta_1}^{(1)}(h)\boldsymbol{N}'_{\substack{e\\o}n\eta_3}(-h) \\ + \mathcal{C}_{2H}^{13}\boldsymbol{N}_{\substack{o\\e}n\eta_1}^{(1)}(h)\boldsymbol{M}'_{\substack{e\\o}n\eta_3}(-h) \\ + \mathcal{C}_{2V}^{13}\boldsymbol{M}_{\substack{o\\e}n\eta_1}^{(1)}(h)\boldsymbol{N}'_{\substack{e\\o}n\eta_3}(-h)\Big]. \end{aligned} \tag{2.6}$$

To find its corresponding magnetic type $\overline{\boldsymbol{G}}_{ms}^{(13)}(\boldsymbol{r},\boldsymbol{r'})$, the dual property is applied.

Here, $\mathcal{C}_{1H}^{13}, \mathcal{C}_{1V}^{13}, \mathcal{C}_{2H}^{13}, \mathcal{C}_{2V}^{13}$ are the scattering coefficients of the DGF. These coefficients are easily obtained from the transmission matrices $\mathbf{F}_{jm}^{H}$ and $\mathbf{F}_{jm}^{V}$ as demonstrated in [46]. The expressions for these coefficients as well as the transmission matrices can be found in Appendix I for completeness of this paper itself. The scattered coefficients $\mathcal{C}_{1H}^{13}$, $\mathcal{C}_{1V}^{13}$, $\mathcal{C}_{2H}^{13}$, $\mathcal{C}_{2V}^{13}$ are dependent on the radii (a_1 and a_2 in Fig. 2.1) of the inner and outer cylinders.

To find the transmitted electromagnetic fields at a particular point on the outer surface of the modeling cylinder, Eqs. (2.1a)-(2.2b) and the scattering DGF will be used with the variable r and θ in the vector wave functions to be the co-ordinates of that particular point.

2.2.5 Correction Factor

As can be seen from Fig. 2.1, the actual unit normal $\widehat{\boldsymbol{n}}$ of the radome surface may not be in line with the unit normal $\widehat{\boldsymbol{n}}_c$ of the circular cylinder that models the discrete sections. These two normals differ by an angle of θ_d. To correct for this non-alignment of the two normals, a correction factor is formulated. This correction factor will be multiplied to the scattered coefficients $\mathcal{C}_{1H}^{13}, \mathcal{C}_{1V}^{13}, \mathcal{C}_{2H}^{13}, \mathcal{C}_{2V}^{13}$ of the scattered DGF in order to obtain the "corrected" scattered coefficients for that particular elementary section.

To obtain the expression for the correction factor $\mathcal{F}$, the transmission coefficient through a planar layer at both the normal incidence and oblique incidence needs to be known. These planar transmission coefficients are given as follow.

At normal incidence, the planar transmission coefficient is

$$T_{\mathrm{pn}} = \frac{\frac{4\eta_2\eta_1}{(\eta_2+\eta_1)^2}}{1-\frac{(\eta_2+\eta_1)^2\ e^{i2k_2t}}{(\eta_2+\eta_1)^2}}. \tag{2.7}$$

At an oblique incidence, the planar transmission coefficient is

$$T_{\mathrm{po}} = \frac{\frac{4\eta_2\eta_1\cos\theta_i\cos\theta_t}{(\eta_2\cos\theta_i+\eta_1\cos\theta_t)^2}}{1-\frac{(\eta_2\cos\theta_i+\eta_1\cos\theta_t)^2\ e^{i2k_2t}}{(\eta_2\cos\theta_i+\eta_1\cos\theta_t)^2}}, \tag{2.8}$$

where

$$\eta_1 = \sqrt{\frac{\mu_1}{\epsilon_1}}, \tag{2.9a}$$

$$\eta_2 = \sqrt{\frac{\mu_2}{\epsilon_2}}, \tag{2.9b}$$

and

$$k_2 = \omega\sqrt{\mu_2\epsilon_2}, \tag{2.10}$$

where μ is the permeability of the medium, ϵ is the permittivity of the medium, θ_i is the incidence angle, θ_t is the transmitted angle and t is the thickness of the planar layer. The subscript 1 denotes the medium in region 1 (free space) while the subscript 2 denotes the radome's layer which is in region 2.

The correction factor is formulated as the ratio of the planar transmission coefficient at an oblique angle of θ_d ($T_{\rm po}$ where the subscript "po" denotes "the planar oblique") through a plane slab to the one at normal incidence ($T_{\rm pn}$ where the subscript "pn" denotes "the planar normal") through the plane slab.

$$\mathcal{F} = \frac{\dfrac{4\eta_2\eta_1\cos\theta_i\cos\theta_t}{\left(\eta_2\cos\theta_i+\eta_1\cos\theta_t\right)^2}}{1-\dfrac{\left(\eta_2\cos\theta_i+\eta_1\cos\theta_t\right)^2\ e^{i2k_2t}}{\left(\eta_2\cos\theta_i+\eta_1\cos\theta_t\right)^2}}\ \frac{1-\dfrac{\left(\eta_2+\eta_1\right)^2\ e^{i2k_2t}}{\left(\eta_2+\eta_1\right)^2}}{\dfrac{4\eta_2\eta_1}{\left(\eta_2+\eta_1\right)^2}}. \tag{2.11}$$

The plane slab thickness is the same as the thickness of the circular cylinder that models the small section. Such a ratio is obtained by assuming that the following relationship holds,

$$\frac{T_{\rm po}}{T_{\rm pn}} = \frac{T_{\rm co}}{T_{\rm cn}}, \tag{2.12a}$$

or

$$T_{\rm co} = \frac{T_{\rm po}}{T_{\rm pn}}T_{\rm cn}. \tag{2.12b}$$

In (2.12), the parameter $T_{\rm co}$ (where the subscript "co" denotes "the circular oblique") represents the "corrected" circular transmission coefficient, $T_{\rm cn}$ (where the subscript

"cn" denotes "the circular normal") represents the scattered coefficients $\mathcal{C}_{1H}^{13}, \mathcal{C}_{1V}^{13}, \mathcal{C}_{2H}^{13}, \mathcal{C}_{2V}^{13}$ of the DGF.

2.2.6 Equivalent Current Source

Once the fields on the outer surface of the radome are found, its equivalent electric current source $\boldsymbol{J}_{es}$ and magnetic current sources $\boldsymbol{M}_{es}$ can be determined easily by the following relationships:

$$\boldsymbol{J}_{es} = \widehat{\boldsymbol{n}} \times \boldsymbol{H}_s, \tag{2.13a}$$

$$\boldsymbol{M}_{es} = \boldsymbol{E}_s \times \widehat{\boldsymbol{n}}, \tag{2.13b}$$

where $\boldsymbol{E}_s$ and $\boldsymbol{H}_s$ refer to the electric and magnetic fields on an elementary surface of the radome, respectively, and $\widehat{\boldsymbol{n}}$ refers to the outward unit normal at this radome's surface element.

2.2.7 Transmitted Field

Once the equivalent discrete current sources that resides on the outer surface of the radome is known, the antenna-radome combination can then be taken to be effectively represented by this set of discrete equivalent current sources. Hence, the transmitted field through the radome can be obtained by evaluating the unbounded field due to this set of equivalent current sources.

2.3 Application to 2D Elliptical Radome

The aforementioned procedure for the computation of the electromagnetic fields is valid for a three-dimensional analysis since the source could be of an arbitrary current distribution and the field point can be any point in a 3-D cylindrical coordinates. However, to verify our analysis, we consider herein a 2-D case where the source is assumed to be an infinite long wire of uniform current distribution as given in [70].

2.3.1 Implementation

By considering the antenna source to be that of an infinite $\hat{\boldsymbol{z}}$-directed current distribution [70], the discrete analysis of a 3-dimensional cylindrical radome will be reduced to a 2-dimensional problem which can be easily implemented in a numerical program. The structure of elliptical radome that is considered has been illustrated in Figure 2.2.

In Fig. 2.2, t is the thickness of the radome, Ω is the scan angle of the antenna, a is the major axis and b is the minor axis. The various dimensions of the 2-dimensional elliptical radome that will be used in the analysis are as follows: $L = 5\lambda_0$, $D = \frac{10}{3}\lambda_0$, $a = 20\lambda_0$, and $b = 10\lambda_0$. Here, λ_0 is the wavelength in free space of the antenna field and ϵ_n is the relative permittivity of the dielectric radome shell. The source antenna is of an infinite $\hat{\boldsymbol{z}}$-directed electric current distribution $\boldsymbol{J}_s$ which is invariant with the $\hat{\boldsymbol{z}}$-direction and it is of unit amplitude (i.e. $\boldsymbol{J}_s = \hat{\boldsymbol{z}} e^{-i\omega t}$).

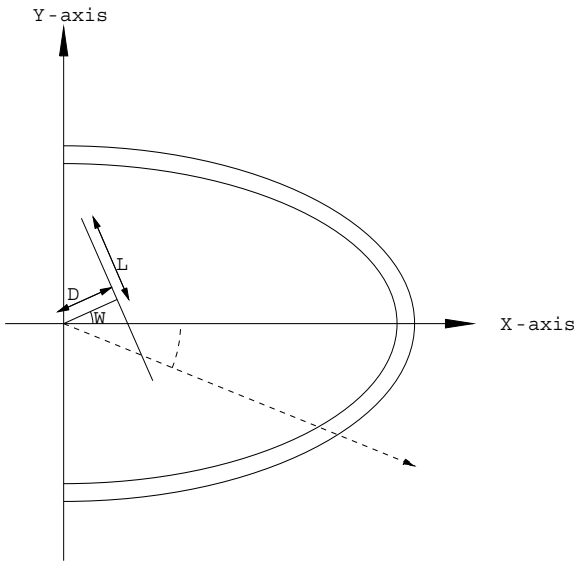

Figure 2.2: Geometry of the elliptical radome used in the study.

Using the scattered DGF, both the discrete magnetic and electric fields on the outer surface elements of the radome is first computed. From these discrete fields, its equivalent magnetic and electric current sources are then obtained by using the relationships as shown in Eqs. (2.13a) and (2.13b). The antenna-radome combination is now taken to be represented by this set of equivalent discrete current sources. The total transmitted electric fields due to these equivalent sources can be further computed using the unbounded DGF. Here, the total transmitted field will consist of 2 components: the E-field due to the equivalent electric source and the E-field due to the equivalent magnetic source.

The numerical program is implemented using the Wolfram's *Mathematica* (where 180 discrete points used). The numerical program has been checked carefully to ensure its validity before it is used to assess the radome's performance. For example, the program is used to generate the transmitted electric field for the case in which

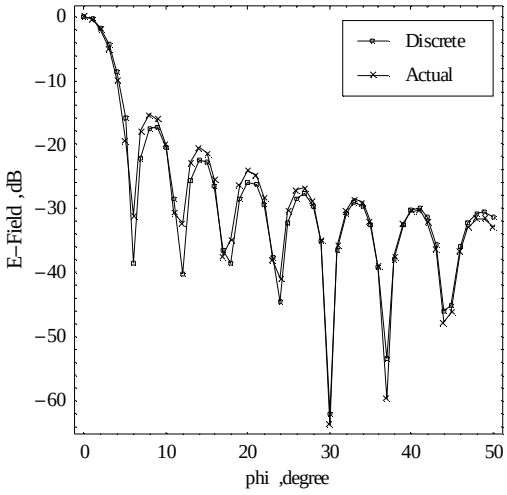

Figure 2.3: Radiation pattern for $\epsilon_n = 1$

the dielectric constant of the radome is set to be that of the free space. In such case, the radome should have no effect on the radiation fields. The radiation field generated by this numerical program is shown in Fig. 2.3. As can be seen, the result generated by the numerical program is well within the range of error of tolerance incurred due to numerical computations.

2.3.2 Numerical Results

With the aforementioned numerical implementation, various results of radiation power patterns of the antenna, boresight errors of the radome, and peak gain attenuations are obtained for the cases where $t = \lambda/2$, λ, and 2λ, as shown in Fig. 2.4 to Fig. 2.11. In the computation, the relative permittivity ϵ_r is set to be 2.

Fig. 2.4 to Fig. 2.7 show the radiation power patterns obtained by the discrete method at various scanning angles (Ω) of 0^o, 6^o, 18^o, and 24^o, respectively. The

radiation patterns for three different thickness are obtained and plotted for each scanning angle. It is seen that the radiation patterns differ slightly when the thickness of the radome is an integer times of half-a-wave ($\lambda/2$). However, the radiation patterns are shifted when the scanning angle is increased from 3^o to 24^o.

Fig. 2.8 and Fig. 2.10 illustrate the boresight errors of the radome for the cases where $t = 1\lambda$ and $t = 2\lambda$, respectively. These boresight errors of the radome are compared with the results obtained in [2] which used the plane wave spectrum-surface integration method (PWS-SI) and the model cylindrical wave-spectrum method (Cyl-WS).

Fig. 2.9 and Fig. 2.11 depict the peak-gain attenuations of the radome for these two cases, respectively. The results of the peak-gain attenuations of the radome are also compared with the results obtained in [2].

To compare with the results in [70] which used the PWS-SI method, another case of the radome is considered where $t = 1\lambda$ and $\epsilon_n = 4$. Fig. 2.12 to Fig. 2.15 show the radiation patterns obtained by the discrete method as compared with those published in [2].

2.4 Discussion

Before one can draw any conclusion from the comparisons in Fig. 2.8 to Fig. 2.15, the accuracy of the PWS-SI method and the model cylindrical wave-spectrum method should first be determined.

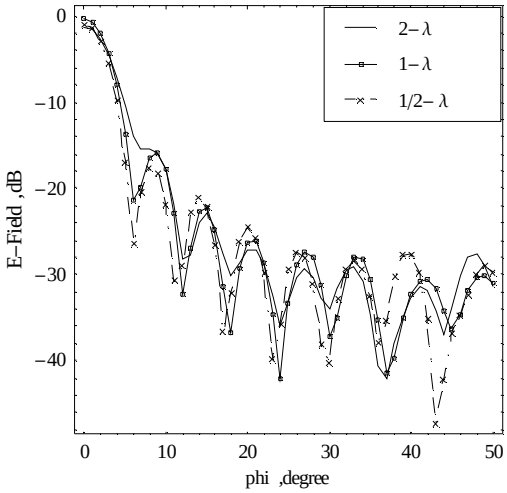

Figure 2.4: Radiation patterns for various thicknesses at a scan angle of 0^o.

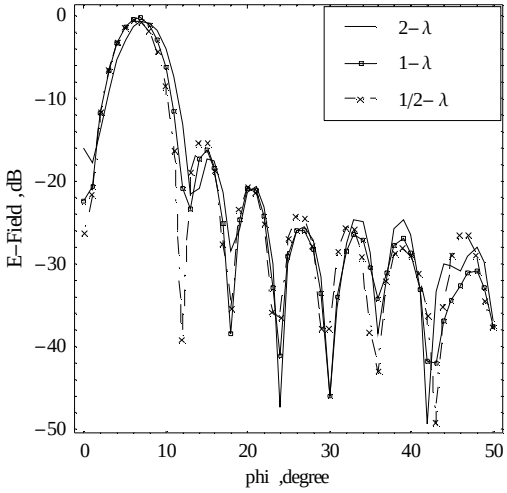

Figure 2.5: Radiation patterns for various thicknesses at a scan angle of 6^o.

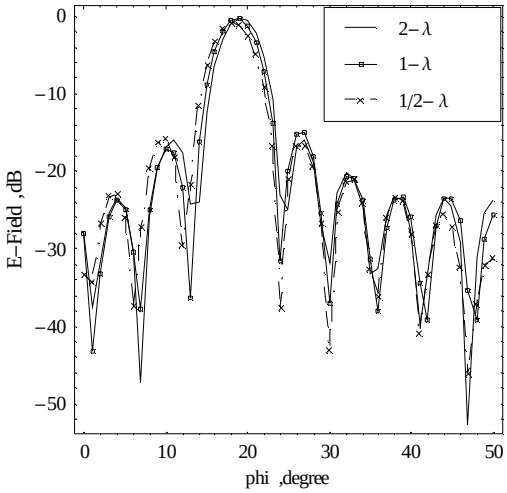

Figure 2.6: Radiation patterns for various thicknesses at a scan angle of 18^o.

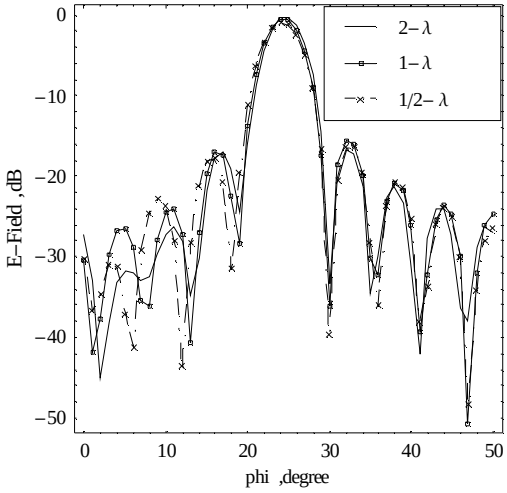

Figure 2.7: Radiation patterns for various thicknesses at a scan angle of 24^o.

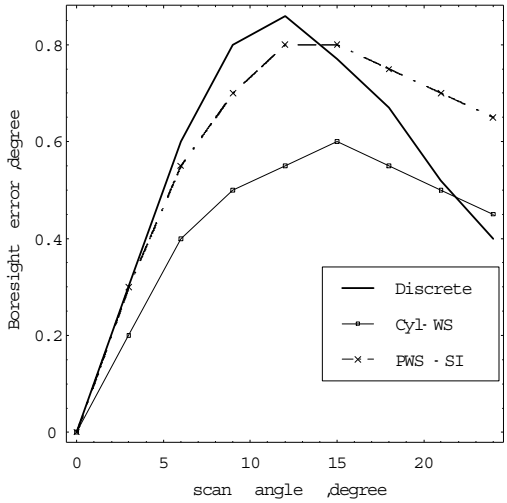

Figure 2.8: Boresight error for a thickness of λ.

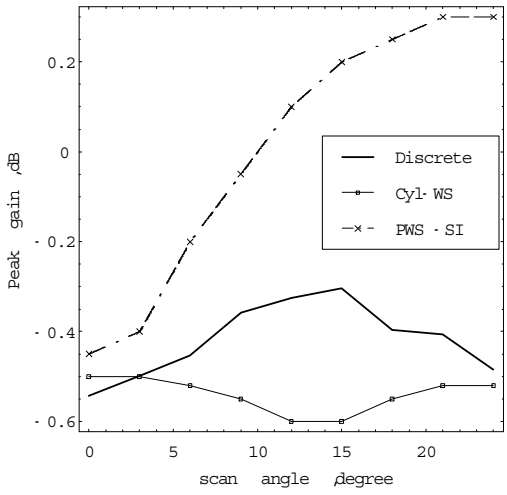

Figure 2.9: Peak-gain attenuation for a thickness of λ.

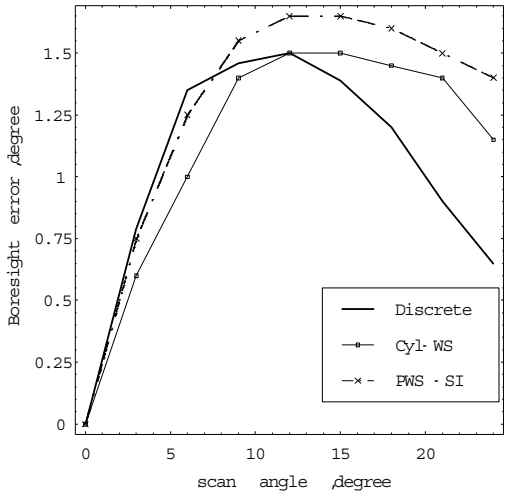

Figure 2.10: Boresight error for a thickness of 2λ.

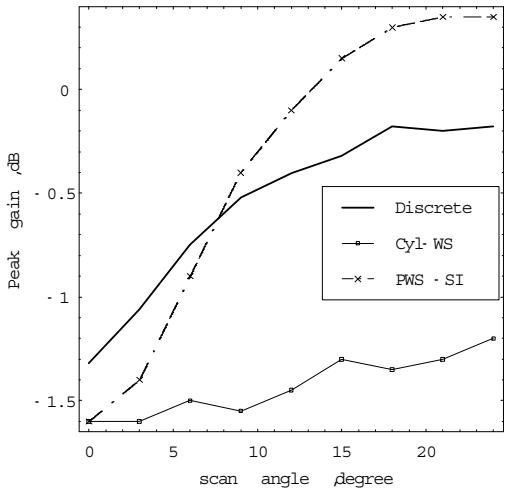

Figure 2.11: Peak-gain attenuation for a thickness of 2λ.

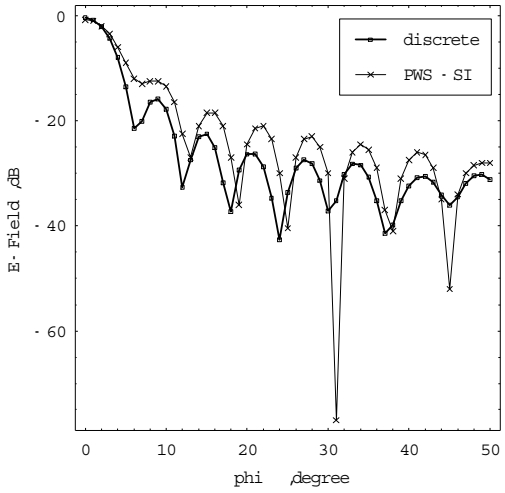

Figure 2.12: Radiation pattern for a thickness of λ at a scan angle of 0^o.

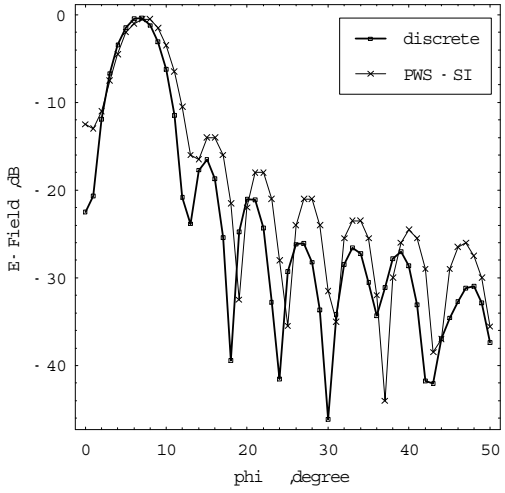

Figure 2.13: Radiation pattern for a thickness of λ at a scan angle of 6^o.

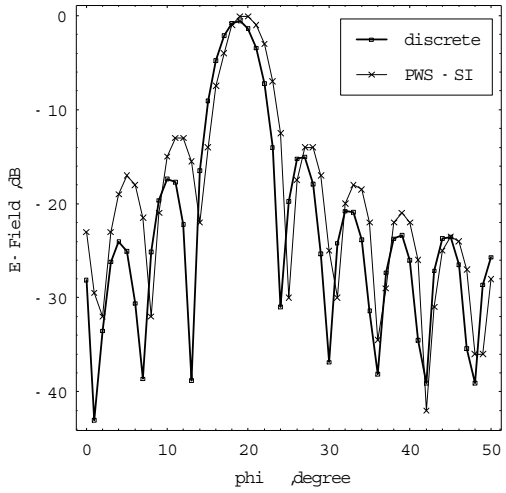

Figure 2.14: Radiation pattern for a thickness of λ at a scan angle of 18^o.

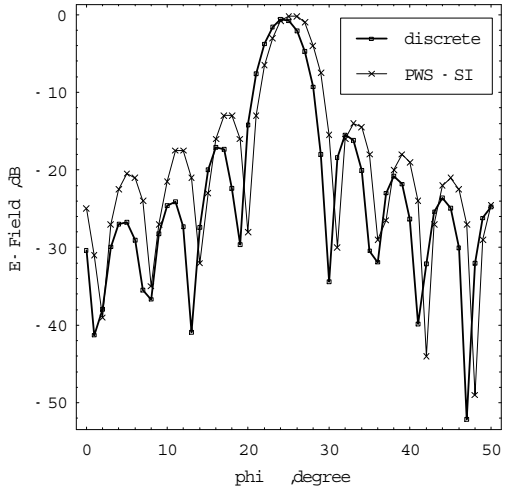

Figure 2.15: Radiation pattern for a thickness of λ at a scan angle of 24^o.

Although several assumptions and approximations had been made in both the PWS-SI method and the model cylindrical wave-spectrum method, their generated results, even not exact, should still approximate the real solution quite well. This is because, in these methods, major transmission effects through a dielectric layer had been taken into consideration. Hence, both the PWS-SI and model cylindrical wave-spectrum method should, in these cases of elliptical radome, produce results which are of acceptable or reasonable accuracy.

From the comparisons in Fig. 2.8 to Fig. 2.15, it can be seen that the results that are generated by the discrete method lie between or close to the results that were obtained by the PWS-SI method and the model cylindrical wave-spectrum method. Hence, this would suggest that the accuracy of the discrete method is reasonable. Theoretically, the discrete method should, however, be more accurate and/or better than both the PWS-SI method and the cylindrical wave-spectrum method.

In the PWS-SI method, plane-slab approximation is used. This means that the curvature effect of the radome's surface has not been taken into consideration. On the other hand, the discrete method, by the virtue of using the dyadic Green's function, takes the curvature of the radome's shell into consideration. In this aspect, the discrete method should provide more accurate results than the PWS-SI method. This argument applies to other conventional methods such as the ray-tracing method that uses plane-slab approximation.

In the model cylindrical wave-spectrum method, although the curvature of the radome was taken into consideration, it was only valid for a 2-dimensional analysis

of the antenna-radome problem. On the other hand, the discrete method is valid for a more general 3-dimensional analysis of the antenna-radome problem where the source current could be arbitrarily distributed. In addition, there are some doubts or uncertainty concerning the formulation of the model cylindrical wave-spectrum method. For example, in the model cylindrical wave-spectrum method, at each point on the radome surface, it is modeled locally as a circular cylindrical layer with its radius being equal to the radius of curvature at that particular point. In this way of formulation, there might arise a situation in which the radius of the modeling circular layer might become too small such that the source is now effectively outside this imaginary circular layer. In this way, the transmission formulation at that point might becomes invalid. This was what had been encountered when attempts are made to use this curvature in the discrete method. The radiation pattern that is obtained using this consideration was found to be out of what should be reasonable! Note that, although the radome wall is curved and the fields that incidence on the wall are at an oblique angle, the expected pattern should not be very far off the unbounded radiation pattern since the thickness of the radome is of half-a-wavelength ($\lambda/2$) and its relative permittivity is only 2.

Finally, although the discrete method is used in the analysis of a 3-dimension cylindrical radome in this paper, the same principle can be applied in the study of electromagnetic transmission through, and/or scattering by, a 3-dimensional enclose structure such as the superspheroidal radome shells. For such a 3-dimensional enclosed structure, the spherical DGF should be used instead of the cylindrical DGF which is considered here.

2.5 Conclusions

In this chapter, a three-dimensional discrete method, which makes use of cylindrical dyadic Green's functions, has been proposed in the study of electromagnetic transmission through a cylindrical radome of non-circular cross sections. The general formulation of this discrete method in the study of a 3-dimensional cylindrical radome of arbitrary cross sections is derived. As an example, this general formulation is then applied to the study of electromagnetic transmission through a 2-dimensional elliptical cylindrical radome shell where the source current of the antenna is considered to be infinite in the $\hat{\boldsymbol{z}}$-direction. Several cases of this 2-dimensional elliptical cylindrical radome shell have been studied. The numerical results generated by the discrete method for these cases are compared with those obtained by the PWS-SI and the model cylindrical wave-spectrum method (published in [2] and [70]). From these comparisons, it was concluded that the discrete method is quite accurate. In fact, the discrete method, by the virtue of using DGF, should give a more accurate result. This is because the curvature effects of the radome's layer/shell among other considerations have been taken into account by the usage of the DGF.

Chapter 3

Discrete Analysis of a 3D Airborne Radome of Superspheroidal Shapes

---

In this chapter, a discrete method, which makes use of the spherical dyadic Green's functions (DGF's), is developed to study the electromagnetic transmission through an axisymmetric radome of superspheroidal shapes. By means of the dyadic Green's functions, the discrete method inherently accounts for the curvature effects of the radome shell, which is generally ignored in classical approaches such as the ray-tracing method and the plane wave spectrum analysis. This proposed discrete method is thus able to give a more accurate analysis on the electromagnetic transmission problem through an airborne radome of superspheroidal shapes. Numerical results on power patterns and boresight errors are obtained and compared for various geometrical parameters of a superspheroidal radome.

3.1 Introduction

Radomes are used to enclose antennas with the principal purpose of shielding the antenna from the physical environment. This improves system availability since the antenna is not affected by winds, rain, or ice. It can also improve performance since high winds can distort the shape and pointing direction of the reflector. Typical applications include antennas for ground, maritime, aircraft and missile electronics system. Being in a protected environment, the life cycle of the antenna improves. Moreover the structural requirements of the antenna are less stringent, resulting in reduced fabrication and installation costs.

Ideally the radome should appear transparent to radio frequency so as not to degrade the electrical performance of the enclosed antenna. However in practice, the antenna performance can be altered by radome effects on its radiation pattern. The more significant of these effects is the boresight error which is the bending of the angle-of-arrival of a received signal relative to its actual angle-of-arrival, arising from distortions of the electromagnetic wavefront as it propagates through a dielectric radome wall. Another effect is antenna side lobe-level degradation which occurs both because of losses in the radome and distortion in the antenna pattern, as a result of deformation of the effective illumination pattern. In addition, radiation scattered from the radome may affect radar performance by elevating antenna side lobes, thus adding to the clutter that must be mitigated via signal processing. Lastly there are copolarized and cross-polarized transmission loss which are usually the result of reflection at the air/dielectric interface and dissipation within the dielectric layers.

Many studies have been done in this area, in order to analyse accurately and improve the performance of the radome [3]. One of the traditional techniques is the ray tracing method which traces a ray in the direction of propagation through the radome wall [4–6]. Beside the various ray tracing techniques, other methods include the plane-wave spectrum [10, 11], modal cylindrical-wave spectrum [12], and the Geometric theory of diffraction [13] each applying their own set of approximations to solve the radome problem. The Finite Element method [14] assumes that the radome does not affect the antenna current distribution, in order for the model to work.

This chapter applies the Method of Moments to the study of electromagnetic transmission through a superspheroidal radome with dielectric layer. This is a discrete method which makes use of the spherical dyadic Green's functions (DGF's). By means of the inner product, the method effectively takes into account the continuity of the surface, instead of discretizing it. This proposed method is thus able to give a more accurate analysis on the electromagnetic transmission problem through a superspheroidal radome. Numerical results on the far field radiation pattern are generated for various geometrical parameters of the superspheroidal radome, and compared.

3.2 Formulation of the Problem

This section will be presenting a general formulation of the analysis that is used in the study of the far field properties of a source enclosed within a 3-dimensional super-

spheroidal radome with a dielectric shell. This includes looking into the properties of the radome, as well as a detailed presentation of the theory and mathematical expressions that are essential in the study. The unbounded dyadic Green's function and the spherical vector wave functions are also given, including how these expressions can be used to generate a general formulation for the electromagnetic field of the dipole within the radome.

3.2.1 Concept Outline

In the analysis as presented in this chapter, the electromagnetic fields in the inner and outer regions of the radomes, as well as that within the dielectric radome layer are first formulated in terms of the unbounded dyadic Green's function and the vector wave functions, together with unknown coefficients to be determined. Then by making use of the boundary conditions for the electromagnetic fields on both the inner and outer surfaces, a coupled set of integral equations are generated. These unknown coefficients are solved using the Method of Moments. Knowledge of the unknown coefficients will allow the determination of the far field radiation pattern.

3.2.2 Analysis of a 3D Superspheroidal Radome

Due to the axis-symmetric property of the superspheroid shape, and the fact that a dipole oriented along the axis of revolution is employed, it is sufficient to consider a 2-dimensional description of the problem (see Fig. 3.1). Making use of the spherical

coordinates system, it is obvious that quantities like the electric field and unit normal to the surface, are all independent of the $\hat{\phi}$ component.

This chapter will be investigating a three-layered medium in which the outer-most and the inner-most layers are free space medium while the second layer constitutes the radome material which is of dielectric nature. The source is located in the inner-most layer of the radome, at the intersection of the axis and the base. In Fig. 3.1, a is the length of the radome along the axis of revolution and b is the radius at the cross-sectional base of the radome. t is the thickness, while r is the distance measured from the intersection of the base and the axis of revolution (i.e. the origin).

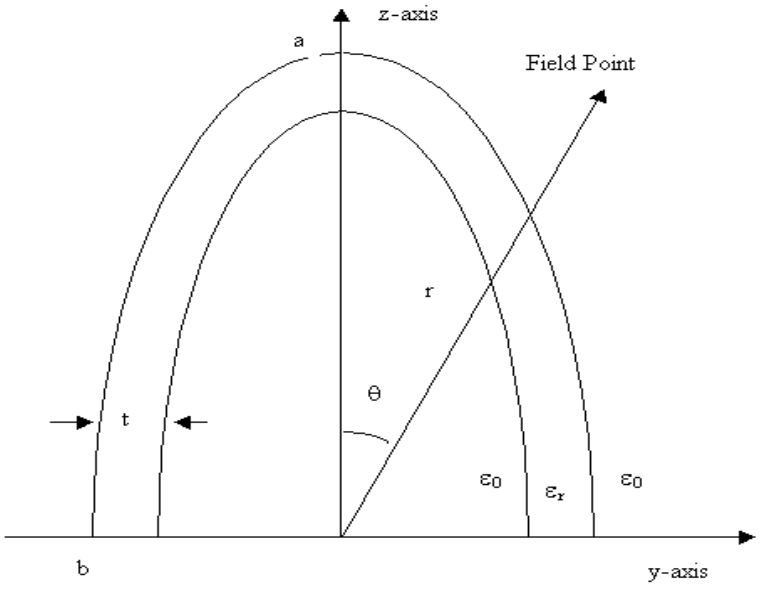

Figure 3.1: Geometry of the elliptical radome used in the study.

To analyze the problem, we will first take a look at the 3-dimensional super-spheroidal shape defined by the equation below as derived by P.L. Overfelt in [71].

$$y^2 + z^2 = \left(\frac{b}{a}\right)^2 (a^v - x^v)^{\frac{2}{v}}, \qquad b \leq a. \tag{3.1}$$

The unit normal can be easily derived from (3.1) as

$$\widehat{\boldsymbol{n}} = \pm \frac{b^2 x^{v-1}\hat{x} + a^2(a^v - x^v)^{(1-\frac{2}{v})}(y\hat{y} + z\hat{z})}{\left\{b^4 x^{2(v-1)} + a^4(a^v - x^v)^{2(1-\frac{2}{v})}(y^2 + z^2)\right\}^{\frac{1}{2}}}. \tag{3.2}$$

Since the analysis in this paper will be dealing heavily with electromagnetic field and waves, it is necessary to express the unit normal derived above in the spherical coordinates system. Making a translation between the three axes by replacing the x axis by the z axis, the y axis by the x axis, and finally the z axis by the y axis, equation (3.2) becomes

$$\widehat{\boldsymbol{n}} = \pm \frac{a^2(a^v - z^v)^{(1-\frac{2}{v})}(x\hat{x} + y\hat{y}) + b^2 z^{v-1}\hat{z}}{\left\{a^4(a^v - z^v)^{2(1-\frac{2}{v})}(x^2 + y^2) + b^4 z^{2(v-1)}\right\}^{\frac{1}{2}}}. \tag{3.3}$$

Using the transformation from the rectangular to the spherical coordinates system [72], it can be shown that (3.3) can be expressed in terms of r and θ only such that

$$\widehat{\boldsymbol{n}}(r,\theta) = \frac{\widehat{\boldsymbol{n}}_{num}(r,\theta)}{n_{den}(r,\theta)}, \tag{3.4}$$

where

$$\widehat{\boldsymbol{n}}_{num}(r,\theta) = n_r\hat{r} + n_\theta\hat{\theta} + n_\phi\hat{\phi}, \tag{3.5}$$

such that

$$\begin{aligned} n_r \;=\; & \left\{a^2 r\sin^2\theta[a^v - r^v\cos^v\theta]^{(1-\frac{2}{v})}\right. \\ & \left. + b^2 r^{(v-1)}\cos^v\theta\right\}, \end{aligned} \tag{3.6a}$$

$$n_\theta = \left\{ a^2 r \sin\theta \ \cos\theta [a^v - r^v \cos^v\theta]^{(1-\frac{2}{v})} - b^2 r^{(v-1)} \cos^{(v-1)}\theta \ \sin\theta \right\}, \tag{3.6b}$$

$$n_\phi = 0. \tag{3.6c}$$

The component ϕ have been set to zero here, since it does not make any contribution in our dealing with a vertical dipole. The relationship between r and θ is as given below by

$$r = \frac{ab}{[(a\sin\theta)^v + (b\cos\theta)^v]^{\frac{1}{v}}}. \tag{3.7}$$

3.2.3 General Formulation of the Electromagnetic Fields

The spherical unbounded dyadic Green's function can be used to find the electric field generated by a source [73].

$$\boldsymbol{E}_{gen}(\boldsymbol{r}) = \sum_{n=1}^{\infty}\sum_{m=0}^{n} [\ \boldsymbol{M}^{(1)}_{\substack{e\\o}mn}(k_s) K_{\substack{even\\odd}} + \boldsymbol{N}^{(1)}_{\substack{e\\o}mn}(k_s) L_{\substack{even\\odd}}\ ] \tag{3.8}$$

where

$$K_{\substack{even\\odd}} = -\frac{\omega\mu_s k_s}{4\pi}(2-\delta^0_m)\frac{2n+1}{n(n+1)}\frac{(n-m)!}{n+m)!}\cdot \iiint_{V_s} \boldsymbol{M'}^{\ }_{\substack{e\\o}mn}(k_s)\cdot \boldsymbol{J_s}(\boldsymbol{r},\boldsymbol{r'})dV', \tag{3.9}$$

and

$$L_{odd}^{even} = -\frac{\omega\mu_s k_s}{4\pi}(2-\delta_m^0)\frac{2n+1}{n(n+1)}\frac{(n-m)!}{n+m)!}\cdot \iiint_{V_s} \boldsymbol{N'}_{o}^{e}{}_{mn}(k_s)\cdot \boldsymbol{J_s}(\boldsymbol{r},\boldsymbol{r'})dV'. \tag{3.10}$$

In the presence of a dielectric radome, the electromagnetic fields generated by the source in the inner-most region will be subjected to multiple reflection and refraction at the interfaces of the various layers of the radome. The contribution of all the reflected waves due to the inner surface is accounted for by

$$\boldsymbol{E}_{sc}(\boldsymbol{r}) = \sum_{n=1}^{\infty}\sum_{m=0}^{n}[\ \boldsymbol{M}_{o}^{e}{}_{mn}(k_f)C_{mn} + \boldsymbol{N}_{o}^{e}{}_{mn}(k_f)D_{mn}\ ], \tag{3.11}$$

where C_{mn} and D_{mn} are the scattered coefficients of the spherical vector wave functions to be solved, and are functions of m and n. The scattered coefficients accounts for the reflection of the field at the inner surface of the radome, as well as incoming fields from the external layers. The subscript f denotes the field layer. The propagation constant, k_f, in the f^{th} layer satisfies the following relationship

$$k_f = \omega\sqrt{\mu_f\epsilon_f\left(1+\frac{i\sigma_f}{\omega\epsilon_f}\right)}, \tag{3.12}$$

where ϵ_f and σ_f denote the permittivity and conductivity of that field layer, respectively. A time dependence $\exp(-i\omega t)$ is assumed for the fields throughout.

By the principle of superposition, the electromagnetic fields in the inner-most layer($s=3$ and $f=3$) are

$$\boldsymbol{E}_{inner} = \boldsymbol{E}_{gen} + \boldsymbol{E}_{sc}, \tag{3.13}$$

$$\begin{aligned}\boldsymbol{H}_{inner}(\boldsymbol{r}) &= \frac{k_s}{i\omega\mu_s}\sum_{n=1}^{\infty}\sum_{m=0}^{n}[\ \boldsymbol{N}^{(1)}_{\substack{e\\o}mn}(k_s)K^{even}_{odd} \\ &\quad +\boldsymbol{M}^{(1)}_{\substack{e\\o}mn}(k_s)L^{even}_{odd} + \boldsymbol{N}_{\substack{e\\o}mn}(k_f)C_{mn} \\ &\quad +\boldsymbol{M}_{\substack{e\\o}mn}(k_f)D_{mn}\ ]. \end{aligned} \tag{3.14}$$

As for the electromagnetic fields in the outer-most layer of the radome, $f = 1$. These are given by

$$\boldsymbol{E}_{outer}(\boldsymbol{r}) = \sum_{n=1}^{\infty}\sum_{m=0}^{n}[\ \boldsymbol{M}^{(1)}_{\substack{e\\o}mn}(k_f)A_{mn} + \boldsymbol{N}^{(1)}_{\substack{e\\o}mn}(k_f)B_{mn}\ ], \tag{3.15}$$

$$\begin{aligned}\boldsymbol{H}_{outer}(\boldsymbol{r}) &= \frac{k_f}{i\omega\mu_f}\sum_{n=1}^{\infty}\sum_{m=0}^{n}[\ \boldsymbol{N}^{(1)}_{\substack{e\\o}mn}(k_f)A_{mn} \\ &\quad +\boldsymbol{M}^{(1)}_{\substack{e\\o}mn}(k_f)B_{mn}\ ], \end{aligned} \tag{3.16}$$

where A_{mn} and B_{mn} are the transmitted coefficients of the spherical vector wave functions to be solved. The transmitted coefficients account for the transmitted fields in the outer-most layer after undergoing multiple reflection and refraction at the two interfaces.

Clearly, the electromagnetic fields in the centre layer ($f = 2$) must be due to transmitted fields from the inner region that have undergone refraction at the inner interface, as well as the multiple reflected waves in the layer due to it being sandwiched being two layers, together with the incoming fields from the external layer. These are represented by the following

$$\begin{aligned}\boldsymbol{E}_{ctrl}(\boldsymbol{r}) &= \sum_{n=1}^{\infty}\sum_{m=0}^{n}[\ \boldsymbol{M}^{(1)}_{\substack{e\\o}mn}(k_f)a_{mn} + \boldsymbol{N}^{(1)}_{\substack{e\\o}mn}(k_f)b_{mn} \\ &\quad +\boldsymbol{M}_{\substack{e\\o}mn}(k_f)c_{mn} + \boldsymbol{N}_{\substack{e\\o}mn}(k_f)d_{mn}\ ], \end{aligned} \tag{3.17}$$

$$\begin{aligned}\boldsymbol{H}_{ctrl}(\boldsymbol{r}) &= \frac{k_f}{i\omega\mu_f}\sum_{n=1}^{\infty}\sum_{m=0}^{n}[\ \boldsymbol{N}^{(1)}_{\substack{e\\o}mn}(k_f)a_{mn} \\ &\quad +\boldsymbol{M}^{(1)}_{\substack{e\\o}mn}(k_f)b_{mn}+\boldsymbol{N}_{\substack{e\\o}mn}(k_f)c_{mn} \\ &\quad +\boldsymbol{M}_{\substack{e\\o}mn}(k_f)d_{mn}\ ],\end{aligned} \tag{3.18}$$

where a_{mn}, b_{mn}, c_{mn} and d_{mn} are the coefficients of the spherical vector wave functions to be solved, accounting for the effects discussed earlier.

3.2.4 Boundary Condition and the Method of Moments

Now we make use of boundary conditions at the inner and outer interfaces. For TE mode, we obtain following four equations

$$\begin{aligned}\widehat{\boldsymbol{n}}_1\times\sum_{n=1}^{\infty}\sum_{m=0}^{n}[\ \boldsymbol{M}^{(1)}_{\substack{e\\o}mn}(k_1)A_{mn}-\boldsymbol{M}^{(1)}_{\substack{e\\o}mn}(k_2)a_{mn} \\ -\boldsymbol{M}_{\substack{e\\o}mn}(k_2)c_{mn}\ ]=0,\end{aligned} \tag{3.19}$$

$$\begin{aligned}\widehat{\boldsymbol{n}}_2\times\sum_{n=1}^{\infty}\sum_{m=0}^{n}[\ -\boldsymbol{M}_{\substack{e\\o}mn}(k_3)C_{mn}+\boldsymbol{M}^{(1)}_{\substack{e\\o}mn}(k_2)a_{mn} \\ +\boldsymbol{M}_{\substack{e\\o}mn}(k_2)c_{mn}\ ]=\widehat{\boldsymbol{n}}_2\times\sum_{n=1}^{\infty}\sum_{m=0}^{n}[\ \boldsymbol{M}^{(1)}_{\substack{e\\o}mn}(k_s)K^{even}_{odd}\ ],\end{aligned} \tag{3.20}$$

$$\begin{aligned}\widehat{\boldsymbol{n}}_1\times\sum_{n=1}^{\infty}\sum_{m=0}^{n}[\ \frac{k_1}{\mu_1}\boldsymbol{N}^{(1)}_{\substack{e\\o}mn}(k_1)A_{mn}-\frac{k_2}{\mu_2}\boldsymbol{N}^{(1)}_{\substack{e\\o}mn}(k_2)a_{mn} \\ -\frac{k_2}{\mu_2}\boldsymbol{N}_{\substack{e\\o}mn}(k_2)c_{mn}\ ]=0,\end{aligned} \tag{3.21}$$

$$\widehat{\boldsymbol{n}}_2 \times \sum_{n=1}^{\infty}\sum_{m=0}^{n}[\,-\frac{k_3}{\mu_3}\boldsymbol{N}_{\substack{e\\o}mn}(k_3)C_{mn} + \frac{k_2}{\mu_2}\boldsymbol{N}^{(1)}_{\substack{e\\o}mn}(k_2)a_{mn}$$
$$+\frac{k_2}{\mu_2}\boldsymbol{N}_{\substack{e\\o}mn}(k_2)c_{mn}\,] = \widehat{\boldsymbol{n}}_2 \times \sum_{n=1}^{\infty}\sum_{m=0}^{n}[\,\boldsymbol{N}^{(1)}_{\substack{e\\o}mn}(k_s)L^{even}_{odd}\,]. \tag{3.22}$$

These four equations above form a coupled set of integral equations, bounded by the summation series of n and m as given in the expressions for the electric and magnetic fields. Normal algrebra manipulations cannot be applied to solve these equations. So the Method of Moments will be used to solve for these unknown coefficients. we can express the coupled set of integral equations in matrix form as given by

$$\boldsymbol{L}\cdot\boldsymbol{f} = \boldsymbol{y} \tag{3.23}$$

where $\boldsymbol{L}$ is a square matrix with its element being the terms on the left hand side of equations (3.19) to (3.22). $\boldsymbol{y}$ is a column vector containing the terms on the right hand side of the equations. Clearly, $\boldsymbol{f}$ is a column vector of the unknown coefficients.

Taking into account the summation of the series of n from 1 to N, and m is from 0 to n, it is clear that $\boldsymbol{L_{mn}}$ is a matrix of size $4N(N+1)$ by $4N(N+1)$. Now, defining a set of weighting functions, w_l in the range of $\boldsymbol{L_{mn}}$, and taking the inner product of equation (3.23) with each w_l, we obtain

$$< w_l, \boldsymbol{L_{mn}} > \cdot\boldsymbol{f_l} =< w_l, \boldsymbol{y_l} > \tag{3.24}$$

for $l = 1, 2, 3, ..., 4N(N+1)$. The weighting functions [74, 75] chosen should be linearly independent, and such that the evaluation of the matrix do not become too

complex. It must also be such that the matrix do not become singular. In this paper, the cosine function is used such that

$$w_l = \cos(l\theta). \tag{3.25}$$

Using above the method of moments, we can solve for the unknown coefficients (A_{mn}, C_{mn}, a_{mn} and c_{mn}) in the vector $\boldsymbol{f_l}$ by matrix inversion.

Similarly, we also can solve for the unknown coefficients (B_{mn}, D_{mn}, b_{mn} and d_{mn}) of TM mode using the method of moments.

3.3 Numerical Results

In this section, some numerical examples are presented to validate the algorithm as well as to demonstrate the application of the algorithm for analyzing the radiation patterns of dipoles in radomes. The first example considers a dipole array enclosed by a spherical dielectric shell of uniform thickness, for which the analytical solution is available. The inner radius is $1.2\lambda_0$, the thickness is $0.08\lambda_0$, and the relative permittivity is fixed at $\epsilon_r = 2+j$. A $x-$directed 9-element uniform dipole array with quarter wavelength inter-element spacing is placed along the x-axis and centered in the shell. The calculated radiation patterns for $\phi = 0$ and θ from 0 to 90 degrees are shown in Fig. 3.2. As a reference, the radiation pattern of the dipole array in free-space is also plotted in the figure. It can be seen that the MOM solution agrees well with the analytical solution.

The another example shows the calculated results for a dipole array in the presence of an ogive radome, $v = 1.449$. An 8-element dipole array is placed a quarter wavelength above a conducting plate inside the radome (the plate is positioned at the radome base). The base diameter is $5.33\lambda_0$, the length is $6.67\lambda_0$, the thickness is $0.08\lambda_0$, and the relative permittivity is fixed at $\epsilon_r = 2 + j$. The dipole orientations and array axis are in the same direction (perpendicular to the radome axis). The calculated radiation patterns for $\phi = 0$ and θ from 0 to 45 degrees are shown in Fig. 3.3. It can be seen that the MoM solution agrees well with the AIM solution [76].

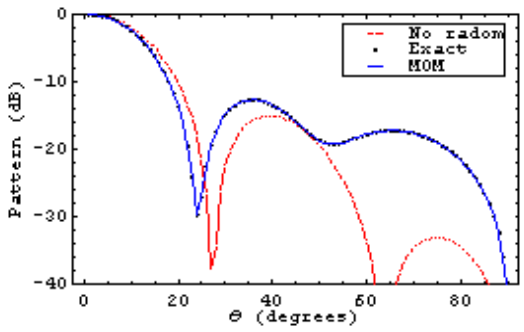

Figure 3.2: Comparison of the MoM result with the exact result for the radiation pattern of a dipole array with a spherical dielectric shell.

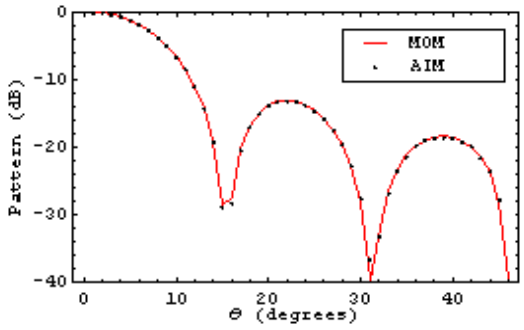

Figure 3.3: Comparison of the MoM result with the AIM result for the radiation pattern of a dipole array with an ogive radome.

Next, a electric dipole is placed a quarter wavelength above a conducting plate inside the radome. The base radius is $10\lambda_0$, the length is $10\lambda_0$, $v = 2$ and the relative permittivity is fixed at $\epsilon_r = 2$. various results of boresight errors and peak gain attenuations of the radome, are obtained for the cases where $t = 1.0\lambda$, 0.5λ, 0.25λ, and 0.1λ, as shown in Fig. 3.4 and Fig. 3.5.

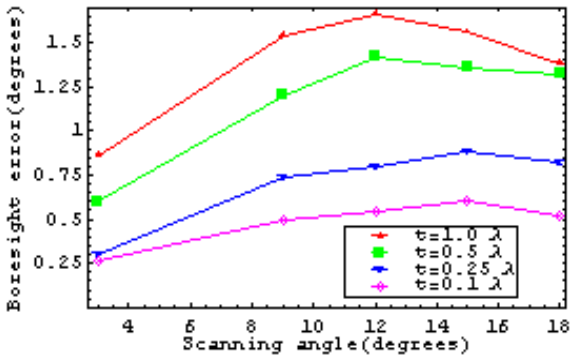

Figure 3.4: Boresight error for various thickness of radome.

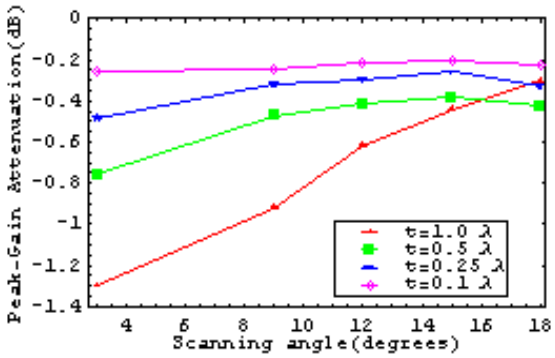

Figure 3.5: Peak-gain attenuations for various thickness of radome.

3.4 Conclusions

In this chapter, the method of moments, making use of the spherical vector wave functions as well as the free space dyadic Green's function, has been proposed in the study of the electromagnetic transmission through a superspheroidal radome having a dielectric shell. The general formulation of the Method of Moments in the study of the far field properties of a source enclosed within a dielectric superspheroidal radome is derived. This general formulation is then applied in the study of electromagnetic transmission through a 3-dimensional superspheroidal radome by considering a point source. The numerical results of these cases were then generated and they were presented in terms of the transmitted electric far-field radiation patterns. From the good agreements with the validity tests, it can be concluded that the method of moments is capable of generating results which are of reasonable accuracy.

Chapter 4

Radiation Due to an Infinitely Transmission Line Near a Dielectric Elliptical Waveguide

---

In this chapter, the dyadic Green's function technique has been employed to characterize electromagnetic radiation of an imposed current line source in the presence of an isotropic dielectric elliptical cylinder. The current density along the infinitely long wire has a constant amplitude but a varying phase. The elliptical cylinder is considered to be infinite in length. In order to analyze the problem, the dyadic Green's functions are expressed in terms of elliptical vector wave functions and the general equations needed to solve for the reflection and transmission coefficients are derived from the boundary conditions. These derived equations are transformed into, and solved using, a linear equation system. Numerically, the radiation patterns of the infinitely long wire are computed, plotted, and shown for various cases

where the position and distance of the line source are varied. Both lossy and lossless dielectric media for the elliptical cylinder are considered. The results are believed to be very useful to many practical problems, and especially to characterize cable radiation or transmission line power leakage in tunnels.

4.1 Introduction

Electromagnetic scattering of a normal incident plane wave by an elliptical cylinder was considered by Yeh [21] and Burke [22]. For the oblique incident case, the equations needed to solve for the scattering and transmission coefficients were formulated by Yeh [23]. The method in those works is to express the incident, scattered and transmitted plane waves in expansions of vector wave eigenfunctions obtained using the separation of variables method. These eigenfunctions are expressed usually in terms of Mathieu functions. The continuity boundary conditions were then implemented in determination of the coefficients in the scattered and transmitted waves. Numerical computations were presented in [21, 22, 24, 25] for the normal incident plane waves. For the oblique incident plane waves, numerical computations were presented by Kim [26]. Up to now, a generalized analysis of electromagnetic radiation problems involving dielectric elliptical cylinders has not been well-documented yet. This motivates the present work which considers electromagnetic radiation due to an infinitely transmission line near a dielectric elliptical cylinder.

To obtain general characteristics of the electromagnetic radiation in the presence of dielectric elliptical cylinders, the dyadic Green's function is an important

kernel of the integral equations [47–55]. Also, the dyadic Green's functions are quite important kernels used in numerical techniques such as the Method of Moments and the Boundary Element Method. The free space dyadic Green's function has already been available in terms of the elliptical vector wave functions. In this work, the dyadic Green's functions for regions 1 and 2 of the geometry are formulated first and the scattering superposition principle is employed. Then, the scattering coefficients of dyadic Green's functions are formulated by employing the boundary conditions.

Using the integral equation, we will consider electromagnetic radiation by an infinitely long transmission line placed near an elliptical cylinder. This transmission line is assumed to have an electric current density of constant amplitude but a varying phase. This current density together with some mathematical properties of the Mathieu functions are utilized to simplify the general equations satisfied by the reflection and transmission coefficients. The linear equation system for the coefficients are then expressed in matrix form and are computed numerically using both matrix manipulations and iterative technique. The electric field in far-zone are then be formulated and computed numerically. Various field patterns are plotted for the transmission line located at different positions with respect to the elliptical cylinder. Discussions are made and conclusion is drawn.

4.2 Coordinate System and Mathematical Functions

The elliptical coordinate system as shown in Fig. 4.1 is defined by the following relations:

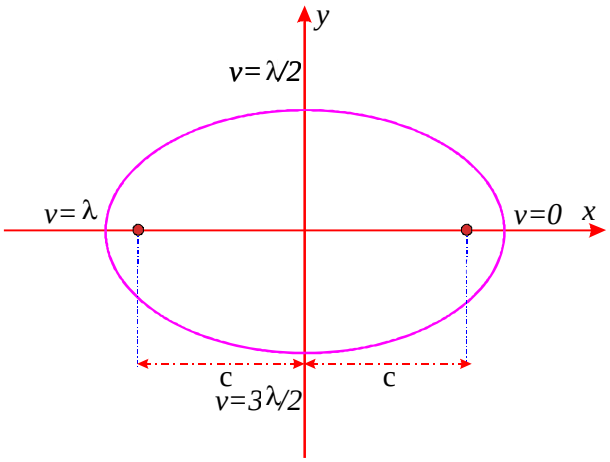

Figure 4.1: A cross section view of the elliptical coordinate system.

$$x = c\cosh(u)\cos(v), \quad y = c\sinh(u)\sin(v), \quad z = z, \tag{4.1}$$

where

$$0 \leq u \leq \infty, \quad \text{and} \quad 0 \leq v \leq 2\pi;$$

while c stands for the semi-focal length of the ellipse. The contour surfaces of constant u represent confocal elliptic cylinders, while those of constant v identify confocal hyperbolic cylinders. The problem of interest in this chapter is shown in

Fig. 4.2 where an infinitely long transmission line source is positioned parallelly with respect to the dielectric elliptical cylinder.

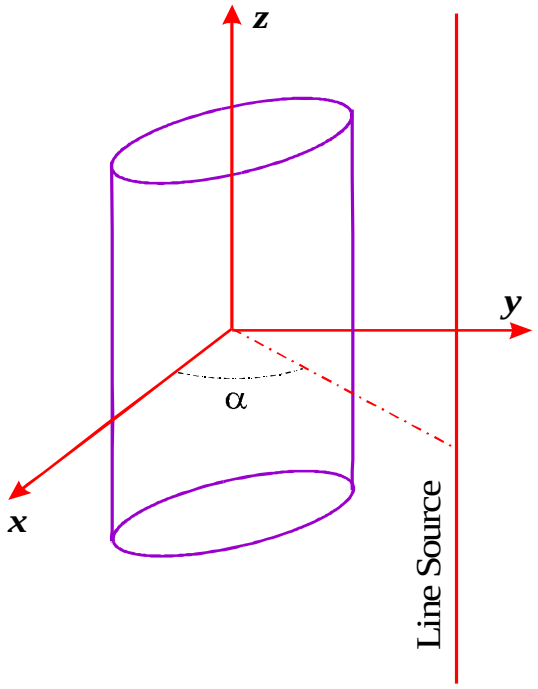

Figure 4.2: Radiation by an infinitely long transmission line in the presence of an elliptical dielectric cylinder.

Two kinds of Mathieu functions are used here, i.e., the periodic solution consisting of the even or odd angular functions, $S_{em\lambda}(v)$ and $S_{om\lambda}(v)$; and the non-periodic functions consisting of the even or odd radial functions, $R_{em\lambda}(u)$ and $R_{om\lambda}(u)$. All the definitions of the Mathieu functions are obtained from the National Bureau of Standards [77] and given below (for a self-contained description):

$$S_{em\lambda}(v) = \sum_{n=0}^{\infty}{}' D_n^m(\lambda)\cos(nv), \quad m = 0, 1, 2, \cdots; \tag{4.2a}$$

$$S_{om\lambda}(v) = \sum_{n=0}^{\infty}{}' F_n^m(\lambda)\sin(nv), \quad m = 1, 2, 3, \cdots; \tag{4.2b}$$

where the summation $\sum_{n=0}^{\infty}{}'$ means that when m is even, n is summed over all the even values and when m is odd, n is summed over all the odd values. The radial Mathieu functions of the first kind are defined as

$$R_{em\lambda}(u) = \sqrt{\frac{\pi}{2}}\sum_{n=0}^{\infty}{}' (i)^{m-n} D_n^m(\lambda) J_n[c\lambda\cosh(u)], \tag{4.3a}$$

$$R_{om\lambda}(u) = \sqrt{\frac{\pi}{2}}\tanh(u)\sum_{n=0}^{\infty}{}' (i)^{n-m} n F_n^m(\lambda) J_n[c\lambda\cosh(u)]. \tag{4.3b}$$

The radial Mathieu functions of the second kind are expressed by

$$N_{e(2m)\lambda}(u) = (-1)^m\sqrt{\frac{\pi}{2}}\sum_{k=0}^{\infty}(-1)^k\frac{D_{2k}^{2m}(\lambda)}{D_0^{2m}(\lambda)}Y_k(a)J_k(b), \tag{4.4a}$$

$$N_{e(2m+1)\lambda}(u) = (-1)^m\sqrt{\frac{\pi}{2}}\sum_{k=0}^{\infty}(-1)^k \times \frac{D_{2k+1}^{2m+1}(\lambda)}{D_1^{2m+1}(\lambda)}[Y_{k+1}(a)J_k(b) + Y_k(a)J_{k+1}(b)], \tag{4.4b}$$

$$N_{o(2m)\lambda}(u) = (-1)^m\sqrt{\frac{\pi}{2}}\sum_{k=1}^{\infty}(-1)^k \times \frac{F_{2k}^{2m}(\lambda)}{F_2^{2m}(\lambda)}[Y_{k+1}(a)J_{k-1}(b) - Y_{k-1}(a)J_{k+1}(b)], \tag{4.4c}$$

$$N_{o(2m+1)\lambda}(u) = (-1)^m\sqrt{\frac{\pi}{2}}\sum_{k=0}^{\infty}(-1)^k \times \frac{F_{2k+1}^{2m+1}(\lambda)}{F_1^{2m+1}(\lambda)}[Y_{k+1}(a)J_k(b) - Y_k(a)J_{k+1}(b)], \tag{4.4d}$$

where $a = \frac{c\lambda}{2}e^u$ and $b = \frac{c\lambda}{2}e^{-u}$. Also, $J_n(\bullet)$ and $Y_n(\bullet)$ denote the Bessel functions of the first and second kinds, respectively. The radial functions of the third kind representing outgoing waves for the given time dependence of $e^{-i\omega t}$ are defined as:

$$R^{(1)}_{\substack{e\\o}m\lambda}(u) = R_{\substack{e\\o}m\lambda}(u) + iN_{\substack{e\\o}m\lambda}(u). \tag{4.5}$$

The orthogonality properties of the angular Mathieu functions are provided as follows:

$$\int_0^{2\pi} S_{em\lambda}(v) S_{om'\lambda}(v) dv = 0, \tag{4.6a}$$

$$\int_0^{2\pi} S_{em\lambda}(v) S_{em'\lambda}(v) dv = \begin{cases} 0, & m \neq m', \\ I_{em\lambda}, & m = m'; \end{cases} \tag{4.6b}$$

$$\int_0^{2\pi} S_{om\lambda}(v) S_{om'\lambda}(v) dv = \begin{cases} 0, & m \neq m', \\ I_{om\lambda}, & m = m'; \end{cases} \tag{4.6c}$$

where

$$I_{em\lambda} = \pi {\sum_{n=0}^{\infty}}' (1+\delta_o) \left[D_n^m(\lambda)\right]^2, \tag{4.7a}$$

$$I_{om\lambda} = \pi {\sum_{n=0}^{\infty}}' \left[F_n^m(\lambda)\right]^2, \tag{4.7b}$$

with $\delta_o = 1$ when $n = 0$ and $\delta_o = 0$ when $n \neq 0$. Note that the orthogonality can only be applied for the same λ. We can express the angular Mathieu functions of different λ and λ' given by McLachlan [78]:

$$S_{em\lambda}(v) = {\sum_{r=0}^{\infty}}' \chi_{emr} S_{er\lambda'}(v), \tag{4.8a}$$

$$S_{om\lambda}(v) = {\sum_{r=1}^{\infty}}' \chi_{omr} S_{or\lambda'}(v), \tag{4.8b}$$

$$\frac{\partial}{\partial v} S_{em\lambda}(v) = {\sum_{r=0}^{\infty}}' \chi_{emr} {\sum_{p=1}^{\infty}}' \zeta_{erp} S_{op\lambda'}(v), \tag{4.8c}$$

$$\frac{\partial}{\partial v} S_{om\lambda}(v) = {\sum_{r=1}^{\infty}}' \chi_{omr} {\sum_{p=0}^{\infty}}' \zeta_{r,p} S_{ep\lambda'}(v). \tag{4.8d}$$

Again, the prime in the summation of $\sum'$ means that when m is even, r or p is summed over even numbers and when m is odd, r or p is summed over all odd

numbers. Using Eqs. (4.2a) and (4.2b), we defined χ_{emr}, χ_{omr}, ζ_{emp} and ζ_{omp} as:

$$\begin{aligned}
\chi_{emr} &= \frac{\int_0^{2\pi} S_{em\lambda}(v) S_{er\lambda'}(v) dv}{\int_0^{2\pi} S_{er\lambda'}^2(v) dv} \\
&= \frac{\sum_{n=0}^{\infty}{}' (1+\delta_0) D_n^m(\lambda) D_n^r(\lambda')}{\sum_{p=0}^{\infty}{}' (1+\delta_0) [D_p^r(\lambda')]^2}, \qquad (4.9a) \\
\chi_{omr} &= \frac{\int_0^{2\pi} S_{om\lambda}(v) S_{or\lambda'}(v) dv}{\int_0^{2\pi} S_{or\lambda'}^2(v) dv} \\
&= \frac{\sum_{n=1}^{\infty}{}' F_n^m(\lambda) F_n^r(\lambda')}{\sum_{p=1}^{\infty}{}' [F_p^r(\lambda')]^2}, \qquad (4.9b) \\
\zeta_{emp} &= \frac{\int_0^{2\pi} \frac{\partial}{\partial v} S_{em\lambda'}(v) S_{op\lambda'}(v) dv}{\int_0^{2\pi} S_{op\lambda'}^2(v) dv} \\
&= \frac{-\sum_{n=1}^{\infty}{}' n D_n^m(\lambda') F_n^p(\lambda')}{\sum_{n=1}^{\infty}{}' [F_n^p(\lambda')]^2}, \qquad (4.9c) \\
\zeta_{omp} &= \frac{\int_0^{2\pi} \frac{\partial}{\partial v} S_{om\lambda'}(v) S_{ep\lambda'}(v) dv}{\int_0^{2\pi} S_{ep\lambda'}^2(v) dv} \\
&= \frac{\sum_{n=1}^{\infty}{}' n F_n^m(\lambda') D_n^p(\lambda')}{\sum_{n=0}^{\infty}{}' (1+\delta_0) [D_n^p(\lambda')]^2}. \qquad (4.9d)
\end{aligned}$$

4.3 Dyadic Green's Functions

The unbounded dyadic Green's function was obtained by Tai [47] for $u \overset{>}{<} u_s$ in terms of elliptical vector wave functions:

$$\begin{aligned}
\overline{\boldsymbol{G}}_{eo}(\boldsymbol{r}, \boldsymbol{r}') = &-\frac{1}{k_1^2} \hat{\boldsymbol{u}} \hat{\boldsymbol{u}} \delta(\boldsymbol{r} - \boldsymbol{r}') + \frac{i}{2\pi} \int_{-\infty}^{\infty} dh \sum_m \frac{1}{\lambda^2 I_{e_{o}mn}} \\
&\times \begin{cases} \boldsymbol{M}_{e_{o}m\lambda}^{'(1)}(h) \boldsymbol{M}_{e_{o}m\lambda}(-h) + \boldsymbol{N}_{e_{o}m\lambda}^{'(1)}(h) \boldsymbol{N}_{e_{o}m\lambda}(-h), \\ \boldsymbol{M}_{e_{o}m\lambda}(h) \boldsymbol{M}_{e_{o}m\lambda}^{'(1)}(-h) + \boldsymbol{N}_{e_{o}m\lambda}(h) \boldsymbol{N}_{e_{o}m\lambda}^{'(1)}(-h); \end{cases} \qquad (4.10)
\end{aligned}$$

where u_s denotes the position of the source from the origin which is at the centre of the elliptical cylinder while λ and h satisfy the relation of $k^2 = \omega^2\mu\epsilon = \lambda^2 + h^2$. The expansion of a combination of even and odd means,

$$\boldsymbol{M}_{\substack{e\\o}m\lambda}(h)\boldsymbol{M}^{'(1)}_{\substack{e\\o}m\lambda}(-h) = \boldsymbol{M}_{em\lambda}(h)\boldsymbol{M}^{'(1)}_{em\lambda}(-h) + \boldsymbol{M}_{om\lambda}(h)\boldsymbol{M}^{'(1)}_{om\lambda}(-h). \tag{4.11}$$

The vector wave functions are expressed in terms of Mathieu functions below:

$$\boldsymbol{M}_{\substack{e\\o}m\lambda}(h) = \frac{1}{\beta}\Big[R_{\substack{e\\o}m\lambda}(u)\frac{\partial S_{\substack{e\\o}m\lambda}(v)}{\partial v}\widehat{\boldsymbol{u}} - S_{\substack{e\\o}m\lambda}(v)\frac{\partial R_{\substack{e\\o}m\lambda}(u)}{\partial u}\widehat{\boldsymbol{v}}\Big]e^{ihz}, \tag{4.12a}$$

$$\boldsymbol{M}^{(1)}_{\substack{e\\o}m\lambda}(h) = \frac{1}{\beta}\Big[R^{(1)}_{\substack{e\\o}m\lambda}(u)\frac{\partial S_{\substack{e\\o}m\lambda}(v)}{\partial v}\widehat{\boldsymbol{u}} - S_{\substack{e\\o}m\lambda}(v)\frac{\partial R^{(1)}_{\substack{e\\o}m\lambda}(u)}{\partial u}\widehat{\boldsymbol{v}}\Big]e^{ihz}, \tag{4.12b}$$

and

$$\boldsymbol{N}_{\substack{e\\o}m\lambda}(h) = \frac{1}{k\beta}\Big[ihS_{\substack{e\\o}m\lambda}(v)\frac{\partial R_{\substack{e\\o}m\lambda}(u)}{\partial u}\widehat{\boldsymbol{u}} + ihR_{\substack{e\\o}m\lambda}(u) + \frac{\partial S_{\substack{e\\o}m\lambda}(v)}{\partial v}\widehat{\boldsymbol{v}} + \beta\lambda^2 R_{\substack{e\\o}m\lambda}(u)S_{\substack{e\\o}m\lambda}(v)\widehat{\boldsymbol{z}}\Big]e^{ihz}, \tag{4.13a}$$

$$\boldsymbol{N}^{(1)}_{\substack{e\\o}m\lambda}(h) = \frac{1}{k\beta}\Big[ihS_{\substack{e\\o}m\lambda}(v)\frac{\partial R^{(1)}_{\substack{e\\o}m\lambda}(u)}{\partial u}\widehat{\boldsymbol{u}} + ihR^{(1)}_{\substack{e\\o}m\lambda}(u) + \frac{\partial S_{\substack{e\\o}m\lambda}(v)}{\partial v}\widehat{\boldsymbol{v}} + \beta\lambda^2 R^{(1)}_{\substack{e\\o}m\lambda}(u)S_{\substack{e\\o}m\lambda}(v)\widehat{\boldsymbol{z}}\Big]e^{ihz}. \tag{4.13b}$$

Subsequently, we consider two regions, namely, Region 1 outside of the dielectric cylinder (with permittivity ϵ_1 and permeability μ_1) and Region 2 inside of the dielectric cylinder (with permittivity ϵ_2 and permeability μ_2) . We can now assume that the scattering dyadic Green's functions due to an electric source in Region 1

are defined as:

$$\overline{\boldsymbol{G}}_{es}^{(11)}(\boldsymbol{r},\boldsymbol{r}') = \frac{i}{2\pi}\int_{-\infty}^{\infty} dh \sum_m \frac{1}{\eta^2 I_{emn}}\Big\{\Big[A_{\ o^m}^{e}\boldsymbol{M}_{e^{mn}}^{(1)}(h) + B_{\ e^m}^{o}\boldsymbol{N}_{o^{mn}}^{(1)}(h)\Big]\boldsymbol{M}_{e^{mn}}^{\prime(1)}(-h) + \Big[C_{\ o^m}^{e}\boldsymbol{N}_{e^{mn}}^{(1)}(h) + D_{\ e^m}^{o}\boldsymbol{M}_{o^{mn}}^{(1)}(h)\Big]\boldsymbol{N}_{e^{mn}}^{\prime(1)}(-h)\Big\}, \tag{4.14a}$$

$$\overline{\boldsymbol{G}}_{es}^{(21)}(\boldsymbol{r},\boldsymbol{r}') = \frac{i}{2\pi}\int_{-\infty}^{\infty} dh \sum_m \frac{1}{\xi^2 I_{o^{m\xi}}^{e}}\Big\{\Big[a_{\ o^m}^{e}\boldsymbol{M}_{\ o^{m\xi}}^{e}(h) + b_{\ e^m}^{o}\boldsymbol{N}_{\ e^{m\xi}}^{o}(h)\Big]\boldsymbol{M}_{e^{mn}}^{\prime(1)}(-h) + \Big[c_{\ o^m}^{e}\boldsymbol{N}_{\ o^{m\xi}}^{e}(h) + d_{\ e^m}^{o}\boldsymbol{M}_{\ e^{m\xi}}^{o}(h)\Big]\boldsymbol{N}_{e^{mn}}^{\prime(1)}(-h)\Big\}, \tag{4.14b}$$

where $A_{\ o^m}^{e}$, $B_{\ e^m}^{o}$, $C_{\ o^m}^{e}$, and $D_{\ e^m}^{o}$ represent the reflection coefficients while $a_{\ o^m}^{e}$, $b_{\ e^m}^{o}$, $c_{\ o^m}^{e}$, $d_{\ e^m}^{o}$ denote the transmission coefficients, $\eta = \sqrt{k_1^2 - h^2}$ and $\xi = \sqrt{k_2^2 - h^2}$ with $k_1 = \omega\sqrt{\mu_1\epsilon_1}$ and $k_2 = \omega\sqrt{\mu_2\epsilon_2}$. The first superscript in $\overline{\boldsymbol{G}}_{es}^{(11)}$ and $\overline{\boldsymbol{G}}_{es}^{(21)}$ corresponds to the region where the observation point is located while the second superscript corresponds to the region where the source is located and in the present case, the source is located in Region 1 only.

Using the principle of scattering superposition, we have

$$\overline{\boldsymbol{G}}_{e}^{(11)}(\boldsymbol{r},\boldsymbol{r}') = \overline{\boldsymbol{G}}_{eo}(\boldsymbol{r},\boldsymbol{r}') + \overline{\boldsymbol{G}}_{es}^{(11)}(\boldsymbol{r},\boldsymbol{r}'), \tag{4.15a}$$

$$\overline{\boldsymbol{G}}_{e}^{(21)}(\boldsymbol{r},\boldsymbol{r}') = \overline{\boldsymbol{G}}_{es}^{(21)}(\boldsymbol{r},\boldsymbol{r}'), \tag{4.15b}$$

where the eigenvalue λ in $\overline{\boldsymbol{G}}_{eo}(\boldsymbol{r},\boldsymbol{r}')$ should take the form of η. The boundary conditions at $u = u_o$ are satisfied by the dyadic Green's functions as follows [47]:

$$\widehat{\boldsymbol{u}} \times \Big[\overline{\boldsymbol{G}}_{e}^{(11)}(\boldsymbol{r},\boldsymbol{r}') - \overline{\boldsymbol{G}}_{e}^{(21)}(\boldsymbol{r},\boldsymbol{r}')\Big] = 0, \tag{4.16a}$$

$$\widehat{\boldsymbol{u}} \times \left[\frac{\nabla \times \overline{\boldsymbol{G}}_{e}^{(11)}(\boldsymbol{r},\boldsymbol{r}')}{\mu_1} - \frac{\nabla \times \overline{\boldsymbol{G}}_{e}^{(21)}(\boldsymbol{r},\boldsymbol{r}')}{\mu_2}\right] = 0. \tag{4.16b}$$

Substituting Eqs. (4.10), (4.14a), and (4.14b) into the boundary equations, we have for Eq. (4.16a):

$$\begin{aligned}
&\widehat{\boldsymbol{u}} \times \int_{-\infty}^{\infty} dh \sum_m \frac{1}{\eta^2 I_{\substack{e\\o}m\eta}} \Big[\Big(\boldsymbol{M}_{\substack{e\\o}m\eta}(h) \boldsymbol{M}'^{(1)}_{\substack{e\\o}m\eta}(-h) \\
&+ \boldsymbol{N}_{\substack{e\\o}m\eta}(h) \boldsymbol{N}'^{(1)}_{\substack{e\\o}m\eta}(-h) \Big) + \Big(A_{\substack{e\\o}m} \boldsymbol{M}^{(1)}_{\substack{e\\o}m\eta}(h) \\
&+ B_{\substack{o\\e}m} \boldsymbol{N}^{(1)}_{\substack{o\\e}m\eta}(h) \Big) \boldsymbol{M}'^{(1)}_{\substack{e\\o}m\eta}(-h) + \Big(C_{\substack{e\\o}m} \boldsymbol{N}^{(1)}_{\substack{e\\o}m\eta}(h) \\
&+ D_{\substack{o\\e}m} \boldsymbol{M}^{(1)}_{\substack{o\\e}m\eta}(h) \Big) \boldsymbol{N}'^{(1)}_{\substack{e\\o}m\eta}(-h) \Big] \\
&= \widehat{\boldsymbol{u}} \times \int_{-\infty}^{\infty} dh \sum_m \frac{1}{\xi^2 I_{\substack{e\\o}m\xi}} \Big[\Big(a_{\substack{e\\o}m} \boldsymbol{M}_{\substack{e\\o}m\xi}(h) \\
&+ b_{\substack{o\\e}m} \boldsymbol{N}_{\substack{o\\e}m\xi}(h) \Big) \boldsymbol{M}'^{(1)}_{\substack{e\\o}m\eta}(-h) + \Big(c_{\substack{e\\o}m} \boldsymbol{N}_{\substack{e\\o}m\xi}(h) \\
&+ d_{\substack{o\\e}m} \boldsymbol{M}_{\substack{o\\e}m\xi}(h) \Big) \boldsymbol{N}'^{(1)}_{\substack{e\\o}m\eta}(-h) \Big];
\end{aligned} \tag{4.17a}$$

and for Eq. (4.16b):

$$\begin{aligned}
&\widehat{\boldsymbol{u}} \times \int_{-\infty}^{\infty} dh \sum_m \frac{k_1}{\eta^2 I_{\substack{e\\o}m\eta}} \Big[\Big(\boldsymbol{N}_{\substack{e\\o}m\eta}(h) \boldsymbol{M}'^{(1)}_{\substack{e\\o}m\eta}(-h) \\
&+ \boldsymbol{M}_{\substack{e\\o}m\eta}(h) \boldsymbol{N}'^{(1)}_{\substack{e\\o}m\eta}(-h) \Big) + \Big(A_{\substack{e\\o}m} \boldsymbol{N}^{(1)}_{\substack{e\\o}m\eta}(h) \\
&+ B_{\substack{o\\e}m} \boldsymbol{M}^{(1)}_{\substack{o\\e}m\eta}(h) \Big) \boldsymbol{M}'^{(1)}_{\substack{e\\o}m\eta}(-h) + \Big(C_{\substack{e\\o}m} \boldsymbol{M}^{(1)}_{\substack{e\\o}m\eta}(h) \\
&+ D_{\substack{o\\e}m} \boldsymbol{N}^{(1)}_{\substack{o\\e}m\eta}(h) \Big) \boldsymbol{N}'^{(1)}_{\substack{e\\o}m\eta}(-h) \Big] \\
&= \frac{1}{\mu_r} \widehat{\boldsymbol{u}} \times \int_{-\infty}^{\infty} dh \sum_m \frac{k_2}{\xi^2 I_{\substack{e\\o}m\xi}} \Big[\Big(a_{\substack{e\\o}m} \boldsymbol{N}_{\substack{e\\o}m\xi}(h) \\
&+ b_{\substack{o\\e}m} \boldsymbol{M}_{\substack{o\\e}m\xi}(h) \Big) \boldsymbol{M}'^{(1)}_{\substack{e\\o}m\eta}(-h) + \Big(c_{\substack{e\\o}m} \boldsymbol{M}_{\substack{e\\o}m\xi}(h) \\
&+ d_{\substack{o\\e}m} \boldsymbol{N}_{\substack{o\\e}m\xi}(h) \Big) \boldsymbol{N}'^{(1)}_{\substack{e\\o}m\eta}(-h) \Big].
\end{aligned} \tag{4.17b}$$

These two equations will be solved later for the scattering coefficients.

4.4 Equations Satisfied by Scattering Coefficients

After formulating the dyadic Green's functions and obtaining the general set of boundary equations, we can now apply them to practical radiation problems. To analyze EM radiatiation, an infinitely long transmission line source with an electric current density of the following form is assumed:

$$\boldsymbol{J}(\boldsymbol{r}') = E_o \frac{\delta(u'-u_s)\delta(v'-\alpha)}{\beta^2} e^{-ik_1\cos\gamma z'}\widehat{\boldsymbol{z}}. \tag{4.18}$$

It can be shown that the volume integral of the scalar product of the electric current source and the vector wave functions are as follows:

$$\Phi_M = \int\int\int_{V'} \boldsymbol{M}'^{(1)}_{\substack{e\\o}m\eta}(-h)\cdot\boldsymbol{J}(\boldsymbol{r}')dV' = 0, \tag{4.19a}$$

$$\begin{aligned}\Phi_N &= \int\int\int_{V'} \boldsymbol{N}'^{(1)}_{\substack{e\\o}m\eta}(-h)\cdot\boldsymbol{J}(\boldsymbol{r}')dV' \\ &= \frac{\eta^2}{k_1} R^{(1)}_{\substack{e\\o}m\eta}(u_s) S_{\substack{e\\o}m\eta}(\alpha) E_o 2\pi\delta(h+k_1\cos\gamma).\end{aligned} \tag{4.19b}$$

Using these above relations, we can scalarly multiply both sides of (4.17a) and (4.17b) with the current density and then simplify them into the following equations: from (4.17a),

$$\begin{aligned}\widehat{\boldsymbol{u}}\times\sum_m \frac{R^{(1)}_{\substack{e\\o}m\eta}(u_s)}{\eta^2 I_{\substack{e\\o}m\eta}}\Big\{\Big[&\boldsymbol{N}_{\substack{e\\o}m\eta}(-k_1\cos\gamma) + C_{\substack{e\\o}m} \\ &\times\boldsymbol{N}^{(1)}_{\substack{e\\o}m\eta}(-k_1\cos\gamma) + D_{\substack{o\\e}m}\boldsymbol{M}^{(1)}_{\substack{o\\e}m\eta}(-k_1\cos\gamma)\Big] S_{\substack{e\\o}m\eta}(\alpha)\Big\} \\ = \widehat{\boldsymbol{u}}\times\sum_m \frac{R^{(1)}_{\substack{e\\o}m\eta}(u_s)}{\xi^2 I_{\substack{e\\o}m\xi}}\Big\{\Big[&c_{\substack{e\\o}m}\boldsymbol{N}_{\substack{e\\o}m\xi}(-k_1\cos\gamma) + d_{\substack{o\\e}m} \\ &\times\boldsymbol{M}_{\substack{o\\e}m\xi}(-k_1\cos\gamma)\Big] S_{\substack{e\\o}m\eta}(\alpha)\Big\};\end{aligned} \tag{4.20a}$$

and from (4.17b),

$$\widehat{\boldsymbol{u}}\times\sum_m \frac{R^{(1)}_{\substack{e\\o}m\eta}(u_s)k_1}{\eta^2 I_{\substack{e\\o}m\eta}}\Big\{\Big[\boldsymbol{M}_{\substack{e\\o}m\eta}(-k_1\cos\gamma) + C_{\substack{e\\o}m}$$

$$\times \boldsymbol{M}^{(1)}_{{}^{e}_{o}m\eta}(-k_1\cos\gamma) + D_{{}^{o}_{e}m}\boldsymbol{N}^{(1)}_{{}^{o}_{e}m\eta}(-k_1\cos\gamma)\Big]S_{{}^{e}_{o}m\eta}(\alpha)\Big\}$$
$$= \frac{1}{\mu_r}\widehat{\boldsymbol{u}} \times \sum_m \frac{R^{(1)}_{{}^{e}_{o}m\eta}(u_s)k_2}{\xi^2 I_{{}^{e}_{o}m\xi}}\Big\{\Big[c_{{}^{e}_{o}m}\boldsymbol{M}_{{}^{e}_{o}m\xi}(-k_1\cos\gamma)$$
$$+ d_{{}^{o}_{e}m}\boldsymbol{N}_{{}^{o}_{e}m\xi}(-k_1\cos\gamma)\Big]S_{{}^{e}_{o}m\eta}(\alpha)\Big\}. \tag{4.20b}$$

These equations, i.e., (4.20a) and (4.20b) can be further simplified by substituting the vector wave functions in terms of the Mathieu functions in Eqs. (4.12a) to (4.13b) and decomposing the $\widehat{\boldsymbol{v}}$- and $\widehat{\boldsymbol{z}}$-components. These decomposed equations can then be further simplified by applying the orthogonal properties of the Mathieu functions from (4.6a) to (4.6c) and some special properties of the Mathieu functions in term of different wavenumbers in (4.8a) to (4.8d). With this process, eight equations (4 upper subscript cases and 4 lower subscript cases) can be obtained:

$$C_{{}^{e}_{o}q} = \frac{1}{S_{{}^{e}_{o}q\eta}(\alpha)}\sum_{m=0}^{\infty}{}' \frac{R^{(1)}_{{}^{e}_{o}m\eta}(u_s)}{R^{(1)}_{{}^{e}_{o}q\eta}(u_s)}\frac{I_{{}^{e}_{o}q\eta}}{I_{{}^{e}_{o}m\xi}}\Big[c_{{}^{e}_{o}m}\frac{k_1}{k_2}\frac{R_{{}^{e}_{o}m\xi}(u)}{R^{(1)}_{{}^{e}_{o}q\eta}(u)}$$
$$\times \chi^{e}_{{}^{o}mq}S_{{}^{e}_{o}m\eta}(\alpha)\Big] - \frac{R_{{}^{e}_{o}q\eta}(u)}{R^{(1)}_{{}^{e}_{o}q\eta}(u)}, \tag{4.21a}$$

$$D_{{}^{e}_{o}q} = \frac{1}{\mu_r S_{{}^{o}_{e}q\eta}(\alpha)}\sum_{m=1}^{\infty}{}' \frac{R^{(1)}_{{}^{e}_{o}m\eta}(u_s)}{R^{(1)}_{{}^{e}_{o}q\eta}(u_s)}\frac{I_{{}^{o}_{e}q\eta}}{I_{{}^{o}_{e}m\xi}}\Big[d_{{}^{e}_{o}m}\frac{R_{{}^{e}_{o}m\xi}(u)}{R^{(1)}_{{}^{e}_{o}q\eta}(u)}$$
$$\times \chi^{e}_{{}^{o}mq}S_{{}^{o}_{e}m\eta}(\alpha)\Big]; \tag{4.21b}$$

and

$$\sum_{m=0}^{\infty}{}' \frac{R^{(1)}_{{}^{e}_{o}m\eta}(u_s)}{I_{{}^{e}_{o}m\xi}} i\cos\gamma c_{{}^{e}_{o}m}\frac{k_1}{k_2}R_{{}^{e}_{o}m\xi}(u)S_{{}^{e}_{o}m\eta}(\alpha)\Big(\frac{1}{\eta^2}$$
$$-\frac{1}{\xi^2}\Big)\sum_{r=0}^{\infty}{}' \chi^{e}_{{}^{o}mr}\zeta_{{}^{e}_{o}rq} = \sum_{m=1}^{\infty}{}' \frac{R^{(1)}_{{}^{e}_{o}m\eta}(u_s)}{I_{{}^{e}_{o}m\xi}} d_{{}^{o}_{e}m}S_{{}^{e}_{o}m\eta}(\alpha)\chi^{o}_{{}^{e}mq}$$
$$\times\Big[\frac{1}{\xi^2}\frac{\partial}{\partial u}R_{{}^{o}_{e}q\xi}(u) - \frac{1}{\eta^2\mu_r}\frac{R_{{}^{o}_{e}m\xi}(u)}{R^{(1)}_{{}^{o}_{e}q\eta}(u)}\frac{\partial}{\partial u}R^{(1)}_{{}^{o}_{e}q\eta}(u)\Big], \tag{4.22a}$$

$$\sum_{m=1}^{\infty}{}' \frac{R^{(1)}_{{}^{o}_{e}m\eta}(u_s)}{\mu_r}\frac{I_{{}^{o}_{e}q\eta}}{I_{{}^{o}_{e}m\xi}} i\cos\gamma d_{{}^{o}_{e}m}R_{{}^{e}_{o}m\xi}(u)S_{{}^{o}_{e}m\eta}(\alpha)$$

$$\times\left(\frac{1}{\eta^2}-\frac{1}{\xi^2}\right)\sum_{r=0}^{\infty}{}'\chi^{e}_{o^{mr}}\zeta^{e}_{o^{rq}}+\frac{R^{(1)}_{o_{e^{q\eta}}}(u_s)}{\eta^2}S^{o}_{e^{q\eta}}(\alpha)$$
$$\times\left[\frac{\partial}{\partial u}R^{o}_{e^{q\eta}}(u)-\frac{R^{o}_{e^{q\eta}}(u)}{R^{(1)}_{o_{e^{q\eta}}}(u)}\frac{\partial}{\partial u}R^{(1)}_{o_{e^{q\eta}}}(u)\right]$$
$$=\sum_{m=1}^{\infty}{}'R^{(1)}_{o_{e^{m\eta}}}(u_s)\frac{I^{o}_{e^{q\eta}}}{I^{o}_{e^{m\xi}}}c^{o}_{e^{m}}\chi^{o}_{e^{mq}}S^{o}_{e^{m\eta}}(\alpha)\left[\frac{k_2}{\xi^2\mu_r k_1}\right.$$
$$\left.\times\frac{\partial}{\partial u}R^{o}_{e^{m\xi}}(u)-\frac{k_1}{\eta^2 k_2}\frac{R^{o}_{e^{m\xi}}(u)}{R^{(1)}_{o_{e^{q\eta}}}(u)}\frac{\partial}{\partial u}R^{(1)}_{o_{e^{q\eta}}}(u)\right]. \tag{4.22b}$$

Equations (4.22a) to (4.22b) are satisfied by the transmission coefficients. They are then solved by using the matrix operations by varying q. The reflection coefficients are then solved by substituting the transmission coefficients into Eqs. (4.21a) to (4.21b). From Eqs. (4.22a) to (4.22b) we can write

$$[\Gamma_e]\cdot[C_{even}]=[\Delta_o]\cdot[D_{odd}], \tag{4.23a}$$

$$[\Gamma_o]\cdot[C_{odd}]=[\Delta_e]\cdot[D_{even}], \tag{4.23b}$$

$$[\Xi_e]\cdot[D_{even}]+[\Omega_{eq}]=[\Psi_o]\cdot[C_{odd}], \tag{4.23c}$$

$$[\Xi_o]\cdot[D_{odd}]+[\Omega_{oq}]=[\Psi_e]\cdot[C_{even}], \tag{4.23d}$$

where

$$\Omega^{e}_{o^{q}}=\frac{R^{(1)}_{e_{o^{q\eta}}}(u_s)}{\eta^2}S^{e}_{o^{q\eta}}(\alpha)\left[\frac{\partial}{\partial u}R^{e}_{o^{q\eta}}(u)\right.$$
$$\left.-\frac{R^{e}_{o^{q\eta}}(u)}{R^{(1)}_{e_{o^{q\eta}}}(u)}\frac{\partial}{\partial u}R^{(1)}_{e_{o^{q\eta}}}(u)\right], \tag{4.24a}$$

$$\Gamma^{e}_{o(q,m)}=\frac{R^{(1)}_{e_{o^{m\eta}}}(u_s)}{I^{e}_{o^{m\xi}}}i\cos\gamma\frac{k_1}{k_2}R^{e}_{o^{m\xi}}(u)S^{e}_{o^{m\eta}}(\alpha)$$
$$\times\left(\frac{1}{\eta^2}-\frac{1}{\xi^2}\right)\sum_{r=0}^{\infty}{}'\chi^{e}_{o^{mr}}\zeta^{e}_{o^{rq}}, \tag{4.24b}$$

$$\Delta^{e}_{o(q,m)}=\frac{R^{(1)}_{o_{e^{m\eta}}}(u_s)}{I^{o}_{e^{m\xi}}}S^{o}_{e^{m\eta}}(\alpha)\chi^{e}_{o^{mq}}\left[\frac{1}{\xi^2}\frac{\partial}{\partial u}R^{e}_{o^{q\xi}}(u)\right.$$

$$- \frac{1}{\eta^2 \mu_r} \frac{R_{e_{o^{m\xi}}}(u)}{R^{(1)}_{e_{o^{q\eta}}}(u)} \frac{\partial}{\partial u} R^{(1)}_{e_{o^{q\eta}}}(u) \Big], \tag{4.24c}$$

$$\Xi^{e}_{o(q,m)} = \frac{R^{(1)}_{o_{e^{m\eta}}}(u_s)}{\mu_r} \frac{I_{o_{e^{q\eta}}}}{I_{o_{e^{m\xi}}}} i \cos\gamma R_{e_{o^{m\xi}}}(u) S_{o_{e^{m\eta}}}(\alpha) \times \left(\frac{1}{\eta^2} - \frac{1}{\xi^2} \right) \sum_{r=0}^{\infty\,\prime} \chi^{e}_{o^{mr}} \zeta^{e}_{o^{rq}}, \tag{4.24d}$$

$$\Psi^{e}_{o(q,m)} = R^{(1)}_{e_{o^{m\eta}}}(u_s) \frac{I_{e_{o^{q\eta}}}}{I_{e_{o^{m\xi}}}} \chi^{e}_{o^{mq}} S_{e_{o^{m\eta}}}(\alpha) \Big[\frac{k_2}{\xi^2 \mu_r k_1} \times \frac{\partial}{\partial u} R_{e_{o^{m\xi}}}(u) - \frac{k_1}{\eta^2 k_2} \frac{R_{e_{o^{m\xi}}}(u)}{R^{(1)}_{e_{o^{q\eta}}}(u)} \frac{\partial}{\partial u} R^{(1)}_{e_{o^{q\eta}}}(u) \Big]; \tag{4.24e}$$

$$[C_{even}] = \begin{pmatrix} c_{e0} \\ c_{e1} \\ c_{e2} \\ c_{e3} \\ \vdots \\ c_{eN-1} \end{pmatrix}, \quad [C_{odd}] = \begin{pmatrix} c_{o1} \\ c_{o2} \\ c_{o3} \\ c_{o4} \\ \vdots \\ c_{oN} \end{pmatrix}, \tag{4.25a}$$

$$[D_{even}] = \begin{pmatrix} d_{e1} \\ d_{e2} \\ d_{e3} \\ d_{e4} \\ \vdots \\ d_{eN} \end{pmatrix}, \quad [D_{odd}] = \begin{pmatrix} d_{o1} \\ d_{o2} \\ d_{o3} \\ d_{o4} \\ \vdots \\ d_{oN} \end{pmatrix}. \tag{4.25b}$$

In the next section, the electric field expressions will be obtained.

4.5 Far Field Expressions

The radiated electric field in free space due to the transmission line in the absence of the cylinder are expressed as:

$$\begin{aligned}
\boldsymbol{E}^{free}(\boldsymbol{r}) &= i\omega\mu_o \int\int\int_{V'} \overline{\boldsymbol{G}}_{eo}(\boldsymbol{r},\boldsymbol{r}') \cdot \boldsymbol{J}(\boldsymbol{r}')dV' \\
&= i\omega\mu_o \int\int\int_{v'} \frac{i}{2\pi} \int_{-\infty}^{\infty} dh \sum_m \frac{1}{\eta^2 I_{\substack{e\\o}m\eta}} \\
&\quad \times \boldsymbol{N}^{(1)}_{\substack{e\\o}m\eta}(h)\boldsymbol{N}'_{\substack{e\\o}m\eta}(-h) \cdot \boldsymbol{J}(\boldsymbol{r}')dV' \\
&= -\omega\mu_o \sum_m \frac{E_o}{k_1 I_{\substack{e\\o}m\eta}} \boldsymbol{N}^{(1)}_{\substack{e\\o}m\eta}(-k_1\cos\gamma) \\
&\quad \times R_{\substack{e\\o}m\eta}(u_s) S_{\substack{e\\o}m\eta}(\alpha).
\end{aligned} \tag{4.26a}$$

The scattered electric field can be found from:

$$\begin{aligned}
\boldsymbol{E}^s(\boldsymbol{r}) &= i\omega\mu_o \iiint_{V'} \overline{\boldsymbol{G}}^{(11)}_{es}(\boldsymbol{r},\boldsymbol{r}') \cdot \boldsymbol{J}(\boldsymbol{r}')dV', \\
&= i\omega\mu_o \iiint_{v'} \frac{i}{2\pi} \int_{-\infty}^{\infty} dh \sum_m \frac{1}{\eta^2 I_{\substack{e\\o}m\eta}} \Big[C_{\substack{e\\o}m} \boldsymbol{N}^{(1)}_{\substack{e\\o}m\eta}(h) \\
&\quad + D_{\substack{o\\e}m} \boldsymbol{M}^{(1)}_{\substack{o\\e}m\eta}(h) \Big] \boldsymbol{N}'^{(1)}_{\substack{e\\o}m\eta}(-h) \cdot \boldsymbol{J}(\boldsymbol{r}')dV', \\
&= -\omega\mu_o \sum_m \frac{E_o}{k_1\eta^2 I_{\substack{e\\o}m\eta}} \Big[C_{\substack{e\\o}m} \boldsymbol{N}^{(1)}_{\substack{e\\o}m\eta}(-k_1\cos\gamma) \\
&\quad + D_{\substack{o\\e}m} \boldsymbol{M}^{(1)}_{\substack{o\\e}m\eta}(-k_1\cos\gamma) \Big] R^{(1)}_{\substack{e\\o}m\eta}(u_s) S_{\substack{e\\o}m\eta}(\alpha).
\end{aligned} \tag{4.26b}$$

The total electric field in the outer region of the cylindrical structure is

$$\boldsymbol{E}^{total} = \boldsymbol{E}^{free} + \boldsymbol{E}^s. \tag{4.27}$$

Explicitly, we can write the components of the free-space electric field by expressing the vector wave functions in terms of Mathieu functions as follows:

$$E_u^{free} = \omega\mu_o \sum_m \frac{E_o}{k_1 I_{\substack{e\\o}m\eta}} \frac{i\cos\gamma}{\beta} \frac{\partial R^{(1)}_{\substack{e\\o}m\eta}(u)}{\partial u} S_{\substack{e\\o}m\eta}(v)$$

$$\times R^{e}_{o}{}_{m\eta}(u_s)S^{e}_{o}{}_{m\eta}(\alpha)e^{-ik_1\cos\gamma z}, \tag{4.28a}$$

$$E_v^{free} = \omega\mu_o \sum_m \frac{E_o}{k_1 I^{e}_{o}{}_{m\eta}} \frac{i\cos\gamma}{\beta} \frac{\partial S^{e}_{o}{}_{m\eta}(v)}{\partial v} R^{(1)e}_{o}{}_{m\eta}(u)$$
$$\times R^{e}_{o}{}_{m\eta}(u_s)S^{e}_{o}{}_{m\eta}(\alpha)e^{-ik_1\cos\gamma z}, \tag{4.28b}$$

$$E_z^{free} = -\omega\mu_o \sum_m \frac{E_o}{k_1 I^{e}_{o}{}_{m\eta}} \frac{\eta^2}{k1} S^{e}_{o}{}_{m\eta}(v) R^{(1)e}_{o}{}_{m\eta}(u)$$
$$\times R^{e}_{o}{}_{m\eta}(u_s)S^{e}_{o}{}_{m\eta}(\alpha)e^{-ik_1\cos\gamma z}. \tag{4.28c}$$

The components of the scattered electric field are:

$$E_u^s = -\sqrt{\frac{\mu_o}{\epsilon_o}} \sum_m \frac{E_o}{I^{e}_{o}{}_{m\eta}} \Big[C^{e}_{o}{}_{om} \frac{-i\cos\gamma}{\beta} \frac{\partial R^{(1)}_{e}{}_{o}{}_{m\eta}(u)}{\partial u}$$
$$S^{e}_{o}{}_{m\eta}(v) + \frac{D^{o}_{e}{}_{m}}{\beta} \frac{\partial S^{o}_{e}{}_{m\eta}(v)}{\partial v} R^{o}_{e}{}_{m\eta}(u) \Big] R^{(1)e}_{o}{}_{m\eta}(u_s)$$
$$S^{e}_{o}{}_{m\eta}(\alpha)e^{-ik_1\cos\gamma z}, \tag{4.29a}$$

$$E_v^s = -\sqrt{\frac{\mu_o}{\epsilon_o}} \sum_m \frac{E_o}{I^{e}_{o}{}_{m\eta}} \Big[C^{e}_{o}{}_{om} \frac{-i\cos\gamma}{\beta} R^{(1)e}_{o}{}_{m\eta}(u) \frac{\partial S^{e}_{o}{}_{m\eta}(v)}{\partial v}$$
$$- \frac{D^{o}_{e}{}_{m}}{\beta} S^{o}_{e}{}_{m\eta}(v) \frac{\partial R^{(1)}_{o}{}_{e}{}_{m\eta}(u)}{\partial u} \Big] R^{(1)e}_{o}{}_{m\eta}(u_s) S^{e}_{o}{}_{m\eta}(\alpha)$$
$$\times e^{-ik_1\cos\gamma z}, \tag{4.29b}$$

$$E_z^s = -\sqrt{\frac{\mu_o}{\epsilon_o}} \sum_m \frac{E_o}{I^{e}_{o}{}_{m\eta}} \Big[C^{e}_{o}{}_{om} \frac{\eta^2}{k_1} R^{(1)e}_{o}{}_{m\eta}(u) S^{e}_{o}{}_{m\eta}(v) \Big]$$
$$\times R^{(1)e}_{o}{}_{m\eta}(u_s) S^{e}_{o}{}_{m\eta}(\alpha) e^{-ik_1\cos\gamma z}. \tag{4.29c}$$

Using the asympotic expression of the radial Mathieu functions of the third kind [79] given below

$$R^{(1)}_{em\eta}(u_s) \longrightarrow \frac{e^{i(\eta r_s - \frac{2m+1}{4}\pi)}}{\sqrt{\eta r_s}}, \tag{4.30a}$$

$$R^{(1)}_{om\eta}(u_s) \longrightarrow \frac{e^{i(\eta r_s - \frac{2m+1}{4}\pi)}}{\sqrt{\eta r_s}}, \tag{4.30b}$$

where r_s represents the cylindrical radial coordinate, we can rewrite the components of the free-space electric field in far zone as follows:

$$E_r^{free} = \sqrt{\frac{\mu_o}{\epsilon_o}} \sum_m \frac{(-i)^m \eta E_o}{\sqrt{\eta r} I_{\substack{e\\o}m\eta}} i \cos\gamma S_{\substack{e\\o}m\eta}(\phi) S_{\substack{e\\o}m\eta}(\alpha) \times R_{\substack{e\\o}m\eta}(u_s) e^{-ik_1 \cos\gamma z} e^{i\eta r - \frac{\pi}{4}}, \tag{4.31a}$$

$$E_z^{free} = -\sqrt{\frac{\mu_o}{\epsilon_o}} \sum_m \frac{(-i)^m E_o}{\sqrt{\eta r} I_{\substack{e\\o}m\eta}} \frac{\eta^2}{k1} S_{\substack{e\\o}m\eta}(\phi) R_{\substack{e\\o}m\eta}(u_s) \times S_{\substack{e\\o}m\eta}(\alpha) e^{-ik_1 \cos\gamma z} e^{i\eta r - \frac{\pi}{4}}. \tag{4.31b}$$

The components of the far scattered electric field can be written as:

$$E_r^s = -\sqrt{\frac{\mu_o}{\epsilon_o}} \sum_m \frac{(-i)^m \eta E_o}{I_{\substack{e\\o}m\eta}} C_{\substack{e\\o}m} \frac{-i\cos\gamma}{\sqrt{\eta r}} S_{\substack{e\\o}m\eta}(\phi) \times R^{(1)}_{\substack{e\\o}m\eta}(u_s) S_{\substack{e\\o}m\eta}(\alpha) e^{-ik_1 \cos\gamma z} e^{i\eta r - \frac{\pi}{4}}, \tag{4.32a}$$

$$E_\phi^s = \sqrt{\frac{\mu_o}{\epsilon_o}} \sum_m \frac{(-i)^m \eta E_o}{\sqrt{\eta r} I_{\substack{e\\o}m\eta}} D_{\substack{o\\e}m} S_{\substack{o\\e}m\eta}(\phi) R^{(1)}_{\substack{e\\o}m\eta}(u_s) \times S_{\substack{e\\o}m\eta}(\alpha) e^{-ik_1 \cos\gamma z} e^{i\eta r - \frac{\pi}{4}}, \tag{4.32b}$$

$$E_z^s = -\sqrt{\frac{\mu_o}{\epsilon_o}} \sum_m \frac{(-i)^m E_o}{\sqrt{\eta r} I_{\substack{e\\o}m\eta}} C_{\substack{e\\o}m} \frac{\eta^2}{k_1} S_{\substack{e\\o}m\eta}(v) R^{(1)}_{\substack{e\\o}m\eta}(u_s) \times S_{\substack{e\\o}m\eta}(\alpha) e^{-ik_1 \cos\gamma z} e^{i\eta r - \frac{\pi}{4}}. \tag{4.32c}$$

4.6 Numerical Results

The scattered and total electric fields normalized by the far field $\sqrt{\frac{\mu_o}{\eta\epsilon_o r}}\ |\boldsymbol{E}^{free}|$ are numerically computed and plotted for several cases. The transmission line source is placed at several distances with respect to the elliptical cylinder. We have also considered various effects (including lossless and lossy effects) of dielectric media at different frequencies and for various cylinder dimensions. For ease of comparison

and convenience of drawing meanful conclusion, we assume the cross section area of the elliptical cylinder remains unchanged while the shape of the cylindrical cross section varies. For each of the figures, we also assumed that $a/b = 2.0$, 3.75, and 15.1, respectively while ka is assumed to be 0.73, 1.00, and 2.00 correspondingly.

Figures 4.3(a) and 4.3(b) show the normalized scattered and total electric fields in the lossless case (where $\epsilon_r = 2.0$), respectively, when the transmission line source is placed at $u_s = 2a$ and $\alpha = 180$ (on the major axis at a relatively large distance).

It is observed that when the elliptic shape is close to a sphere, the scattered electric field seems to be the largest; and it becomes smallest when the elliptic shape is very oblate. Physically, it is understandable as the physical area that blocks the wave propagation varies with the shape of the cylinder. The larger the blocking area, the more the energy is reflected. It is also seen that the field radiated directly from the transmission line may have a different phase from the field reflected by the cylinder. So, the stronger scattered field does not mean the total field is also stronger, as seen from Figs. 4.3(a) and 4.3(b). In certain angles, the field is enhanced because of the in-phase summation; while in some other angles, the field can be very low because of the opposite phase and its resulted cancelation of the field. Another observation is that the electric field radiated directly from the transmission line dominates the total electric field.

To see the effects of the lossy materials, Figs. 4.4(a) and 4.4(b) show the normalized scattered and total electric fields in the lossy case (where $\epsilon_r = 2.0 + i2.0$), respectively. The other parameters used in Figs. 4.4(a) and 4.4(b) are the same as

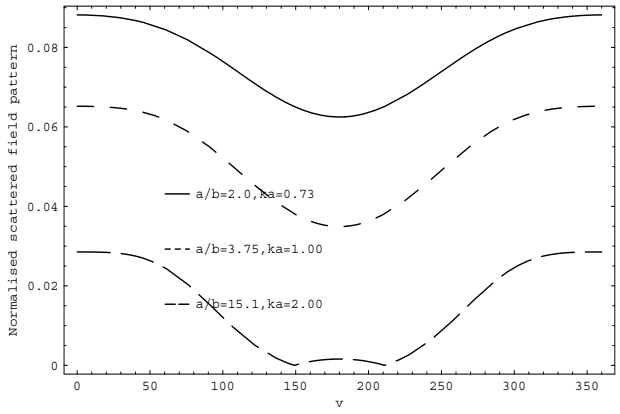

(a) Normalized scattered electric field.

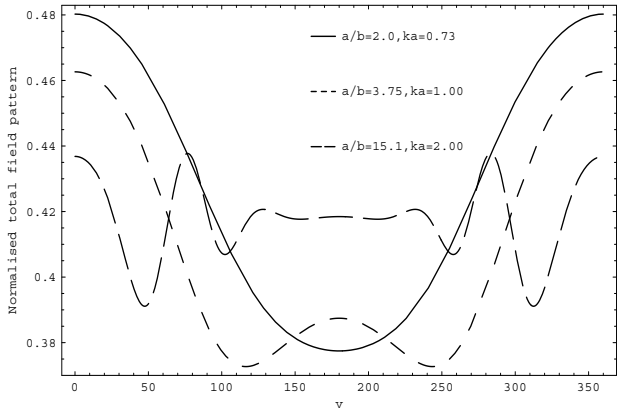

(b) Normalized total electric field.

Figure 4.3: Normalized scattered and total electric fields for $u_s = 2a$, $\epsilon_r = 2.0$ and $\alpha = 180^o$.

those used in Figs. 4.3(a) and 4.3(b).

From Figs. 4.4(a) and 4.4(b), it is seen that the magnitude of field scattered by a lossy cylinder is even larger than that by a lossless cylinder. This scattering enhancement phenomena can be explained as more of the waves are reflected back due to the lossy nature of the dielectric. However, it is also seen from Figs. 4.3(a) and 4.3(b) that the magnitude of the total electric field in the presence of the lossy cylinder is smaller than that in the presence of the lossless cylinder. This is simply because some of the power is absorbed by the lossy material. At $\phi = 180^o$, the backscattering effects for the lossy dielectric media become very strong.

Figures 4.5(a) and 4.5(b) show the normalised scattered and total electric field for the lossless case (where $\epsilon_r = 2.0$, and the transmission line is placed nearer to the cylinder at $u_s = 1.2a$ and $\alpha = 180^o$. Comparing these in Figs. 4.3(a) and 4.3(b) where the source is placed at $u_s = 2a$, it is seen that magnitude of the scattered field increases, but the pattern does not change drastically as the line source is moved closer to the cylindrical waveguide along the ellipse' major axis while the total electric field also increases slightly in magnitude. In the case where $k_1 a = 2.00$, the oscillations appearing in the total field distribution decrease when the line source is moved closer to the cylinder.

So far, we have looked into various effects of elliptic cylinder's shape, the line source's distance, the cylinder's dielectric material property on both scattered and total electric fields, when the tranmission line is located in the ellipse's major axis. Subsequently, we will invetigate those effects when the tranmission line is located

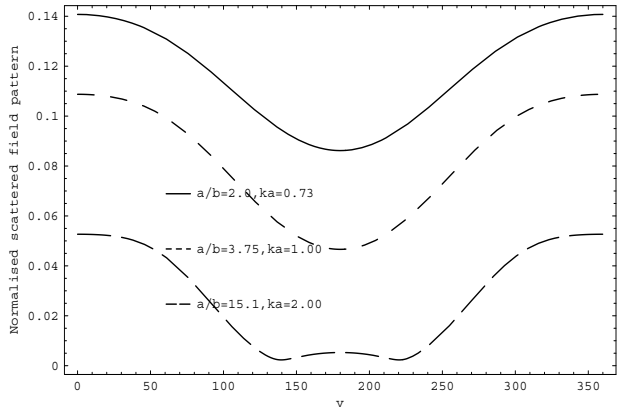

(a) Normalized scattered electric field.

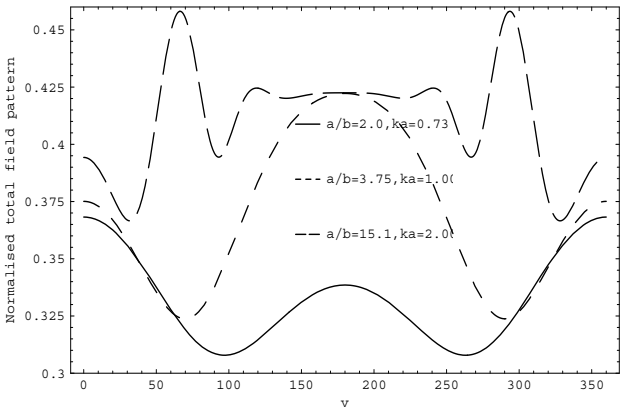

(b) Normalized total electric field.

Figure 4.4: Normalized scattered and total electric fields for $u_s = 2a$, $\epsilon_r = 2.0 + i2.0$ and $\alpha = 180^o$.

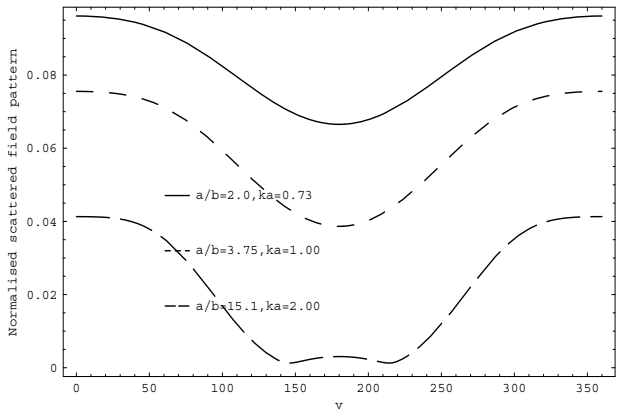

(a) Normalized scattered electric field.

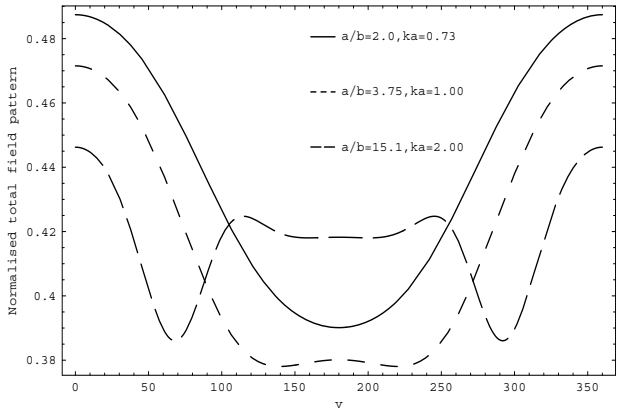

(b) Normalized total electric field.

Figure 4.5: Normalized scattered and total electric fields for $u_s = 1.2a$, $\epsilon_r = 2.0$ and $\alpha = 180^o$.

in the ellipse's minor axis. Figs. 4.6(a) and 4.6(b) show the normalized scattered and total electric fields in the lossless case where $\epsilon_r = 2.0$ and the transmission line source is placed along the minor axis nearer to the cylinder at $u_s = 2b$ and $\alpha = 270^o$. In the present case, the radial distance is shorter than that in Figs. 4.3(a) and 4.3(b) and the area that blocks the wave propagation along the minor axis is increased. It is seen from Figs. 4.6(a) and 4.6(b) that the distribution pattern of the scattered wave changes dramatically. Similar to the previous cases that we considered, the oscillation in the scattered field distribution occurs and its magnitude is small when the ellipse is close to a sphere in shape but is very large when the ellipse is very oblate in shape (and close to a plate). Also, it is found that backscattering is very strong but the forward scattering is even stronger. In other words, the scattered field along the major axis becomes quite weak. It is also found that when the transmission line is located in the minor axis direction, the total field distribution pattern varies with the shape of the ellipse, but its tendency does not change too much with shape. An important observation is that in this case, neither the backscattering nor the forward scattering is strong and a maximum occurs at an angle of about 50^o. This maximum varies with the shape of the ellipse slightly.

To see effects of the radial distance further in the present case, Figs. 4.7(a) and 4.7(b) show the normalized scattered and total electric fields in the lossless case where $\epsilon_r = 2.0$ and the transmission line source is placed along the minor axis nearer to the cylinder at $u_s = 1.2b$ and $\alpha = 270^o$. The similar observation to that in Figs. 4.6(a) and 4.6(b) is found. However, magnitudes of both scattered and total electric fields in Figs. 4.7(a) and 4.7(b) are, in general, larger than those magnitudes

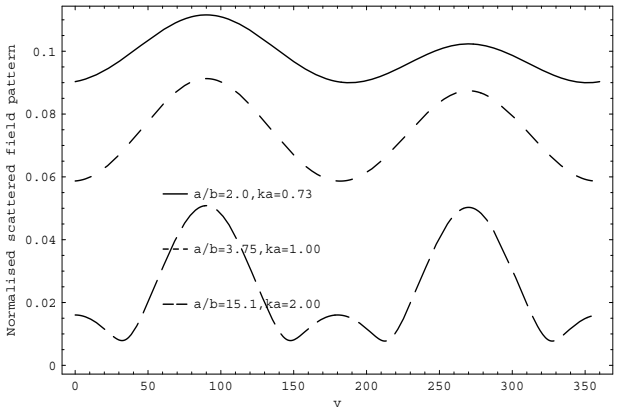

(a) Normalized scattered electric field.

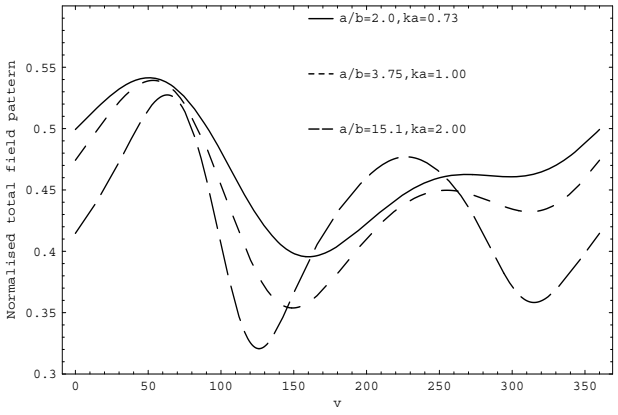

(b) Normalized total electric field.

Figure 4.6: Normalized scattered and total electric fields for $u_s = 2b$, $\epsilon_r = 2.0$ and $\alpha = 270^o$.

in Figs. 4.6(a) and 4.6(b). Also, the elliptical waveguide's shapes varying from a sphere to an oblate ellipse make more significant difference in both the scattered and the total electric fields. For the total electric field, we notice a slight increase in magnitude and for the case where $k_1 a = 2.00$ the field pattern changes slightly as the line source is moved closer to the cylinder. A similar observation is also made, that is, neither the backscattering nor the forward scattering in the present case is strong and a maximum occurs at an angle varying from 50^o to 80^o depending upon the shape.

4.7 Conclusions

In this chapter, electromagnetic radiation by an infinitely long transmission line analyzed using the dyadic Green's function technique. The transmission line carries a current of constant amplitude but varying phase and is located in the vicinity of an elliptic dielectric waveguide. Wave penetration into, and scattering by, the elliptic waveguide are investigated. The dyadic Green's functions inside and outside of the elliptic waveguide are formulated first in terms of the elliptical vector wave functions which are in turn expressed as Mathieu functions. Using the boundary conditions, we derived a set of general equations governing the scattering and transmitting coefficients of the dyadic Green's functions. From integral equations, the scattered and total electric fields in far-zone are then derived analytically and computed numerically. Different positions of the line source and various medium parameters of the elliptical cylinder are considered and corresponding results are

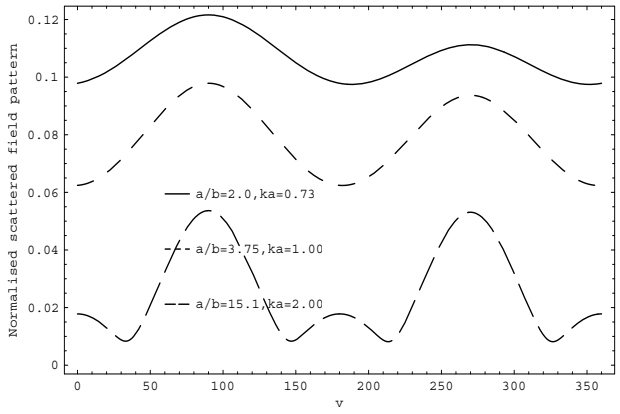

(a) Normalized scattered electric field.

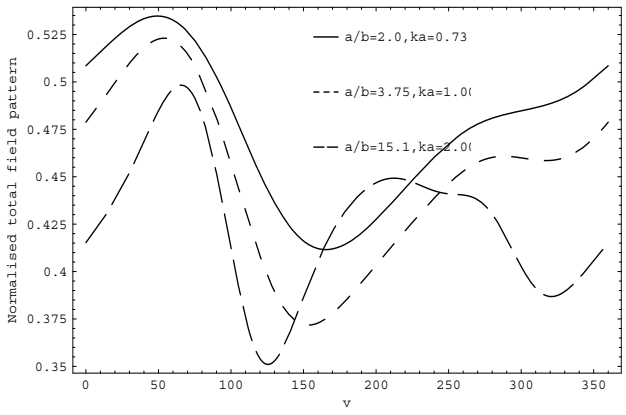

(b) Normalized total electric field.

Figure 4.7: Normalized scattered and total electric fields for $u_s = 1.2b$, $\epsilon_r = 2.0$ and $\alpha = 270^o$.

obtained and discussed.

Chapter 5

Closed-Form Eigenfrequencies in Prolate Spheroidal Conducting Cavity

---

In this chapter, an efficient approach is proposed to analyse the interior boundary value problem in a spheroidal cavity with perfectly conducting wall. Since the vector wave equations are not fully separable in spheroidal coordinates, it becomes necessary to double-check validity of the vector wave functions employed in analysis of the vector boundary problems. A closed-form solution has been obtained for the eigenfrequencies f_{ns0} based on TE and TM cases. From a series of numerical solutions for these eigenfrequencies, it is observed that the f_{ns0} varies with the parameter ξ among the spheroidal coordinates (η, ξ, ϕ) in the form of $f_{ns0}(\xi) = f_{ns}(0)[1+g^{(1)}/\xi^2+g^{(2)}/\xi^4+g^{(3)}/\xi^6+\cdots]$. By means of least squares fitting technique, the values of the coefficients, $g^{(1)}$, $g^{(2)}$, $g^{(3)}$, $\cdots$, are determined numerically. It

provides analytical results, and fast computations, of the eigenfrequencies and the results are valid if ξ is large (*e.g.*, $\xi \geq 100$).

5.1 Introduction

Calculation of eigenfrequencies in electromagnetic cavities is useful in various applications such as the design of resonators. However, analytical calculation of these eigenfrequencies is severely limited by the boundary shape of these cavities. In this chapter, the interior boundary value problem in a prolate spheroidal cavity with perfectly conducting wall is solved analytically. By applying boundary conditions, it is possible to obtain an analytical expression of the base eigenfrequencies f_{ns0} using spheroidal wave functions [56, 57, 49] regardless of whether the parameter $c = kd/2$ is small or large where k denotes the wave number while d stands for the interfocal distance.

An inspection of the plot of a series of f_{ns0} values (confirmed in [58]) indicates that variation of f_{ns0} with the coordinate parameter ξ is of the form $f_{ns0}(\xi) = f_{ns}(0)[1 + g^{(1)}/\xi^2 + g^{(2)}/\xi^4 + g^{(3)}/\xi^6 + \cdots]$ when c is small. By fitting the f_{ns0}, ξ evaluated onto an equation of its derived form, the first four expansion coefficients — $g^{(0)}$, $g^{(1)}$, $g^{(2)}$ and $g^{(3)}$ are determined numerically using the least squares method. The method used to obtain these coefficients is direct and simple, although the assumption of axial symmetry may restrict its applications to those eigenfrequencies $f_{nsm'}$, where $m' = 0$.

5.2 Spheroidal Coordinates and Spheroidal Harmonics

The prolate spheroidal coordinates shown in Fig. 5.1 are related to rectangular coordinates by the following transformation [56, 57, 49]

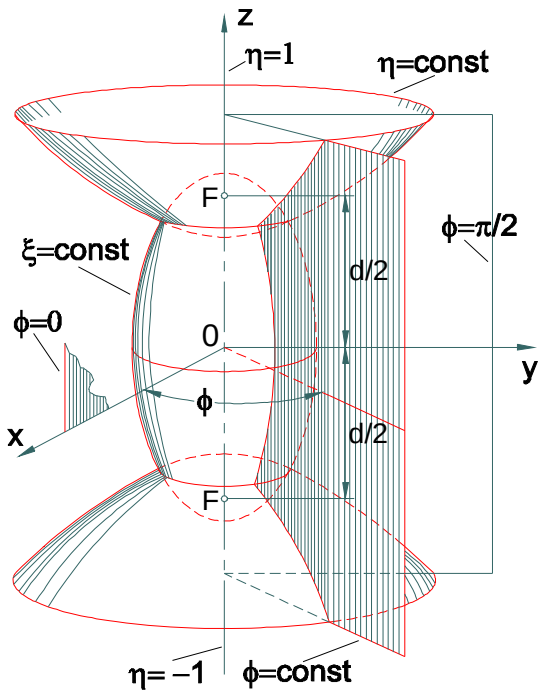

Figure 5.1: Prolate spheroidal coordinates (η, ξ, ϕ) and a conducting cavity.

$$x = \frac{d}{2}\sqrt{(1-\eta^2)(\xi^2-1)}\cos\phi, \tag{5.1a}$$

$$y = \frac{d}{2}\sqrt{(1-\eta^2)(\xi^2-1)}\sin\phi, \tag{5.1b}$$

$$z = \frac{d}{2}\eta\xi, \tag{5.1c}$$

with

$$-1 \le \eta \le 1, \quad 1 \le \xi < \infty, \quad 0 \le \phi \le 2\pi. \tag{5.1d}$$

while the oblate spheroidal coordinates are related by

$$x = \frac{d}{2}\sqrt{(1-\eta^2)\,(\xi^2+1)}\cos\phi, \tag{5.2a}$$

$$y = \frac{d}{2}\sqrt{(1-\eta^2)\,(\xi^2+1)}\sin\phi, \tag{5.2b}$$

$$z = \frac{d}{2}\eta\xi, \tag{5.2c}$$

with

$$-1 \le \eta \le 1, \;\; 0 \le \xi < \infty, \;\; 0 \le \phi \le 2\pi, \tag{5.2d}$$

or

$$0 \le \eta \le 1, \;\; -\infty < \xi < \infty, \;\; 0 \le \phi \le 2\pi. \tag{5.2e}$$

With these coordinates systems, the Helmholtz scalar wave equation becomes separable. The solutions of the wave equation are expressed in the following scalar wave functions:

$$\psi_{mn} = S_{mn}(c,\eta)R_{mn}(c,\xi)\begin{matrix}\cos\\ \sin\end{matrix} m\phi \tag{5.3a}$$

for prolate spheroidal coordinates and

$$\psi_{mn} = S_{mn}(-ic,\eta)R_{mn}(-ic,i\xi)\begin{matrix}\cos\\ \sin\end{matrix} m\phi \tag{5.3b}$$

for oblate spheroidal coordinates, respectively. The four functions, $S_{mn}(c,\eta)$, $R_{mn}(c,\xi)$, $S_{mn}(-ic,\eta)$ and $R_{mn}(-ic,i\xi)$, satisfy the following ordinary differential equations:

$$\frac{d}{d\eta}\left[(1-\eta^2)\frac{d}{d\eta}S_{mn}(c,\eta)\right] + \left[\lambda_{mn} - c^2\eta^2 - \frac{m^2}{1-\eta^2}\right]S_{mn}(c,\eta) = 0, \tag{5.4a}$$

$$\frac{d}{d\xi}\left[(\xi^2-1)\frac{d}{d\xi}R_{mn}(c,\xi)\right] - \left[\lambda_{mn} - c^2\xi^2 + \frac{m^2}{\xi^2-1}\right] R_{mn}(c,\xi) = 0; \tag{5.4b}$$

and

$$\frac{d}{d\eta}\left[(1-\eta^2)\frac{d}{d\eta}S_{mn}(-ic,\eta)\right] + \left[\lambda_{mn} + c^2\eta^2 - \frac{m^2}{1-\eta^2}\right] S_{mn}(-ic,\eta) = 0, \tag{5.5a}$$

$$\frac{d}{d\xi}\left[(\xi^2+1)\frac{d}{d\xi}R_{mn}(-ic,i\xi)\right] - \left[\lambda_{mn} - c^2\xi^2 - \frac{m^2}{\xi^2+1}\right] R_{mn}(-ic,i\xi) = 0. \tag{5.5b}$$

5.3 Theory and Formulation

5.3.1 Background Theory

The prolate spheroidal cavity under consideration is shown in Fig. 5.1. In view of the fact that Mathematica handles only vector differential operations in the prolate spheroidal coordinates in accordance with the notations used in the book by Moon and Spencer [80, pp. 28−29], a temporary change of coordinates is necessary.

As noted by Moon and Spencer [80], the vector Helmholtz equation is more complicated than the scalar counterpart, and its solution using the variable-separation principle may sometimes cause new problems. This is especially true in rotational systems like that of the spherical coordinates or spheroidal coordinates. In spheroidal

coordinates, the solution to vector boundary value problems is further complicated by the fact that the vector wave equation is not exactly separable in spheroidal coordinates. Although another more general analysis has been performed using the vector wave functions, formed by operating on the scalar spheroidal wave functions with vector operators, the validity of the results obtained is doubtful. In view of these limitations, several assumptions are made in the formulation of the current boundary problem in order to provide a truer, more accurate picture.

5.3.2 Derivation

With axial symmetry assumed, it is possible to separate the field components into E_ξ, E_η, and H_ϕ for the TM mode and H_ξ, H_η, and E_ϕ for the TE mode.

First, the TM mode is considered. With axial symmetry, H_ϕ can be assumed simply as

$$H_\phi = F(c,\xi)G(c,\eta). \tag{5.6}$$

By applying the Maxwell equations

$$\boldsymbol{\nabla} \times \boldsymbol{E} = -\frac{\partial \boldsymbol{B}}{\partial t}, \tag{5.7a}$$

$$\boldsymbol{\nabla} \times \boldsymbol{H} = \frac{\partial \boldsymbol{D}}{\partial t}, \tag{5.7b}$$

and using the formulation of $\boldsymbol{\nabla} \times \boldsymbol{X}$ in the spheroidal coordinates where

$$\boldsymbol{\nabla} \times \boldsymbol{X} = \begin{vmatrix} \widehat{\boldsymbol{\eta}}(g_\xi g_\phi)^{-1/2} & \widehat{\boldsymbol{\xi}}(g_\eta g_\phi)^{-1/2} & \widehat{\boldsymbol{\phi}}(g_\eta g_\xi)^{-1/2} \\ \dfrac{\partial}{\partial \eta} & \dfrac{\partial}{\partial \xi} & \dfrac{\partial}{\partial \phi} \\ X_\eta (g_\eta)^{1/2} & X_\xi (g_\xi)^{1/2} & X_\phi (g_\phi)^{1/2} \end{vmatrix} \tag{5.8}$$

with $\boldsymbol{X}$ being either $\boldsymbol{E}$ or $\boldsymbol{H}$, and

$$g_\eta = \frac{d^2(\xi^2 - \eta^2)}{4(1 - \eta^2)}, \tag{5.9a}$$

$$g_\xi = \frac{d^2(\xi^2 - \eta^2)}{4(\xi^2 - 1)}, \tag{5.9b}$$

$$g_\phi = \frac{d^2}{4}(1 - \eta^2)(\xi^2 - 1), \tag{5.9c}$$

the following equations can be obtained:

$$\frac{\partial^2 F(c,\xi)}{\partial \xi^2}(\xi^2 - 1) + 2\xi \frac{\partial F(c,\xi)}{\partial \xi} - \left[(c^2 + \alpha_{mn}) - c^2\xi^2 + \frac{1}{\xi^2 - 1}\right] F(c,\xi) = 0, \tag{5.10a}$$

$$\frac{\partial^2 G(c,\eta)}{\partial \eta^2}(1 - \eta^2) - 2\eta \frac{\partial G(c,\eta)}{\partial \eta} - \left[(c^2 + \alpha_{mn}) - c^2\eta^2 + \frac{1}{1 - \eta^2}\right] G(c,\eta) = 0. \tag{5.10b}$$

In the case when the semimajor axis of the spheroidal surface is close to the semiminor axis ($d/2 = \sqrt{a^2 - b^2} << 1$), the parameter c^2 ($c = kd/2$) used in the summation with α_{mn} will diminish due to the decreasing value of d^2. Thus Eqs. (5.10a) and (5.10b) will be reduced to

$$\frac{\partial^2 F(c,\xi)}{\partial \xi^2}(\xi^2 - 1) + 2\xi \frac{\partial F(c,\xi)}{\partial \xi}$$

$$- \left[\alpha_{mn} - c^2\xi^2 + \frac{1}{\xi^2 - 1}\right] F(c,\xi) = 0, \tag{5.11a}$$

$$\frac{\partial^2 G(c,\eta)}{\partial \eta^2}(1-\eta^2) - 2\eta\frac{\partial G(c,\eta)}{\partial \eta} - \left[\alpha_{mn} - c^2\eta^2 + \frac{1}{1-\eta^2}\right] G(c,\eta) = 0. \tag{5.11b}$$

Comparison of Eqs. (5.10a) and (5.10b) with Eqs. (2.8a) and (2.8b) in [49] indicates that the solutions to the differential equations are in fact given by

$$F(c,\xi) = B_n R_{1n}(c,\xi), \tag{5.12a}$$

$$G(c,\eta) = C_n S_{1n}(c,\eta) \tag{5.12b}$$

(*i.e.*, the radial and angular functions of the first kind with $m = 1$ where and subsequently the superscript $^{(1)}$ has been omitted). In the equations above, B_n and C_n are unknowns to be determined from the EM boundary conditions. Hence, the magnetic field component for the TM modes can in fact be expressed as

$$H_\phi = B_n C_n R_{1n}(c,\xi) S_{1n}(c,\eta), \tag{5.13}$$

and the electric field is therefore expressed as

$$E_\xi = \frac{A}{j\omega\epsilon\sqrt{1-\eta^2}} R_{1n}(c,\xi) \times \left[B_n C_n \sqrt{1-\eta^2}\frac{\partial S_{1n}(c,\eta)}{\partial \eta} + \frac{d}{2} S_{1n}(c,\eta)\right], \tag{5.14a}$$

$$E_\eta = \frac{A}{j\omega\epsilon} B_n C_n \frac{\partial}{\partial \xi}\left[R_{1n}(c,\xi)\sqrt{\xi^2-1}\right], \tag{5.14b}$$

where

$$A = \frac{2}{d(\xi^2-1)(1-\eta^2)} \quad .$$

To obtain the resonance condition, E_η must be zero at the surface $\xi = \xi_0$ of the perfectly conducting spheroidal cavity. From Eq. (5.14b), this requires that

$$\frac{\partial}{\partial \xi}\left[R_{1n}(c,\xi)\sqrt{\xi^2-1}\right]\Big|_{\xi=\xi_0} = 0. \tag{5.15}$$

Thus, by finding the roots of the equation above, the eigenfrequency of the TM mode can be found.

By principle of duality, the fields components for the TE mode can be obtained by substituting E_ϕ for H_ϕ, $-H_\xi$ for E_ξ, and $-H_\eta$ for E_η, respectively. Hence, the resonance condition for the TE modes can be obtained by setting $E_\phi = 0$ at $\xi = \xi_0$. From Eq. (5.13), the boundary condition requires that

$$R_{1n}(c,\xi)|_{\xi=\xi_0} = 0. \tag{5.16}$$

5.4 Numerical Results for TE Modes

5.4.1 Numerical Calculation

Using the package created in [49], the zeros of the radial function, as required by the resonance condition in Eq. (5.16) can be found in a straightforward way. This is because coding the radial function into a package offers convenience of treating $R_{mn}^{(1)}(c,\xi)$ as if it is normal function like cosine and sine. Hence, the command "FindRoot" in Mathematica can be employed to solve directly for the zeros of $R_{mn}^{(1)}(c,\xi)$. This is achieved by means of the Newton-Raphson method in the software program.

In our program, the iterations will stop when a relative error less than 10^{-6} is achieved. As in any Newton's method implementation, an initial guess is required. The spherical Bessel function zeros of various orders are assigned as the first guess. This will provide faster convergence since in the case considered, the spheroidal coordinates can actually be approximated roughly by the spherical coordinates. And from Stratton [57], the resonance condition is given by $j_n(kr) = 0$ in the spherical coordinates. Under the circumstance considered, $c\xi$ (in spheroidal coordinates) $\rightarrow$ kr (in spherical coordinated), thus the required values of $c\xi$ must be in the region around zeros of the spherical Bessel functions.

It is observed from practical calculations that in the region when $c\xi$ is large, "FindRoot" using Newton's method is capable of evaluating the zeros accurately at a very high speed. However, at the same time, it is also observed that the rate will decrease drastically in the region where $c\xi$ is small. This can be explained by the proximity of the initial guess. A series of zeros, spanning the range from $\xi = 100$ to $\xi = 1000$, were collected at irregular intervals.

From the work done by Kokkorakis and Roumeliotis [81], it can be shown, after some manipulations, that the series of values of $c\xi$ that satisfies $R_{1n}(c, \xi) = 0$, are, in fact, governed by an equation of the form

$$c(\xi)\xi = g_0\left[1 + \frac{g_1}{g_0}\left(\frac{1}{\xi^2}\right) + \frac{g_2}{g_0}\left(\frac{1}{\xi^2}\right)^2 + \frac{g_3}{g_0}\left(\frac{1}{\xi^2}\right)^3 + \cdots\right], \tag{5.17}$$

where $g_0, g_1, g_2, \ldots$ are unknown coefficients to be determined.

From Eq. (5.17), the following equation relating the eigenfrequency of the spheroidal cavity can be obtained:

$$f_{ns0} = \frac{g_0}{\pi d\xi\sqrt{\mu\epsilon}}\left[1 + \frac{g_1}{g_0}\left(\frac{1}{\xi^2}\right) + \frac{g_2}{g_0}\left(\frac{1}{\xi^2}\right)^2 + \frac{g_3}{g_0}\left(\frac{1}{\xi^2}\right)^3 + \cdots\right]. \tag{5.18}$$

Thus, by determining the coefficients, g_1, g_2, g_3, ..., a closed-form formula for the eigenfrequency of a spheroidal cavity is obtained. For a given spheroidal dimension expressed in terms of d and ξ_0, the eigenfrequency of a spheroidal cavity can be computed quickly and accurately using Eq. (5.18).

Hitherto, the coefficients have been solved only by Kokkorakis and Roumeliotis [81]. However, only the first two expansion coefficients (g_1 and g_2) of the series in (5.17) are given in his work. Moreover, except for the first coefficient g_1 which can be obtained directly, the second coefficients can only be obtained by using a relatively complicated equation. Furthermore, the equation is obtained after a very lengthy derivation that spanned over than 50 equations.

For the purpose of numerical comparison, a more direct and simpler approach for obtaining the coefficients is employed in the present work. First, the series of values of $c\xi$ that satisfy the condition $R_{1n}(c, \xi) = 0$ over the range of ξ mentioned earlier are collected and placed in a list. Then, by means of the least squares method, these values of $c\xi$ and ξ are fitted onto a function of the form given in Eq. (5.17). In this way, the parameters g_0, g_1, g_2, g_3, ..., can be determined readily. In Mathematica, this is accomplished simply by two short statement commands. To see the difference

between the analytical and numerical approaches, we plotted in Fig. 5.2 the values of $c\xi$ (vertical axis) satisfying (i) $R_{11}^{(1)}(c,\xi) = 0$ (denoted by "*Original*") and (ii) the fitted equation with g_0, g_1 and g_2 (denoted by "*Fitted*") determined against ξ (horizontal axis). A fairly good agreement is observed.

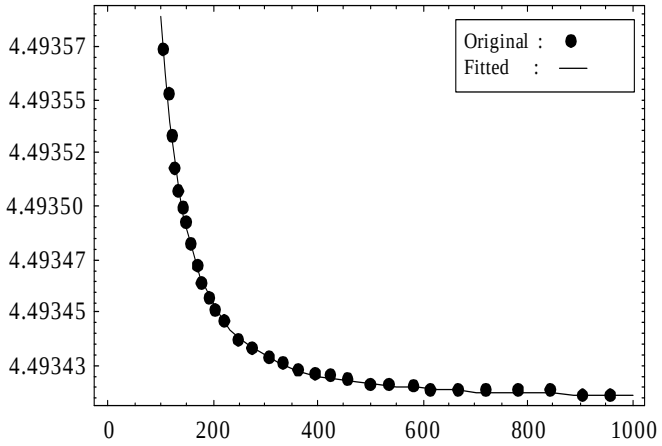

Figure 5.2: The values of $c\xi$ (vertical axis) satisfying (i) $R_{11}^{(1)}(c,\xi) = 0$ and (ii) the fitted equation with g_0, g_1 and g_2 determined against ξ (horizontal axis).

5.4.2 Results and Comparison

The values for the coefficients g_0, g_1, g_2, and g_3 for the TE modes are calculated and tabulated in Tables 5.1 and 5.2. Kokkorakis and Roumeliotis solved for the same set of coefficients in a lengthy and complicated manner. A complete but smaller table has been published in their work [81].

By comparing the present tables and Kokkorakis's tabulated results, it is observed, first, that the first two coefficients produced with this method agree with Kokkorakis's evaluations to a minimum of five significant digits. This shows the

Table 5.1: Expansion Coefficients g_0, g_1, g_2, and g_3 for TE_{ns0} Modes ($s = 1$, 2, and 3)

	n	m	$s = 1$	$s = 2$	$s = 3$
g_0	1	0	4.493410	7.725252	10.904120
	2	0	5.763460	9.095012	12.322940
	3	0	6.987932	10.417120	13.698020
	4	0	8.182562	11.704910	15.039660
g_1/g_0	1	0	0.400000	0.400000	0.400000
	2	0	0.285714	0.285714	0.285714
	3	0	0.266667	0.266667	0.266667
	4	0	0.259752	0.259752	0.259785
g_2/g_0	1	0	0.318057	0.405000	0.540398
	2	0	0.234662	0.330848	0.467022
	3	0	0.109708	0.0069634	-0.015400
	4	0	0.100111	0.057204	0.001593
g_3/g_0	1	0	0.000039	0.000049	0.000052
	2	0	0.000033	0.000041	0.000065
	3	0	0.000005	0.000001	0.000007
	4	0	0.000006	0.000008	0.000001

Table 5.2: Expansion Coefficients g_0, g_1, g_2, and g_3 for TE_{ns0} Modes ($s = 4$, 5, and 6)

	n	m	$s = 4$	$s = 5$	$s = 6$
g_0	1	0	14.066190	17.220750	20.371300
	2	0	15.5146000	18.689040	21.853870
	3	0	16.923620	20.121810	23.304250
	4	0	18.301260	21.525420	24.727570
g_1/g_0	1	0	0.400000	0.400000	0.400000
	2	0	0.285729	0.285716	0.285729
	3	0	0.266667	0.268331	0.266667
	4	0	0.259741	0.259751	0.259764
g_2/g_0	1	0	0.720727	0.945740	1.216530
	2	0	0.639935	0.848433	1.098372
	3	0	-0.051312	-0.272904	-0.258691
	4	0	-0.060967	-0.139916	-0.226860
g_3/g_0	1	0	0.000079	0.000117	0.000117
	2	0	0.000090	0.000119	0.000132
	3	0	-0.000007	-0.000010	-0.000025
	4	0	-0.000008	-0.000006	-0.000031

capability of the method to produce equally accurate results by means of a simpler way. Second, it is almost impossible to produce the coefficients g_3, g_4, and g_5 using Kokkorakis's method. The amount of analytic computation required using the method makes it impractical. On the other hand, the method presented here can be used to produce these coefficients effortlessly and almost instantly, without sacrificing any accuracy. Finally, in the paper of Kokkorakis and Roumeliotis [81], it is claimed that the coefficients are valid in the case when $\xi >> 1$. However, there is no definite definition of how small ξ must be for the coefficients to be valid. In this chapter, the valid range of ξ has been determined, numerically, to be $1/\xi < 0.01$ for $n = 1, 2$ and $1/\xi < 0.005$ for $n = 3, 4$. For other higher-order n, the valid range of ξ will have to be reduced further.

5.5 Numerical Results for TM Modes

5.5.1 Numerical Calculation

Closed-form solutions of the eigenfrequencies for TM modes are obtained in a similar fashion. The variation of $c\xi$ with ξ bears an identical form to the Eq. (5.18); that is, the eigenfrequency for the TM modes can be expressed in a form identical to those shown in (5.18) except that now, g_0 has to be changed to satisfy the equation

$$j_s^d(g_0) = \left.\frac{d[xj_s(x)]}{dx}\right|_{x=g_0} = 0, \tag{5.19}$$

where $j_s(x)$ represents the spherical Bessel functions.

By comparison with the TE modes, two differences need to be considered in the programming aspect. First, the resonance condition has to be altered. Previously, for the TE modes, the condition stated in Eq. (5.16) is satisfied. In the TM modes, the boundary condition requires that Eq. (5.15) be satisfied. At the surface $\xi = \xi_0$, the boundary condition becomes

$$\frac{\partial}{\partial \xi}\left(R_{1n}(c,\xi)\sqrt{\xi^2-1}\right)\Big|_{\xi=\xi_0} = 0. \tag{5.20}$$

With the new boundary condition, the zeros of the left-hand term of (5.15) have to be found instead of that of the radial function. In the program, the zeros of the radial derivative expression in Eq. (5.15) are evaluated using the same Newton's method. However, the function is now different, and so is the initial guess. For the TE modes, the various orders of zeros of the functions in Eq. (5.19) are used instead. To see the difference between the analytical and numerical approaches, we plotted in Fig. 5.3 the values of $c\xi$ (vertical axis) satisfying (i) $\partial/(\partial\xi)(R_{11}^{(1)}(c,\xi)\ \sqrt{\xi^2-1}) = 0$ (denoted by "Original") and (ii) the fitted equation with g_0, g_1 and g_2 (denoted by "Fitted") determined against ξ (horizontal axis). A fairly good agreement is also observed.

5.5.2 Results and Comparison

Employing the same technique to determine the expansion coefficients g_1, g_2, g_3, ..., a series of $c\xi$ values that forces the function in Eq. (5.15) to approach zero is collected and fitted into an equation of the form in Eq. (5.18). In this way, the various

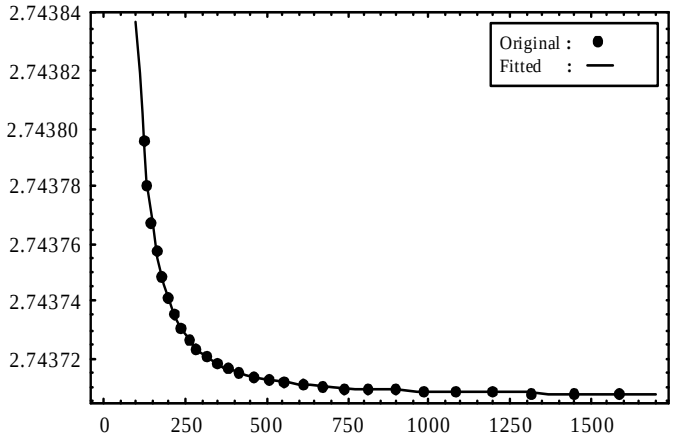

Figure 5.3: The values of $c\xi$ (vertical axis) satisfying (i) $\partial/(\partial\xi)(R_{11}^{(1)}(c,\xi)\sqrt{\xi^2-1}) = 0$ and (ii) the fitted equation with g_0, g_1 and g_2 determined against ξ (horizontal axis).

expansion coefficients are determined. Tabulations of various values obtained using this method for the TM modes are made and shown in Tables 5.3 and 5.4.

The same observation and the same conclusion as in [81] can be drawn upon comparing of the two tables for the TM modes with those for the TE modes. Hence, they are not repeated here.

5.6 Conclusion and Discussion

In this chapter, one of the many possible applications of the spheroidal wave function package is presented in detail, solving an interior boundary value problem. The convenience of coding in Mathematica package is manifested by the ability of this program to find the zeros of functions with complex argument (such as radial functions) simply with one statement. This problem, by itself, is a highly interesting

Table 5.3: Expansion Coefficients g_0, g_1, g_2, and g_3 for TM_{ns0} Modes ($s = 1$, 2, and 3)

	n	m	$s = 1$	$s = 2$	$s = 3$
g_0	1	0	2.743707	6.116764	9.316616
	2	0	3.870239	7.443087	10.713010
	3	0	4.973420	8.721750	12.063590
	4	0	6.061949	9.967547	13.380120
g_1/g_0	1	0	0.472361	0.411295	0.404717
	2	0	0.317536	0.291498	0.288341
	3	0	0.287607	0.270829	0.268664
	4	0	0.275250	0.263014	0.261515
g_2/g_0	1	0	0.341865	0.365769	0.473216
	2	0	0.241764	0.287367	0.398629
	3	0	0.146803	0.094815	0.045170
	4	0	0.127803	0.078719	0.002503
g_3/g_0	1	0	0.000047	0.000050	0.000064
	2	0	0.000007	0.000039	0.000054
	3	0	0.000005	0.000003	0.000001
	4	0	0.000017	0.000011	0.000001

Table 5.4: Expansion Coefficients g_0, g_1, g_2, and g_3 for TM_{ns0} Modes ($s = 4$, 5, and 6)

	n	m	$s = 4$	$s = 5$	$s = 6$
g_0	1	0	12.485940	15.643870	18.796250
	2	0	13.920520	17.102740	20.272000
	3	0	15.313560	18.524210	21.713930
	4	0	16.674150	19.915400	23.127780
g_1/g_0	1	0	0.402599	0.401648	0.401139
	2	0	0.287621	0.286712	0.286420
	3	0	0.267865	0.267472	0.267247
	4	0	0.260747	0.260430	0.260245
g_2/g_0	1	0	0.629327	0.831403	1.078787
	2	0	0.498710	0.741883	0.971928
	3	0	-0.015979	-0.090035	-0.177032
	4	0	-0.029849	-0.100678	-0.183054
g_3/g_0	1	0	0.000086	0.000113	0.000147
	2	0	0.000033	0.000008	0.000076
	3	0	0.000002	-0.000012	-0.000024
	4	0	-0.000003	-0.000014	-0.000025

topic. Due to the preoccupation with the more important issue of completing the Mathematica package, the axial symmetry is assumed so as to reduce the complexity of the problems. The more general and practical problem in which the assumption of axial symmetry is removed is a topic worth looking into for future investigations. As indicated in [49], the study of oblate spheroidal cavities can be achieved in a similar way or by symbolic transfer between the oblate and prolate coordinates. However, it should be noted that the assumed axial symmetry is kept in the z-direction and the assumed field components are not changed in the symbolic programming. s

Chapter 6

A New Closed Form Solution to Light Scattering by Spherical Nanoshells

---

Light or electromagnetic wave scattered by a single sphere or a coated sphere has been considered as a classic Mie theory. There have been some further extensions which were made further based on the Mie theory. Recently, a closed form analytical model of the scattering cross section of a single nanoshell has been considered. The present chapter is documented further, based on the work in 2006 by Alam and Massoud, to derive another different closed form solution to the problem of light scattered by the nanoshells using polynomials of up to order 6. Validation is made by comparing the present closed form solution to the exact Mie scattering solution and also to the other closed form solution by Alam and Massoud. The present work is found to be, however, more generalized and also more accurate for the coated spheres of either tiny/small or medium sizes than that of Alam and Massoud. Therefore, the derived formulas can be used for accurately characterizing both surface plasmon

resonances of nanoparticles (of small sizes) or nano antenna near-field properties (of medium sizes comparable with half wavelength).

6.1 Introduction

Light scattering by spherical particles has been a classical subject which attracted lots of interests over the past a few decades and was also formulated rigorously using the Mie theory [82]. Calculations of derivatives of Mie scattering coefficients were clearly shown in [83]. As the electrical parameter/size $k_0 a$ (where k_0 denotes the wave number of the free space and a stands for the radius of the sphere) of a scattering object becomes much smaller than 1, the Rayleigh scattering dominates [84, 85] and it is expressed approximately by the first order expression in Mie scattering theory.

Using the same method for matching boundary conditions, the results of electric and magnetic fields scattered by multilayered spherical structures can be easily extended [86–90]. Scattering of electromagnetic waves from two concentric spheres was first worked out by Aden and Kerker [86]. Scattering by multilayered spheres was well studied [87, 88] both in the near field and the far field. Scattering of an inhomogeneous sphere was also considered [89] where the sphere is discretized into a multilayered sphere of different permittivities along the radial direction. In addition, a sphere placed in a unbounded medium is also considered in [90] where how the incident plane wave is formulated and considered in the classical Mie scattering

field theory was also addressed in detail. A number of applications was reported by Kerker in [91].

Electromagnetic radiation problem associated with a multilayered sphere was also considered [92, 93]. The dyadic Green's functions used to define electric and magnetic fields in spherically multilayered media were derived [92], which helps to formulate the dipole or antenna radiation problem easily and straightforwardly. Applications of the electromagnetic radiation due to a loop antenna in the presence of a sphere was also considered [93] which could be applied to the medical radiation treatment to human head.

Light or electromagnetic scattering by composite spheres is another interest in the scientific and engineering communities [27–34]. Electromagnetic scattering by a plasma anisotropic sphere was analyzed [27]. The analysis was extended to Mie scattering by an uniaxial anisotropic sphere [28]. Furthermore, scattering by an inhomogeneous plasma anisotropic sphere of multilayers was also formulated and investigated [29]. It can be easily extended to light scattering by an inhomogeneous plasma anisotropic sphere where the exact solutions could be applied to obtain the field distributions in the multilayered spherical structures. Along the analysis line of [27–29], the standard eigenfucntion expansion technique is utilized and the theory for the anisotropic media can still follow closely to theory used for the isotropic media. To characterize eigenvalues in the anisotropic media different from those in the isotropic media, potential formulation and parametric studies for scattering by rotationally symmetric anisotropic spheres were also carried out recently [30].

In addition, Sun discussed light scattering by coated sphere immersed in absorbing medium and compared FDTD method with analytic solutions [31]. Scatterers consisting of concentric and nonconcentric multilayered spheres were also considered [32]. An improved algorithm for electromagnetic scattering of plane wave and shaped beams by multilayered spheres was developed [33] and the geometrical-optics approximation of forward scattering by coated particles was then discussed [34].

With new developments of nanoscience and nanotechnology, it becomes desirable to investigate the microcosmic world of the scattering problems. Nano-scaled objects have thus attracted considerable attentions recently, primarily because they have shown some interesting optical properties and are found to be important for modern photonic applications [35–38]. Nano-scaled metallic particles exhibit interesting optical characteristics and behave differently from those of normal-scaled dimensions. Interactions of collective and individual particles of metals (such as copper, silver and gold) were studied long time ago [39, 40]. Johnson and Christy plotted both the real and imaginary parts of relative permittivities of copper, silver and gold nanoparticles as a function of photon energy in a large range according to different frequencies [41].

Recently, a closed form analytial model of the scattering cross section of a single spherical nanoshell has been considered [59], while some fine experimental works were conducted in [60, 61]. The results given in [59] seemed to agree with the exact solutions very well in accordance with the results in Figs. 6.2 and 6.3. Our recent careful investigations realize that the relative errors in their results are not so small,

especially when the electric size of the nano shell is not large. The present paper is therefore to derive another different closed form solution for describing the light wave scattered by the nanoshells using a polynomial of up to order 6. Validation will be made by comparing the present closed form solution to the exact Mie scattering solution and also to the other closed form solution by Alam and Massoud.

6.2 Basic Formulas

The geometry of the problem defined in this paper is shown in Fig. 6.1, where we will follow closely with the definitions in [59]. So the out-most to inner-most regions

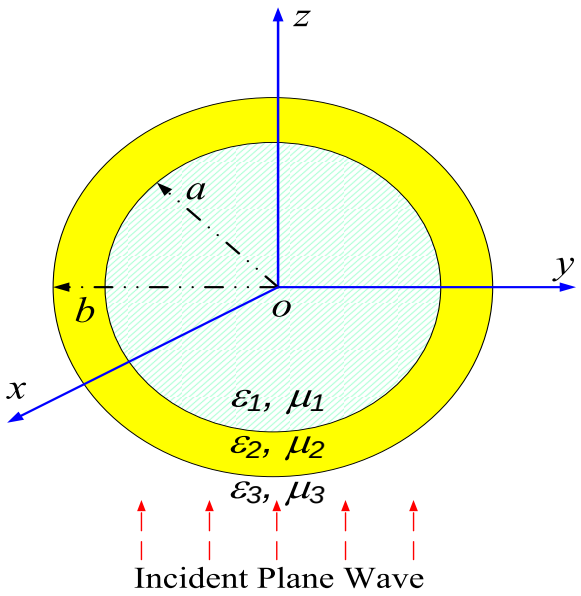

Figure 6.1: Geometry of light scattering by a spherical nanoshell in hosting medium.

are denoted as Regions $i = 3$, 2 and 1 whose permittivities and permeabilities are

assumed to ϵ_i and $\mu_i = \mu_0$ (as nonmagnetic materials), respectively. The incident plane wave is propagating along $+z$ direction. The inner radius of the coated sphere is a and outer radius is b; in other words, the spherical geometrical thickness of the nanoshell is $c = b - a$. For convenience of the formulation, we take $x = k_0 a = \omega\sqrt{\epsilon_0\mu_0}a = a\omega/c$ and $y = k_0 b = \omega\sqrt{\epsilon_0\mu_0}b = b\omega/c$ to be the electrical parameters for the inner and outer radii of the spherical nanoshell (where c denotes the speed of light in free space)[1]. In addition, the refractive indices of the spherical nanocore and the nanoshell are denoted by $m_1 = \sqrt{\epsilon_1/\epsilon_0}$ and $m_2 = \sqrt{\epsilon_2/\epsilon_0}$, respectively. The refractive index of the background hosting medium is $m_3 = \sqrt{\epsilon_3/\epsilon_0}$ and it is assumed herein that it is not necessarily unity, but it can be simplified as $m_3 = 1$ for free space. Correspondingly, the wave numbers in the regions are denoted by $k_j = \omega\sqrt{\epsilon_j\mu_0}$ where $j = 1$, 2 and 3 for the inner, the intermediate, and the outer regions of the problem geometry.

Electric field of an electromagnetic plane wave with an amplitude of E_0 in unbounded hosting medium can be written in terms of the spherical vector wave functions $\boldsymbol{M}$ (TE-wave) and $\boldsymbol{N}$ (TM-wave) as follows:

$$\boldsymbol{E}_i = \sum_{n=1}^{\infty} i^n \frac{2n+1}{n(n+1)} \left(\boldsymbol{M}_{o1n}^{(1)} - i\boldsymbol{N}_{e1n}^{(1)} \right), \tag{6.1}$$

where an incident wave amplitude E_0 is assumed to be unity for simplification of the formulation. This assumption will not affect the further discussion and results. When it is scattered by the nanoshell, the electric wave outside of the nanoshell in the hosting medium is written in terms of the outgoing TE and TM waves in the

[1]The definition made in Ref. [59] is not precisely correct unless the hosting or background medium is free space. Details of the proof will be given later.

following similar form

$$\boldsymbol{E}_{\text{scat},3} = \sum_{n=1}^{\infty} i^n \frac{2n+1}{n(n+1)} \left(a_n \boldsymbol{M}_{o1n}^{(3)}(k_3 r) - i b_n \boldsymbol{N}_{e1n}^{(3)}(k_3 r) \right) \tag{6.2a}$$

while the field inside the nanoshell is expressed by

$$\begin{aligned} \boldsymbol{E}_{\text{scat},2} = \sum_{n=1}^{\infty} i^n \frac{2n+1}{n(n+1)} \Big[& \left(a_n' \boldsymbol{M}_{o1n}^{(3)}(k_2 r) + c_n' \boldsymbol{M}_{o1n}^{(1)}(k_2 r) \right) \\ & -i \left(b_n' \boldsymbol{N}_{e1n}^{(3)} + d_n' \boldsymbol{N}_{e1n}^{(1)} \right) \Big]; \end{aligned} \tag{6.2b}$$

and the electric field inside the nanospherical core-region is given due to the TE and TM standing waves by

$$\boldsymbol{E}_{\text{scat},1} = \sum_{n=1}^{\infty} i^n \frac{2n+1}{n(n+1)} \left(c_n \boldsymbol{M}_{o1n}^{(1)}(k_1 r) - i d_n \boldsymbol{N}_{e1n}^{(1)}(k_1 r) \right). \tag{6.2c}$$

In the aforegiven field expressions where the eigenvalue $m = 1$, the spherical vector wave functions $\boldsymbol{M}_{emn}^{(i)}$ and $\boldsymbol{M}_{omn}^{(i)}$ for even and odd TE modes and $\boldsymbol{N}_{emn}^{(i)}$ and $\boldsymbol{N}_{omn}^{(i)}$ for even and odd TM modes are defined for $i = 1$, 2, 3 and 4 as

$$\begin{aligned} \boldsymbol{M}_{emn}^{(i)}(kr) = & -z_n^{(i)}(\rho) \frac{m P_n^m(\cos\theta)}{\sin\theta} \sin m\phi \widehat{\boldsymbol{\theta}} \\ & - z_n^{(i)}(\rho) \frac{dP_n^m(\cos\theta)}{d\theta} \cos m\phi \widehat{\boldsymbol{\phi}}, \end{aligned} \tag{6.3a}$$

$$\begin{aligned} \boldsymbol{M}_{omn}^{(i)}(kr) = & z_n^{(i)}(\rho) \frac{m P_n^m(\cos\theta)}{\sin\theta} \cos m\phi \widehat{\boldsymbol{\theta}} \\ & - z_n^{(i)}(\rho) \frac{dP_n^m(\cos\theta)}{d\theta} \sin m\phi \widehat{\boldsymbol{\phi}}, \end{aligned} \tag{6.3b}$$

$$\begin{aligned} \boldsymbol{N}_{emn}^{(i)}(kr) = & \frac{n(n+1) z_n^{(i)}(\rho)}{\rho} P_n^m(\cos\theta) \cos m\phi \widehat{\boldsymbol{r}} \\ & + \frac{d}{\rho d\rho} \left[\rho z_n^{(i)}(\rho) \right] \left[\frac{dP_n^m(\cos\theta)}{d\theta} \cos m\phi \widehat{\boldsymbol{\theta}} \right. \\ & \left. - \frac{m P_n^m(\cos\theta)}{\sin\theta} \sin m\phi \widehat{\boldsymbol{\phi}} \right], \end{aligned} \tag{6.3c}$$

$$\begin{aligned} \boldsymbol{N}_{omn}^{(i)}(kr) = & \frac{n(n+1) z_n^{(i)}(\rho)}{\rho} P_n^m(\cos\theta) \sin m\phi \widehat{\boldsymbol{r}} \\ & + \frac{d}{\rho d\rho} \left[\rho z_n^{(i)}(\rho) \right] \left[\frac{dP_n^m(\cos\theta)}{d\theta} \sin m\phi \widehat{\boldsymbol{\theta}} \right. \end{aligned}$$

$$+\frac{mP_n^m(\cos\theta)}{\sin\theta}\cos m\phi\widehat{\boldsymbol{\phi}}\Bigg]. \tag{6.3d}$$

In the above definitions, the superscripts (1), (2), (3) and (4) of $z_n^{(i)}(\rho)$ (where $\rho = kr$ denotes the argument of the spherical Bessel functions) refer to the first kind of spherical Bessel function, the second kind of spherical Bessel function, the first kind of spherical Hankel function, and the second kind of spherical Hankel function, respectively.

Apparently, there exist 8 sets of unknown parameters, (a_n, b_n, c_n and d_n) and also (a'_n, b'_n, c'_n and d'_n), to be determined. From continuity relations of electric field and magnetic field tangential components, we will have 4 boundary conditions on the inner spherical interface and the other 4 boundary conditions on the outer spherical interface. So, all the unknown coefficients can be determined uniquely. The solution procedure is rather standard, although lengthy. So, we will not provide the details of all the solutions, instead we will provide the obtained scattering coefficients in the hosting medium only, a_n and b_n. They are given by

$$a_n = \frac{a_n^{\text{num}}}{a_n^{\text{den}}}, \quad \text{and} \quad b_n = \frac{b_n^{\text{num}}}{a_n^{\text{den}}}, \tag{6.4}$$

where the numerators $N_n^{a,b}$ and denominators $D_n^{a,b}$ of the two scattering coefficients are explicitly given below:

$$\begin{aligned} a_n^{\text{num}} = {} & m_3\psi_n(m_3y)\left[\psi'_n(m_2y) - A_n\chi'_n(m_2y)\right] \\ & - m_2\psi'_n(m_3y)\left[\psi_n(m_2y) - A_n\chi_n(m_2y)\right], \end{aligned} \tag{6.5a}$$

$$\begin{aligned} a_n^{\text{den}} = {} & m_3\xi_n(m_3y)\left[\psi'_n(m_2y) - A_n\chi'_n(m_2y)\right] \\ & - m_2\xi'_n(m_3y)\left[\psi_n(m_2y) - A_n\chi_n(m_2y)\right], \end{aligned} \tag{6.5b}$$

$$b_n^{\text{num}} = m_2\psi_n(m_3y)\left[\psi_n'(m_2y) - B_n\chi_n'(m_2y)\right] - m_3\psi_n'(m_3y)\left[\psi_n(m_2y) - B_n\chi_n(m_2y)\right], \tag{6.5c}$$

$$a_n^{\text{den}} = m_2\xi_n(m_3y)\left[\psi_n'(m_2y) - B_n\chi_n'(m_2y)\right] - m_3\xi_n'(m_3y)\left[\psi_n(m_2y) - B_n\chi_n(m_2y)\right], \tag{6.5d}$$

with the intermediate parameters A_n and B_n defined[2] as

$$A_n = \frac{m_2\psi_n(m_2x)\psi_n'(m_1x) - m_1\psi_n'(m_2x)\psi_n(m_1x)}{m_2\chi_n(m_2x)\psi_n'(m_1x) - m_1\chi_n'(m_2x)\psi_n(m_1x)}, \tag{6.6a}$$

$$B_n = \frac{m_2\psi_n(m_1x)\psi_n'(m_2x) - m_1\psi_n'(m_1x)\psi_n(m_2x)}{m_2\chi_n'(m_2x)\psi_n(m_1x) - m_1\chi_n(m_2x)\psi_n'(m_1x)}; \tag{6.6b}$$

and the Reccati-Bessel functions were defined[3] as

$$\psi_n(\rho) = \rho j_n(\rho), \tag{6.7a}$$

$$\chi_n(\rho) = \rho y_n(\rho), \tag{6.7b}$$

$$\xi_n(\rho) = \rho h_n^{(1)}(\rho) = \rho\left[j_n(\rho) + iy_n(\rho)\right], \tag{6.7c}$$

with the prime to denote their first order derivative of the Reccati-Bessel functions. For the nonmagnetic medium, we have the free space permeability for all the regions, i.e., $\mu_1 = \mu_2 = \mu_3 = \mu_0$. Again, ϵ_1 and ϵ_2 denote the permittivities of the spherical nanocore and the nanoshell while ϵ_3 stands for the permittivity in the outer region of the structure. The formulas given in (6.5a)-(6.5d) are slightly different from those forms in [59], because we herein enclose m_3 in the formulation without loss of any generality while the formulas in (1) and (2) of [59] is only applicable to the case where the outer region is free space; but in the later applications in [59], the authors assumed $\epsilon_3 = 1.78\epsilon_0$ which does not make sense.

[2] In Eqs. (12) and (13) of Ref. [59], subscripts of some $\psi_n(\rho)$ and its derivative were missing.

[3] In Ref. [59], $\chi_n(\rho)$ was not generally defined.

6.3 New Closed Form Solution to Intermediate Coefficients A_n and B_n

As the scattering coefficients a_n and b_n are of our specific interests here, although they look very complicated and involved with the spherical Bessel functions of various kinds. To do so, we also follow the similar procedure of approximating the scattering coefficients a_n and b_n by taking the series expansions of the following first and second kinds of spherical Bessel functions as:

$$j_n(z) = \frac{z^n}{(2n+1)!!} \times \left[1 - \frac{z^2/2}{1!(2n+3)} + \frac{(z^2/2)^2}{2!(2n+3)(2n+5)} + \cdots\right], \tag{6.8a}$$

$$y_n(z) = \frac{(2n-1)!!}{z^{n+1}} \times \left[1 - \frac{z^2/2}{1!(1-2n)} + \frac{(z^2/2)^2}{2!(1-2n)(3-2n)} + \cdots\right], \tag{6.8b}$$

where and subsequently, $n!!$ denotes the factorial by a step of 2 (for instance, $7!! = 7 \cdot 5 \cdot 3 \cdot 1$ while $8!! = 8 \cdot 6 \cdot 4 \cdot 2$). It should be noted that the approximations taken by Alam and Massoud seemed to be incorrect. The numerical tests show that when $x = 0.6$ and $n = \{1, 2, 3\}$, we will have the following exact values of $j_n(z) = \{0.192892, 0.023389, 0.00201634\}$. If we use the approximation in [59], the following values are obtained: $j_n(z) = \{0.149956, 0.0196055, 0.00175972\}$; but if we use the approximations in (6.8a) and (6.8b) of this paper where only the explicit first 3 terms are included, we will obtain fairly accurate results of $j_n(z) = \{0.192893, 0.023389, 0.00201634\}$. Similarly, for the same given conditions ($x = 0.6$ and $n = \{1, 2, 3\}$), we have the exact values of $y_n(z) = \{3.23367, 14.7928, 120.04\}$, the approximate

values of $y_n(z) = \{3.95662,\ 24.7842,\ 155.333\}$ by Ref. [59], and the approximate values of $y_n(z) = \{3.23278,\ 14.7972,\ 120.032\}$ by this paper.

6.3.1 Approximate Expression of Coefficient A_n

With the confidence built, we are now moving toward deriving the closed form solution for the coefficient A_n as follows:

$$A_n \approx \frac{A_n^{\text{num}}}{A_n^{\text{den}}}, \tag{6.9}$$

where we have the closed form solutions to the numerator A_n^{num} and denominator A_n^{den}:

$$\begin{aligned} A_n^{\text{num}} = & -(2n-5)(2n-3)(2n-1)\pi x^{2n+1} m_2^{2n+1} \left(m_2^2 \right. \\ & \left. -m_1^2\right) \left\{x^4 \left(4n^3+24n^2+41n-2x^2m_2^2+21\right) m_1^4 \right. \\ & -2x^2 \left[x^4 m_2^4 - \left(4n^3+28n^2+67n+63\right) x^2 m_2^2 \right. \\ & \left. +2\left(8n^4+68n^3+202n^2+247n+105\right)\right] m_1^2 \\ & +\left(4n^3+24n^2+41n+21\right) \left[x^4 m_2^4 - 4(2n+5) \right. \\ & \left. \times x^2 m_2^2 + 8\left(4n^2+16n+15\right)\right]\Big\}, \end{aligned} \tag{6.10a}$$

$$\begin{aligned} A_n^{\text{den}} = & 4^n \left(4n^2+8n+3\right) \Gamma^2\left(n+\frac{1}{2}\right) \left\{\left(4n^2+24n \right.\right. \\ & \left. +35\right) x^4 \left[4n^3-19n+(1-2n)x^2m_1^2-15\right] m_2^6 \\ & +\left(4n^2+4n-35\right) x^2 \left[2(2n+1)x^4 m_1^4 - \left(4n^3 \right.\right. \\ & \left. +32n^2+43n-30\right) x^2 m_1^2 + 4\left(8n^4+28n^3+2n^2 \right. \\ & \left. -63n-45\right)] m_2^4 + \left(4n^2-16n+15\right) [-(2n+3) \end{aligned} \tag{6.10b}$$

$$\times x^6 m_1^6 + \left(-4n^3 + 79n + 105\right) x^4 m_1^4 - 12\left(8n^3 + 52n^2 + 94n + 35\right) x^2 m_1^2 + 8\left(16n^5 + 128n^4 + 336n^3 + 292n^2 - 37n - 105\right)\Big] m_2^2 + n\left(16n^4 - 16n^3 - 160n^2 + 292n - 105\right) m_1^2 \Big[x^4 m_1^4 - 4(2n + 5) x^2 m_1^2 + 8\left(4n^2 + 16n + 15\right)\Big]\Big\}. \tag{6.10b}$$

It is noted that a factor of

$$F_n^A = \frac{m_1^n \left(32n^5 + 48n^4 - 400n^3 - 216n^2 + 1250n - 525\right)^{-1}}{128 \times 2^{2n} \times m_2^{n+1} \times \Gamma^2\left(n + \frac{5}{2}\right)} \tag{6.11}$$

has been involved in both the numerator and the denominator of coefficient A_n in (6.6a) and has been canceled in (6.9).

It is seen that the solution derived here is general enough for all the different values of n and x values, more complete in form than that given in [59]. Also, it is seen that the closed form solution is very simple, given in terms of only some simple additions of algebraic functions. Also, it is to be shown later that they are quite accurate; and it is valid for complex argument x as well. For those who use Fortran or C languages to write their own codes for computations, this has made the code implementation extremely easier and faster.

Specifically, need to generate the solution for the first a few orders. Firstly, we have the case of $n = 1$, and easily we have the following simplified solution:

$$A_1^{\text{num}} = 27\pi x^3 m_2^3 \left(m_1^2 - m_2^2\right)\Big[2800 - 280\left(m_1^2 + m_2^2\right) x^2 + \left(10m_1^4 + 36m_2^2 m_1^2 + 10m_2^4\right) x^4\Big], \tag{6.12a}$$

$$A_1^{\text{den}} = \frac{15\pi}{4}\left[30240\left(m_1^2+2m_2^2\right)-3024\left(m_1^2-m_2^2\right)\left(m_1^2\right.\right.$$
$$\left.+10m_2^2\right)x^2+4\left(27m_1^6+540m_2^2m_1^4+1323m_2^4m_1^2\right.$$
$$\left.-1890m_2^6\right)x^4+4\left(-15m_2^2m_1^6-162m_2^4m_1^4\right.$$
$$\left.\left.-63m_2^6m_1^2\right)x^6\right]; \tag{6.12b}$$

and when $n = 2$:

$$A_2^{\text{num}} = -33\pi x^5 m_2^5\left(m_1^2-m_2^2\right)\left[10584-756\left(m_1^2+m_2^2\right)\right.$$
$$\left.\times\, x^2+\left(21m_1^4+62m_2^2m_1^2+21m_2^4\right)x^4\right], \tag{6.13a}$$
$$A_2^{\text{den}} = \frac{315\pi}{16}\left[-266112\left(2m_1^2+3m_2^2\right)+6336\left(m_1^2-m_2^2\right)\right.$$
$$\left(6m_1^2+21m_2^2\right)x^2+16\left(-66m_1^6-231m_2^2m_1^4\right.$$
$$\left.+2376m_2^4m_1^2-2079m_2^6\right)x^4+16\left(7m_2^2m_1^6\right.$$
$$\left.\left.-110m_2^4m_1^4-297m_2^6m_1^2\right)x^6\right]. \tag{6.13b}$$

6.3.2 Approximate Expression of Coefficient B_n

Similarly, the closed form solution for the coefficient B_n is given by

$$B_n \approx \frac{B_n^{\text{num}}}{B_n^{\text{den}}}, \tag{6.14}$$

where we have the closed form solutions to the numerator B_n^{num} and denominator B_n^{den}:

$$B_n^{\text{num}} = \left(128n^7+448n^6-1120n^5-3920n^4+2072n^3\right.$$
$$\left.+7252n^2-450n-1575\right)\pi x^{2n+3}m_2^{2n+1}\left(m_1^2\right.$$

$$
\begin{aligned}
&-m_2^2\Big)\Big\{(2n+3)x^4m_1^4+2x^2\Big[(2n+5)x^2m_2^2\\
&-4\Big(4n^2+20n+21\Big)\Big]m_1^2+(2n+3)\Big[x^4m_2^4\\
&-8(2n+7)x^2m_2^2+16\Big(4n^2+24n+35\Big)\Big]\Big\}, \qquad (6.15a)\\
B_n^{\text{den}} &= 4^n(2n+1)^2(2n+3)^2\Big(4n^2+24n+35\Big)\\
&\times\Gamma^2\left(n+\frac{1}{2}\right)\Big\{-\Big(8n^3-36n^2+46n-15\Big)\\
&\times x^6m_1^6+\Big(8n^3-4n^2-82n+105\Big)x^4\Big(8n^2\\
&+16n+x^2m_2^2-10\Big)m_1^4-\Big(8n^3+28n^2-50n\\
&-175\Big)x^2\Big[-x^4m_2^4+4\Big(4n^2-4n-3\Big)x^2m_2^2\\
&+8\Big(8n^3-4n^2-18n+9\Big)\Big]m_1^2+\Big(8n^3+60n^2\\
&+142n+105\Big)\Big[-x^6m_2^6+2\Big(4n^2-16n+15\Big)\\
&\times x^4m_2^4+8\Big(8n^3-36n^2+46n-15\Big)x^2m_2^2\\
&+16\Big(16n^4-64n^3+56n^2+16n-15\Big)\Big]\Big\}. \qquad (6.15b)
\end{aligned}
$$

Similarly, it is also noted that a factor of

$$
F_n^B=\frac{2^{-2(n+6)}m_1^{n+1}m_2^{-n}}{(2n-5)(2n-3)(2n-1)(2n+1)(2n+3)\Gamma^2\left(n+\frac{9}{2}\right)} \qquad (6.16)
$$

has been involved in both the numerator and the denominator of coefficient B_n in (6.6b) and has been canceled in (6.14).

To make it applicable and specific in solution, we consider the solution to the coefficient B_1 below. Again, we split its expression into the numerator and denominator and they are respectively given as follows:

$$
B_1^{\text{num}}=-x^5m_2^3\Big(m_1^2-m_2^2\Big)\Big\{\Big[5x^2m_1^4+2\Big(7x^2m_2^2-180\Big)
$$

$$\times m_1^2 + 5m_2^2\left(x^2m_2^2 - 72\right)\Big]x^2 + 5040\Big\}, \tag{6.17a}$$

$$B_1^{\text{den}} = 15\Big[x^6m_1^6 - 9x^4\left(x^2m_2^2 + 14\right)m_1^4 + 63x^2\left(x^4m_2^4 + 12x^2m_2^2 + 40\right)m_1^2 + 105\left(x^6m_2^6 - 6x^4m_2^4 - 24x^2m_2^2 - 144\right)\Big]. \tag{6.17b}$$

The above fractional form suggests that the solution to the coefficient B_1 is not as simple as the expression of the linear function of x^5 given in [59]. To gain more insight into the accuracy of the expressions, we will discuss on the details of comparisons among the three sets of data, the exact solution from Mie theory, the closed form solution in [59], and the new closed form solution in this paper.

6.3.3 Validations and Accuracy

To gain insight into the accuracy of the present closed form solution to the coefficients A_n and B_n, we have considered relative errors of the numerical results obtained using the present closed form solution as compared with the exact results obtained directly from the Mie scattering theory. In addition, we have also considered the relative errors of the previously obtained closed form solution results in [59]. To gain the consistent results, we also assume the same parameters as used in [59], where $\epsilon_1 = (5.44/1.78)\epsilon_0$, $\epsilon_3 = \epsilon_0$, and $\epsilon_2 = (\epsilon_1 + \epsilon_3)/2$. A comparison has been shown in Fig. 6.2(a) for the coefficient A_1, in Fig. 6.2(b) for the coefficient A_2, and in Fig. 6.2(c) for the coefficient B_1. It is clearly shown that the present results of closed form solution to these coefficients are far more accurate than those in [59] where the relative error of A_1 is always larger than 25% and can reach 30%;

the relative error of A_2 increase up to 25% at a speed faster than cubic power; and the relative error of B_1 also increases from 17% to 35%. All of these accuracies are neither scientifically nor engineeringly acceptable.

6.4 New Closed Form Solutions to Scattering Coefficients a_n and b_n

Now, we turn to the approximations finally to the scattering coefficients a_n and b_n. Substituting (6.8a) and (6.8b) into (6.7a) and (6.7b) and further into (6.7c), we could approximate (6.5a) and (6.5b) as follows.

6.4.1 Approximate Expression of Coefficient a_n

Generalized Case for Any n and Arbitrary Material Properties

Without loss of any generality, we would keep all the intermediates inside. From the Taylor series expansions and keep the terms up to the order 6, we have

$$a_n = y^{2n+1}\frac{\alpha_{n,n}}{\alpha_{n,d}} = y^{2n+1}\frac{\sum_{\ell=0}^{6}\alpha_{n,n}^{(\ell)}y^{\ell}}{\sum_{\ell=0}^{6}\alpha_{n,d}^{(\ell)}y^{\ell}} \tag{6.18}$$

where the coefficients for the numerator are

$$\alpha_{n,n}^{(0)} = -A_n m_2^{-n-1}m_3^n\frac{(n+1)m_2^2+nm_3^2}{2n+1}, \tag{6.19a}$$

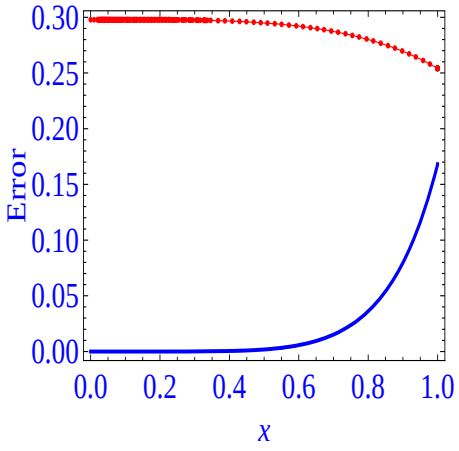

(a) Coefficient A_1.

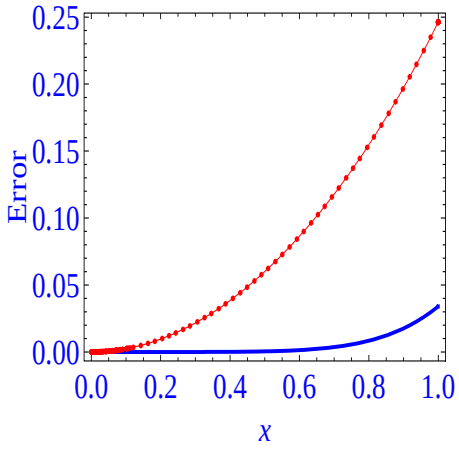

(b) Coefficient A_2.

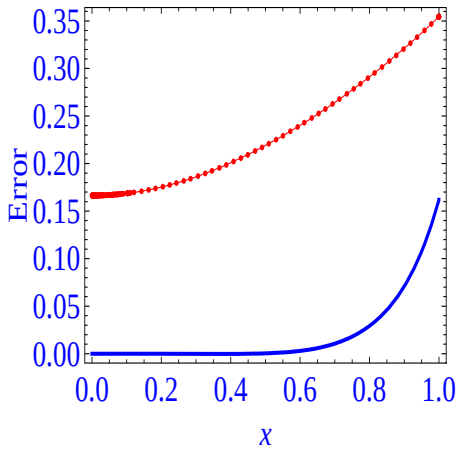

(c) Coefficient B_1.

Figure 6.2: The relative errors of coefficients A_1, A_2, and B_1 obtained in this paper and also in Ref. [59], all compared with the exact solution obtained using the Mie scattering theory. The bullet-dotted curve "– – • – –" denotes the results in [59] while the solid curve "——" stands for the result in this chapter.

$$\alpha_{n,n}^{(1)} = 0, \tag{6.19b}$$

$$\alpha_{n,n}^{(2)} = A_n m_2^{-n-1} m_3^n \left(m_3^2 - m_2^2\right) \times \frac{\left(2n^2+5n+3\right)m_2^2 + n(2n-1)m_3^2}{2\left(8n^3+12n^2-2n-3\right)}, \tag{6.19c}$$

$$\alpha_{n,n}^{(3)} = -\frac{4^{-n}(n+1)\pi m_2^n m_3^n \left(m_2^2 - m_3^2\right)}{(2n+1)^2\Gamma^2\left(n+\frac{1}{2}\right)} y^{2(n-1)}, \tag{6.19d}$$

$$\alpha_{n,n}^{(4)} = A_n m_2^{-n-1} m_3^n \left(m_3^2 - m_2^2\right) \left[(n+1)(2n+3)(2n+5)m_2^4 - 3[4n(n+1)-15]m_3^2 m_2^2 - n[4n(n-2)+3]\, m_3^4\right] / \left[8(4n^2-9)(4n^2-1)(2n+5)\right], \tag{6.19e}$$

$$\alpha_{n,n}^{(5)} = \frac{2^{-2n-1}(n+1)\pi m_2^n m_3^n \left(m_2^4 - m_3^4\right)}{(2n+1)^2(2n+3)\Gamma^2\left(n+\frac{1}{2}\right)} y^{2(n-1)}, \tag{6.19f}$$

$$\alpha_{n,n}^{(6)} = A_n m_2^{1-n} m_3^{n+2} \left[(2n-1)(2n+5)(2n+7)m_2^4 - 2(2n-5)(2n+1)(2n+7)m_3^2 m_2^2 + (2n-5)(2n-3)(2n+3)m_3^4\right] / \left[8(4n^2-25)(4n^2-9) \times (4n^2-1)(2n+7)\right]; \tag{6.19g}$$

while the coefficients for the denominator are

$$\alpha_{n,d}^{(0)} = -\frac{i4^n n}{\pi}\Gamma^2\left(n+\frac{1}{2}\right) A_n m_2^{-n-1} m_3^{-n-1} \times \left(m_2^2 - m_3^2\right), \tag{6.20a}$$

$$\alpha_{n,d}^{(1)} = 0, \tag{6.20b}$$

$$\alpha_{n,d}^{(2)} = -\frac{i2^{2n-3}n}{\pi}(2n-1)\Gamma^2\left(n-\frac{1}{2}\right) A_n \times m_2^{-n-1} m_3^{-n-1}\left(m_2^4 - m_3^4\right), \tag{6.20c}$$

$$\alpha_{n,d}^{(3)} = \frac{y^{2(n-1)} m_2^{-n-1} m_3^{-n-1}}{2n+1}\left\{-i\left[n m_2^2 + (n+1)m_3^2\right] \times m_2^{2n+1} - A_n m_3^{2n+1}\left[(n+1)m_2^2 + n m_3^2\right]\right\},$$

(6.20d)

$$\alpha_{n,d}^{(4)} = -\frac{i2^{2n-3}}{(1-2n)^2(2n-3)\pi}\Gamma^2\left(n+\frac{1}{2}\right)A_n m_2^{-n-1} \times m_3^{-n-1}\left(m_2^2-m_3^2\right)\left\{n(2n-1)m_2^4+2[n(2n-3)+4]m_3^2m_2^2+n(2n-1)m_3^4\right\}, \tag{6.20e}$$

$$\alpha_{n,d}^{(5)} = \frac{y^{2(n-1)}m_2^{-n-1}m_3^{-n-1}}{2(4n^2-1)(2n+3)}\left(m_2^2-m_3^2\right)[i(n+1)(2n+3)m_3^2m_2^{2n+1}+in(2n-1)m_2^{2n+3}-(n+1) \times (2n+3)A_n m_3^{2n+1}m_2^2-n(2n-1)A_n m_3^{2n+3}], \tag{6.20f}$$

$$\alpha_{n,d}^{(6)} = -\frac{i4^{n-4}}{\pi}[4(n-4)n+15]\Gamma^2\left(n-\frac{5}{2}\right)A_n m_2^{1-n} \times \left(m_2^4-m_3^4\right)m_3^{1-n} - \frac{4^{-n-1}(n+1)\pi y^{4(n-1)}m_2^n}{\Gamma^2\left(n+\frac{3}{2}\right)} \times \left(m_2^2-m_3^2\right)m_3^n. \tag{6.20g}$$

These coefficients look complicated, because we considered the general cases of the materials and also the expansion polynomial series up to power 6. They could be significantly simplified, as to be demonstrated later. It should be noted that the expressions of numerator and denominator in (6.18) do not simply follow the power series exactly because the order number n involves also in the power series. For instance, $y^{2(n-1)}$ and $y^{4(n-1)}$ are contained in the intermediate series coefficients, but they will disappear when the first order $n = 1$ is considered. When the second or higher orders are considered, then we have to see if they should be excluded because we basically keep the series expansion up to the order 6.

To see the general variation of the coefficient a_n, we look into the first and dominant coefficient a_1 and plotted their real (in Fig. 6.3(a)) and imaginary (in

Fig. 6.3(b)) parts in Fig. 6.3, of which the real part is directly used to calculate the extinction cross sections. It is shown that they are changing monotonically within the range of the electrical spherical core radius $x \in (0.01, 1.0)$ and the electrical spherical nanoshell radius $y = x + t \in (0.02, 1.4)$ where the spherical nanoshell thickness $t \in (0.01, 0.4)$. As the scattering cross section involves the magnitude, therefore we also consider the magnitude (in Fig. 6.3(c)) and phase (in degrees in Fig. 6.3(d)) variations of the coefficient a_1. It is clearly seen that within the ranges of the physical parameters, these variations are also monotonic. These provide certain sense for the accuracy versus the expansion order of the coefficients, and thus confirm the feasibility of the present work.

Special Case I ($n = 1$)

To simplify the above expression of a_n, we let $n = 1$ but still leave m_3 to be general. Therefore, the following significantly simplified terms are obtained:

$$a_1 = y^3 \frac{\alpha_{1,n}}{\alpha_{1,d}}, \tag{6.21}$$

where

$$\begin{aligned}
\alpha_{1,n} = & -\frac{A_1 m_3}{3}\left(2m_2^2 + m_3^2\right) + \frac{A_1 m_3}{30}\left(-10m_2^4\right. \\
& \left. + 9m_3^2 m_2^2 + m_3^4\right) y^2 - \frac{2m_2^3 m_3}{9}\left(m_2^2 - m_3^2\right) y^3 \\
& - \frac{A_1 m_3}{840}\left(-70m_2^6 + 49m_3^2 m_2^4 + 20m_3^4 m_2^2\right. \\
& \left. + m_3^6\right) y^4 - \frac{m_3}{45}\left(m_2^3 m_3^4 - m_2^7\right) y^5 \\
& + \frac{A_1 m_2^2 m_3^3}{7560}\left(21m_2^4 + 54m_3^2 m_2^2 + 5m_3^4\right) y^6,
\end{aligned} \tag{6.22a}$$

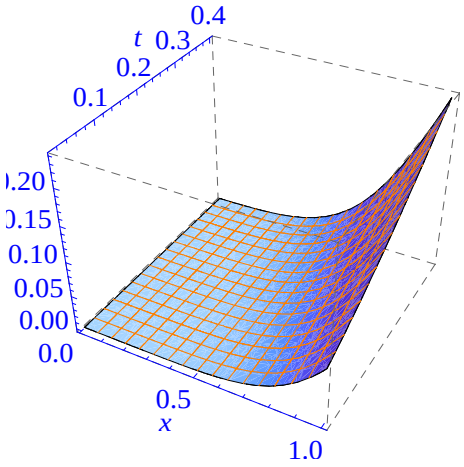

(a) Real part of a_1.

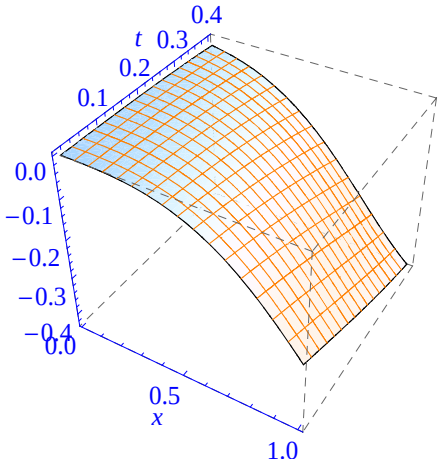

(b) Imaginary part of a_1.

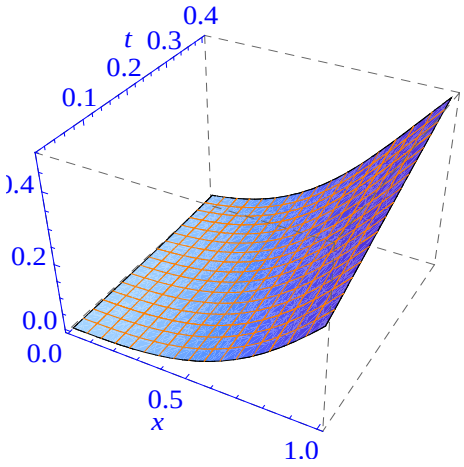

(c) Magnitude of a_1.

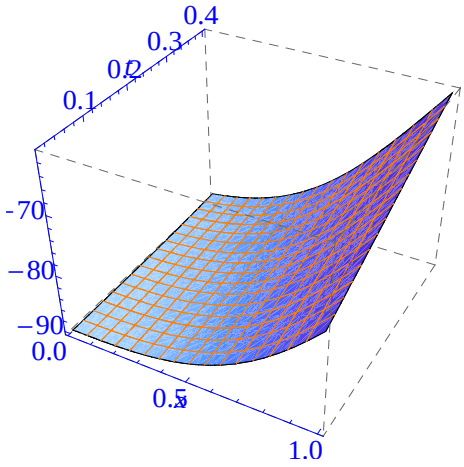

(d) Phase (in degrees) of a_1.

Figure 6.3: The exact coefficient a_1 versus the spherical core radius $x \in (0.01, 1.0)$ and the spherical nanoshell thickness $t \in (0.01, 0.4)$. The other electrical parameters are $\epsilon_1 = (5.44/1.78)\epsilon_0$, $\epsilon_3 = \epsilon_0$, and $\epsilon_2 = (\epsilon_1 + \epsilon_3)/2$ while $\mu_1 = \mu_2 = \mu_3 = \mu_0$.

$$\begin{aligned}\alpha_{1,d} = &+\frac{iA_1}{m_3^2}\left(m_3^2-m_2^2\right)+\frac{iA_1}{2m_3^2}\left(m_3^4-m_2^4\right)y^2\\&-\frac{1}{3}\left(\frac{im_2^5}{m_3^2}+2im_2^3+2A_1m_3m_2^2+A_1m_3^3\right)y^3\\&+\frac{iA_1\left(m_2^6+5m_3^2m_2^4-5m_3^4m_2^2-m_3^6\right)}{8m_3^2}y^4\\&+\frac{i\left(m_2^2-m_3^2\right)}{30m_3^2}\left(m_2^5+10m_3^2m_2^3+10iA_1m_3^3m_2^2\right.\\&\left.+iA_1m_3^5\right)y^5+\frac{1}{36}m_2^2\left[-8m_3m_2^3+8m_3^3m_2\right.\\&\left.-3iA_1\left(m_2^4-m_3^4\right)\right]y^6. \qquad (6.22b)\end{aligned}$$

In (6.21) together with (6.22a) and (6.22b), the intermediate parameter A_1 was defined in (6.9) (where $n = 1$) together with their numerator and denominator defined in (6.12a) and (6.12b), respectively. Please take note that the above specific coefficients in (6.21) given in (6.22a) and (6.22b) can be directly simplified from the expression in 6.18 except for the cancelation of a factor m_2^2 in both denominators of $\alpha_{1,n}$ and $\alpha_{1,d}$. The coefficient a_1 shown in (6.21) together with its intermediate coefficients in (6.22a) and (6.22b) can be simplified by letting $m_3 = 1$, the same as what was done in [59]. Doing so, we could further simplify the expressions.

After the approximate coefficient a_1 is obtained, we may wish to validate it and confirm its accuracy range versus the *electrical* inner radius $x \in (0.01, 1.0)$ and *electrical* outer radius y of the spherical nanoshell. For ease of understanding and calculation, we consider the nanoshell thickness $t \in (0.01, 0.4)$ to represent the outer radius $y = x + t \in (0.02, 1.4)$, as shown in Fig. 6.4. When we consider the relative error limit of 0.68 for the real part of coefficient $\mathrm{Re}[a_1]$, it is seen in Fig. 6.4(a) that the maximum relative error of the present work is below 0.68 while it is much smaller for scientific and engineering applications when the nanocore radius is not

electrically large or when the nanoshell is not electrically thick. At the meantime, we limit the same relative error of 0.68 for the results in [59] and it is seen from Fig. 6.4(b) that the inaccurate area (as cut on the top of the 3D figure) is very large. There is only a small region where the relative error of Re$[a_1]$ in [59] is smaller than 0.68. As the scattering cross section is proportional to the magnitude square of the coefficient, $|a_1|^2$, therefore, we also look into the relative errors of $|a_1|$ in the present paper and also the work in [59], but limit both of them to the allowable errors of 0.15 for engineering applications. It is found from Fig. 6.4(c) and Fig. 6.4(d) that the approximate results produced in this paper are fairly accurate. For the results produced in this paper, there is only a very small inaccurate area with relative error slightly larger than 0.15, as shown in Fig. 6.4(c). For the results published in [59], however, we see in Fig. 6.4(c) that most of the results have relative errors larger than 0.15.

Special Case II ($n = 2$)

Similarly, we could also simplify the above general expression of a_n by letting $n = 2$ to obtain the coefficient a_2. As a result, the following simplified formula is obtained:

$$a_2 = y^5 \frac{\alpha_{2,n}}{\alpha_{2,d}}, \tag{6.23}$$

where

$$\begin{aligned}\alpha_{2,n} = & -\frac{1}{5}A_2 m_3^2\left(3m_2^2+2m_3^2\right)+\frac{1}{70}A_2 m_3^2\left(-7m_2^4\right.\\ & \left.+5m_3^2m_2^2+2m_3^4\right)y^2-\frac{A_2 m_3^2}{2520}\left(63m_2^6-72m_3^2m_2^4\right.\end{aligned}$$

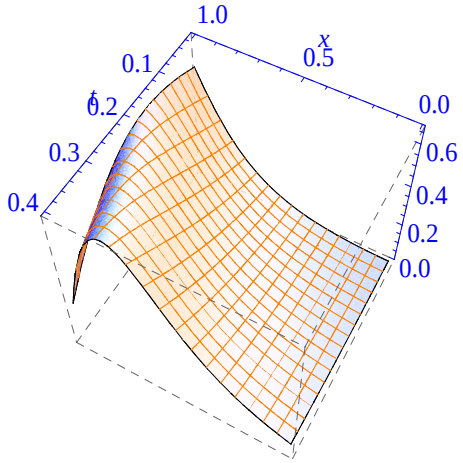

(a) Error of Re$[a_1]$ here.

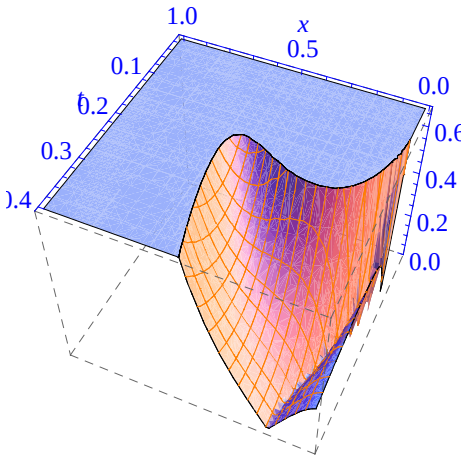

(b) Error of Re$[a_1]$ in [59].

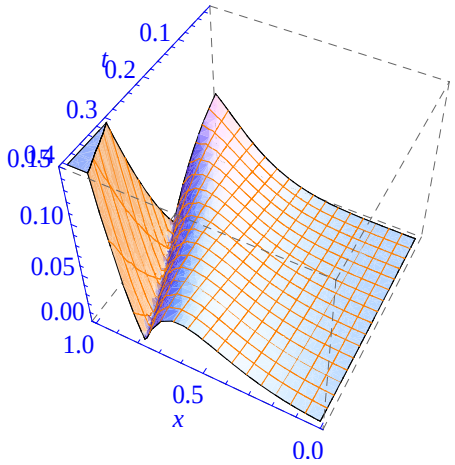

(c) Error of $|a_1|$ here.

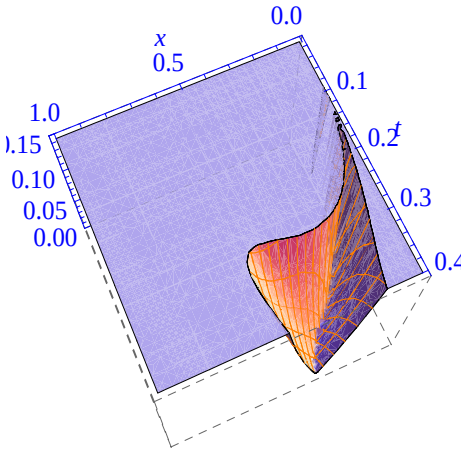

(d) Error of $|a_1|$ in [59].

Figure 6.4: The relative errors of approximate coefficient a_1 formulas derived here in this chapter and in the existing work [59] versus the spherical core radius $x \in (0.01, 1.0)$ and the spherical nanoshell thickness $t \in (0.01, 0.4)$.

$$+7m_3^4m_2^2+2m_3^6\Big)y^4-\frac{1}{75}m_2^5m_3^2\left(m_2^2-m_3^2\right)y^5$$
$$-\frac{A_2m_2^2m_3^4}{83160}\left(297m_2^4+110m_3^2m_2^2-7m_3^4\right)y^6, \tag{6.24a}$$

$$\alpha_{2,d}=\frac{18iA_2}{m_3^3}\left(m_3^2-m_2^2\right)+\frac{3iA_2}{m_3^3}\left(m_3^4-m_2^4\right)y^2+\frac{3iA_2}{4m_3^3}$$
$$\times\left(m_3^2-m_2^2\right)\left(m_2^2+m_3^2\right)^2y^4-\frac{1}{5m_3^3}\left(2im_2^7\right.$$
$$\left.+3im_3^2m_2^5+3A_2m_3^5m_2^2+2A_2m_3^7\right)y^5+\frac{iA_2m_2^2}{4m_3}$$
$$\times\left(m_2^4-m_3^4\right)y^6. \tag{6.24b}$$

In (6.23) together with (6.24a) and (6.24b), the intermediate parameter A_2 was defined in (6.9) (where $n = 2$) together with their numerator and denominator defined in (6.13a) and (6.13b), respectively.

Using this result, we also calculated the absolute values of the coefficient $|a_2|$ and made a comparison on accuracies of the present results and the results published in [59], as shown in Fig. 6.5. It is seen in Fig. 6.5(a) that the coefficient $|a_2|$ is also monotonically changing and its magnitude is much smaller than that of $|a_1|$ by about 10 times especially when the sphere core radius is electrically small or the nanoshell thickness is electrically very thin. Shown also in Fig. 6.5(b) and Fig. 6.5(c) are the comparisons of the relative errors of the approximated a_2 values calculated using the approximate formulas in this paper and also in [59]. It is apparent that when the relative error of 0.15 is kept, the area using the present formulas is much accurate. Because the contribution of $|a_2|$ to the overall values of the extinction and scattering cross sections is only about 10%, so this makes the overall of the present error is even smaller.

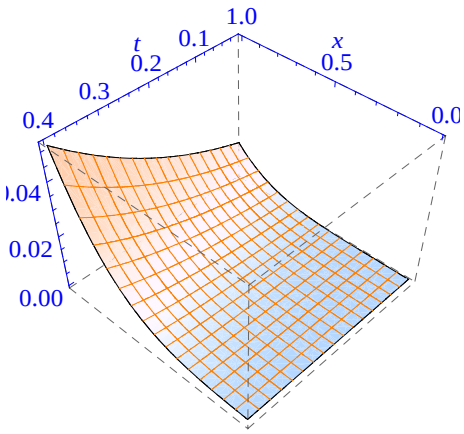

(a) Variation of exact expression $|a_2|$.

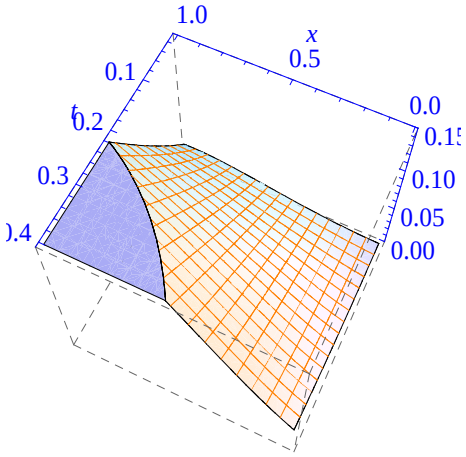

(b) Error of $|a_2|$ here.

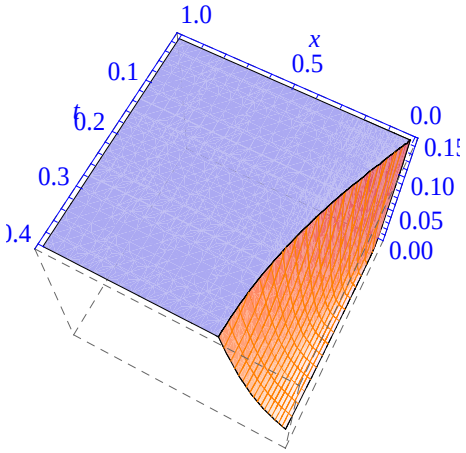

(c) Error of $|a_2|$ in [59].

Figure 6.5: The variation of $|a_2|$ and the relative errors of the formulas derived in this chapter and in the existing work [59] versus the spherical core radius $x \in (0.01, 1.0)$ and the spherical nanoshell thickness $t \in (0.01, 0.4)$.

6.4.2 Approximate Expression of Coefficient b_n

Coefficient b_n

Similarly, the coefficient b_n can be generally derived. However, it is realized that in many papers on nanoparticle scattering formulations, the coefficient b_n is not calculated at all. Nevertheless, the procedure for deriving the coefficients a_n and b_n in (6.4) is the same, also the formula structures for a_n and b_n are the same. Except for the change of the ratio m_3/m_2 in a_n into m_2/m_3 in b_n and the replacement of A_n in a_n by B_n in b_n symbolically, all the other formulations are identical. Therefore, we will not repeat this procedure, but simply provide the useful first order coefficient b_1 for the comparison purpose.

By letting $n = 1$ in (6.4), we have the first term of the coefficient b_n simplified as

$$b_1 = y\frac{\beta_{1,n}}{\beta_{1,d}}, \tag{6.25}$$

where

$$\begin{aligned}\beta_{1,n} = &-\frac{B_1 m_3^2}{m_2} + \frac{B_1 m_3^2}{6m_2}\left(m_3^2 - m_2^2\right)y^2 - \frac{B_1 m_3^2}{120m_2} \\ &\times\left(5m_2^4 - 6m_3^2 m_2^2 + m_3^4\right)y^4 + \frac{1}{45}m_2^2 m_3^2\left(m_3^2\right. \\ &\left.-m_2^2\right)y^5 + \frac{B_1 m_3^2}{15120m_2}\left(105m_2^6 + 63m_3^2 m_2^4\right. \\ &\left.-9m_3^4 m_2^2 + m_3^6\right)y^6, \end{aligned} \tag{6.26a}$$

$$\begin{aligned}\beta_{1,d} = &-\frac{iB_1\left(m_2^2 - m_3^2\right)}{m_2 m_3} - \frac{im_2^3 + B_1 m_3^3}{m_2 m_3}y + \frac{iB_1}{2m_2 m_3} \\ &\times\left(m_2^4 - m_3^4\right)y^2 + \frac{i\left(m_2^2 - m_3^2\right)}{6m_2 m_3}\left(m_2^3 + iB_1 m_3^3\right)y^3\end{aligned}$$

$$- \frac{iB_1}{48m_2m_3}\left(m_2^2 - m_3^2\right)^3 y^4 + \frac{(m_2^2 - m_3^2)}{120m_2m_3}\left(-im_2^5 + 5im_3^2m_2^3 - 5B_1m_3^3m_2^2 + B_1m_3^5\right) y^5 + \frac{1}{45}\left(m_2^2m_3^4 - m_2^4m_3^2\right) y^6. \tag{6.26b}$$

In (6.25) together with (6.26a) and (6.26b), the parameter B_1 was defined in (6.14) ($n = 1$) together with their numerator and denominator defined in (6.17a) and (6.17b), respectively.

To check the accuracy, we have also calculated the coefficient b_1. Shown in Fig. 6.6 are the relative errors of b_1 values computed using the present solution in this paper and the solution in [59]. The parameters used in the calculations are the same as before in Figs. 6.4 and 6.5. It is seen clearly that when the relative error is controlled within 0.45, the area with high accuracy of the results in this paper is very large, as compared with that of the results in [59].

6.5 Discussions and Conclusions

The extinction total cross-section (TCS) is defined as the ratio of the sum of absorbed and scattered energy of incident waves. Mathematically, the extinction total cross-section and the scattering cross section are expressed as

$$Q_{\text{ext}} = \frac{2\pi}{k_0^2}\sum_{n=1}^{\infty}(2n+1)\Re\text{e}[a_n + b_n], \tag{6.27a}$$

$$Q_{\text{sca}} = \frac{2\pi}{k_0^2}\sum_{n=1}^{\infty}(2n+1)\left[|a_n|^2 + |b_n|^2\right]. \tag{6.27b}$$

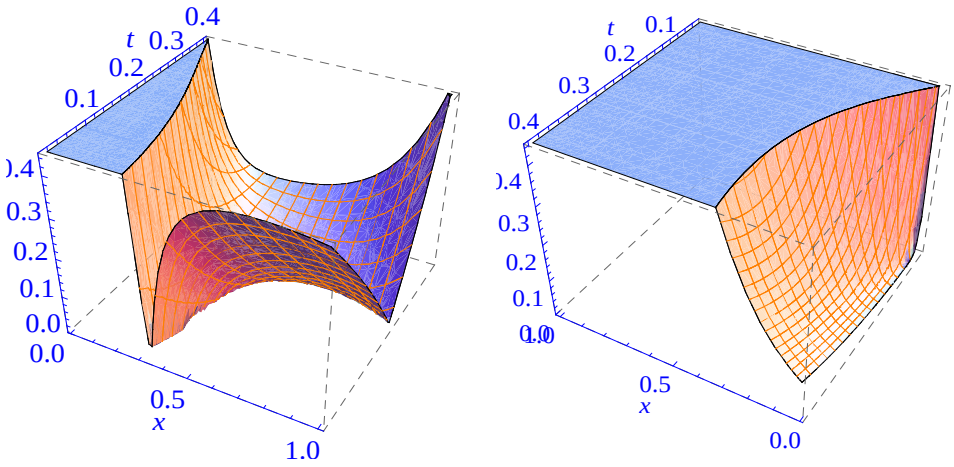

(a) Error of $|b_1|$ here.

(b) Error of $|b_1|$ in [59].

Figure 6.6: The relative errors of the formulas $|b_1|$ derived in this chapter and in the existing work [59] versus the spherical core radius $x \in (0.01, 1.0)$ and the spherical nanoshell thickness $t \in (0.01, 0.4)$.

From this, we could see that the closed form expressions for the extinction cross section and the scattering cross section will be given analytically and approximately as follows:

$$Q_{\text{ext}} \approx \frac{2\pi}{k_0^2} \left[3\Re\text{e}[a_1] + 5\Re\text{e}[a_2] + 3\Re\text{e}[b_1]\right], \tag{6.28a}$$

$$Q_{\text{sca}} \approx \frac{2\pi}{k_0^2} \left[3|a_1|^2 + 5|a_2|^2 + 3|b_1|^2\right]. \tag{6.28b}$$

Apparently, these cross sections are dominated by the value of a_1. The coefficients a_2 and b_1 also contribute to the extinction and scattering cross sections, and their contributions will improve the accuracy of calculating these cross sections although they are much smaller in value.

In summary, we have derived in this chapter a new set of closed form expressions

of the classic Mie scattering coefficients of a spherical nanoshell using a power series up to order 6, which follows closely to the other set in [59]. The derived expressions are very general in nature, because the term number n of the Mie scattering coefficient series is still kept inside for the other potential applications, in addition to the general expressions consisting of the information of the three region electrical parameters (permittivities and permeabilities) and geometrical parameters (the electric inner and outer radii of the structure). This set of approximate expressions is found to be very accurate in the large range of various potential engineering applications including optical nanoparticle characterizations and other nanotechnology applications, validated step by step along the derivation procedure. Computations using this closed form of solutions are very fast and accurate for both lossy and lossless media, but it requires very little effort in the calculations of the cross section results.

Chapter 7

Conclusions and Future Work

In this thesis, a few new methods or concepts are proposed to analyze specifically shaped canonical objects.

Firstly, two new methods are proposed for analysis of radome. One method, which makes use of cylindrical dyadic Green's functions, has been proposed in the study of electromagnetic transmission through a cylindrical radome of non-circular cross sections. The general formulation of this discrete method in the study of a 3-dimensional cylindrical radome of arbitrary cross sections is derived. As an example, this general formulation is then applied to the study of electromagnetic transmission through a 2-dimensional elliptical cylindrical radome shell where the source current of the antenna is considered to be infinite in the $\widehat{z}$-direction. Several cases of this 2-dimensional elliptical cylindrical radome shell have been studied. The numerical results generated by the discrete method for these cases are compared with those obtained by the PWS-SI and the model cylindrical wave-spectrum method

(published in [2] and [70]). From these comparisons, it is concluded that the discrete method is quite accurate.

The other method, which makes use of the spherical dyadic Green's functions (DGF's), is developed to study the electromagnetic transmission through an axil-symmetric radome of superspheroidal shapes. which makes use of cylindrical dyadic Green's functions, has been proposed in the study of electromagnetic transmission through a cylindrical radome of non-circular cross sections. The general formulation of this discrete method in the study of a 3-dimensional cylindrical radome of arbitrary cross sections is derived. However, there is no experimental result available at this moment for the further validity confirmation.

Next, electromagnetic radiation by an infinitely long transmission line analyzed using the dyadic Green's function technique. The transmission line carries a current of constant amplitude but varying phase and is located in the vicinity of an elliptic dielectric waveguide. Wave penetration into, and scattering by, the elliptic waveguide are investigated. The dyadic Green's functions inside and outside of the elliptic waveguide are formulated first in terms of the elliptical vector wave functions which are in turn expressed as Mathieu functions. Using the boundary conditions, we derived a set of general equations governing the scattering and transmitting coefficients of the dyadic Green's functions. From integral equations, the scattered and total electric fields in far-zone are then derived analytically and computed numerically. Different positions of the line source and various medium parameters of the elliptical cylinder are considered and corresponding results are obtained and

discussed.

Then, one of the many possible applications of the spheroidal wave function package is presented in detail, solving an interior boundary value problem. The convenience of coding in Mathematica package is manifested by the ability of this program to find the zeros of functions with complex argument (such as radial functions) simply with one statement. This problem, by itself, is a highly interesting topic. Due to the preoccupation with the more important issue of completing the Mathematica package, the axial symmetry is assumed so as to reduce the complexity of the problems. The more general and practical problem in which the assumption of axial symmetry is removed is a topic worth looking into for future investigations. As indicated in [49], the study of oblate spheroidal cavities can be achieved in a similar way or by symbolic transformation between the oblate and prolate coordinates. However, it should be noted that the assumed axial symmetry is kept in the z-direction and the assumed field components are not changed in the symbolic programming.

Lastly, a new set of closed form expressions of the classic Mie scattering coefficients of a spherical nanoshell using a power series up to order 6, which follows closely to the other set in [59]. The derived expressions are very general in nature, because the term number n of the Mie scattering coefficient series is still kept inside for the other potential applications, in addition to the general expressions consisting of the information of the three region electrical parameters (permittivities and permeabilities) and geometrical parameters (the electric inner and outer radii of the

structure). This set of approximate expressions is found to be very accurate in the large range of various potential engineering applications including optical nanoparticle characterizations and other nanotechnology applications, validated step by step along the derivation procedure. Computations using this closed form of solutions are very fast and accurate for both lossy and lossless media, but it requires very little effort in the calculations of the cross section results.

In my future work, it will be considered that the infinite transmission line carries a current of constant amplitude but varying phase and is located into an elliptic dielectric radome. Numerical results generated by this method will be compared with those obtained by the discrete methods.

Bibliography

[1] J.D.Walton, JR, *Radome Engineering Handbook: Design and Principles*, Marcel Dekker, Inc., New York, 1970.

[2] Jeng-Hwa Chang and Kuan-Kin Chan, "Analysis of a Two-Dimensional Radome of Arbitrarily Curved Surface", *IEEE Transactions on Antennas and Propagation*, vol. AP-38, no. 10, pp. 1565-1568, Oct., 1990.

[3] Herbert L. Hirsch, and Douglas C. Grove, *Practical Simulation of Radar Antennas and Radomes*, Artech House Inc, 1987.

[4] B. Philips, E.A. Parker, and R.J. Langley, "Ray Tracing analysis of the transmission performance of curved FSS" *IEE Proceedings Part H*, vol. 142, no. 3, pp. 193-200, June, 1995.

[5] A. Stanley, E.A. Parker, "Ray tracing fields backscattered from curved dichroic structures", *IEE Proceedings - Microwave, Propagation*, vol. 145, no. 5, pp. 406-410, Oct., 1998.

[6] Georges A. Deschamps, "Ray Techniques in Electromagnetics", *Proceedings of the IEEE*, vol. 60, no. 9, pp. 1022-1035, Sept., 1972.

[7] Prof. E. Arvas, A. Rahhalarabi, U. Pekel, and E. Gundogan, "Electromagnetic transmission through a samll radome of arbitrary shape", *IEE Proceedings Part H*, vol. 137, no. 6, pp. 401-405, Dec., 1990.

[8] James A. Shifflett, "CADDRAD: A Physical Optics Radar/Radome Analysis Code for Arbitrary 3D Geometries", *IEEE Antennas and Propagation Magazine*, vol. 39, no. 6, pp. 73-79, Dec., 1997.

[9] D.M. Elking, J.M. Roedder, D.D. Car, and S.D. Alspach, "A review of high-frequency Radar Cross Section Analysis capabilities at McDonnell Douglas Aerospace", *IEEE Antennas and Propagation Magazine*, vol. 37, no. 5, pp. 33-42, Oct., 1995.

[10] D.C.F. Wu and R.C. Rudduck, "Plane Wave Spectrum - Surface Integration technique for Radome Analysis", *IEEE Transactions on Antennas and Propagation*, vol. AP-22, pp.497-500, May, 1974.

[11] R.C. Rudduck, D.C.F. Wu, and M.R. Inthair, "Near-field Analysis by the Plane Wave Spectrum approach", *IEEE Transactions on Antenna and Propagation*, pp.232-234, Mar., 1973.

[12] J.H. Chang and K.K. Chan, "Analysis of a Two-Dimensional Radome of Arbitrarily Curved Surface", *IEEE Transactions on Antenna and Propagation*, vol. 38, no. 10, pp.1565-1568, Oct., 1990.

[13] Graeme L. James, *Geometrical Theory of Diffraction*, Peter Peregrinus Ltd, 1976.

[14] Richard K. Gordon and Raj Mittra, "Finite Element Analysis of Axisymmetric Radomes", *IEEE Transactions on Antenna and Propagation*, vol. 41, no. 7, pp. 975-980, Jul., 1993.

[15] R.F. Harrington, *Field Computation by Moment Methods*, New York: MacMillan, 1968.

[16] R.C. Hansen, *Moment methods in Antennas & Scattering*, Artech House Inc, 1990.

[17] Korada Umashankar, Allen Taflove, and Sadasiva M. Rao, "Electromagnetic Scattering by Arbitrary Shaped Three-Dimensional Homogeneous Lossy Dielectric Objects", *IEEE Transactions on Antenna and Propagation*, vol. AP34, no. 6, Pg. 758-765, April, 1999.

[18] Giuseppe Mazarella and Giorgio Montisci, "Full-Wave analysis of Dielectric-covered radiatiing series slots", *Microwave and optical technology letters*, vol. 20, no. 1, pp. 67-72, Jan., 1999.

[19] X.J. Huang and Y.W.M. Chia, "The effect of Radome on the transmitted Electromagnetic Field", *IEEE Antenna and Propagation Society International Symposium*, vol. 4, 1998.

[20] Manuel F. Catedra, Emilio Gago, and Luis Nuno, "A Numerical Scheme to obtain the RCS of Three-Dimensional Bodies of Resonant Size Using the Conjugate Gradient Method and the Fast Fourier Transform", *IEEE Transactions on Antenna and Propagation*, vol. 37, no. 5, pp. 528-537, May, 1989.

[21] Cavour Yeh, "The Diffraction of Waves By a Penetrable Ribbon", *Journal of Mathematical Physics*, vol. 4, no. 1, pp. 65-72, Jan., 1963.

[22] J. E. Burke and V. Twersky, "On Scattering of Waves by an Eliptic Cylinder and by a Semielliptic Protuberance on a Ground Plane", *Journal of Optical Society of America*, vol. 54, no. 6, pp. 732-744, Jun., 1964.

[23] Cavour Yeh, "Scattering of Obliquely Incident Light Waves by Elliptical Fibers", *Journal of Optical Society of America*, vol. 54, no. 10, pp. 1227-1231, Oct., 1964.

[24] A-R Sebak, "Electromagnetic Scattering by Two parallel Dielectric Elliptic Cylinders", *IEEE Transactions on Antennas and Propagation*, vol. 42, no. 11, pp. 1521-1527, Nov., 1994.

[25] Minoru Abe and Yasunori Hoshihara and Toshio Sekiguchi, "Scattering Cross Sections of Lossy Dielectric Elliptic Cylinders for Plane Waves", *IECE Trans.Electron.*, vol. E77-C, no. 11, pp. 1759-1764, Nov., 1994.

[26] Kim, Chang Soo, *Scattering of An Obliquely Incident Wave by a Multilayered Elliptical Lossy Dielectric Cylinder*, The Department of Electrical Engineering, Universityof California, Los Angeles, 1989.

[27] Y.-L. Geng, X.-B. Wu, and L.-W. Li, "Analysis of electromagnetic scattering by a plasma anisotropic sphere, *Radio Science*, vol. 38, no. 6, RS1104/pp. 1-12, November/December 2003.

[28] Y.-L. Geng, X.-B. Wu, L.-W. Li and B.-R. Guan, "Mie scattering by an uniaxial anisotropic sphere, *Physical Review E*, vol. 70, no. 5, pp. 056609/1-8, November 1, 2004 .

[29] Y.-L. Geng, X.-B. Wu, L.-W. Li and B.-R. Guan, "Electromagnetic scattering by an inhomogeneous plasma anisotropic sphere of multilayers," *IEEE Trans. Antennas Propagat.*, vol. 53, no. 12, pp. 3982-3989, Dec. 2005.

[30] C.-W. Qiu, L.-W. Li, T. S. Yeo, and S. Zouhdi, "Scattering by rotationally symmetric anisotropic spheres: Potential formulation and parametric studies", *Physical Review E*, vol. 75, no. 2, 026609, January 2007.

[31] W. Sun, N. G. Loeba and Q. Fu, "Light scattering by coated sphere immersed in absorbing medium: a comparison between the FDTD and analytic solutions," *JQSRT*, vol. 83, pp. 483-492, 2004.

[32] B. Stout, C. Andraud, S. Stout and J. Lafait, "Absorption in multiple-scattering systems of coated spheres" *J. Opt. Soc. Am. A*, vol. 20, no. 6, pp. 1050-1059, Jun. 2003.

[33] Z. S. Wu, L. X. Guo, K. F. Ren, G. Gouesbet and G. Gréhan, "Improved algorithm for electromagnetic scattering of plane waves and shaped beams by multilayered spheres," *Appl. Opt.*, vol. 36, no. 21, pp. 5188-5198, Jul. 1997.

[34] F. Xu, X. Cai and K. Ren, "Geometrical-optics approximation of forward scattering by coated particles," *Appl. Opt.*, vol. 43, no. 9, pp. 1870-1879, Mar. 2004.

[35] S. Kawata, *Near-Field and Surface Plasmon Polaritons*, edited, (Springer, Berlin, 2001).

[36] S. Papernov and A. W. Schmid, "Correlations between embedded single gold nanoparticles in SiO_2 thin film and nanoscale crater formation induced by pulsed-laser radiation," *J. Appl. Phys.*, vol. 92, no. 10, pp. 5720-5728, Nov. 2002.

[37] J. R. Krenn, A. Dereux, J. C. Weeber et al., "Squeezing the optical near-field zone by plasmon coupling of metallic nanoparticles ," *Phys. Rev. Lett.*, vol. 82, no. 12, pp. 2590-2593, Mar. 1999.

[38] K. Li, M. I. Stockman, and D. J. Bergman, "Self-similar chain of metal nanospheres as an efficient nanolens," *Phys. Rev. Lett.*, vol. 91, no. 22, pp. 227402 1-4, Nov. 2003.

[39] D. Pines and D. Bohm, "A collective description of electron interactions: II. collective vs individual particle aspects of the interactions," *Phys. Rev.*, vol. 85, no. 2, pp. 338-353, Jan. 1952.

[40] D. Bohm and D. Pines, "A collective description of electron interactions: III. coulomb interactions in a degenerate electron gas ," *Phys. Rev.*, vol. 92, no. 3, pp. 609-625, Nov. 1953.

[41] P. B. Johnson and R. W. Christy, "Optical constants of the noble metals," *Phys. Rev. B*, vol. 6, no. 12, pp. 4370-4379, Dec. 1972.

[42] C.T. Tai, *Dyadic Green's Function in Electromagnetic Theory*, Scranton, PA : Intext Educational, 1971.

[43] W.C. Chew, *Waves and Fields in Inhomogeneous Media*, New York: Van nostrand, 1990.

[44] L.W. Li and P.S. Kooi and M.S. Leong and T.S. Yeo, "On the eigenfunction expansion of dyadic Green's function in planarly stratified media", *Journal of Electromagnetic Waves and Applications*, vol. AP-8, no. 8, pp. 663-678, Aug., 1994.

[45] L.W. Li and P.S. Kooi and M.S. Leong and T.S. Yeo, "Electromagnetic Dyadic Green's Function in Spherically Multilayered Media", *IEEE Transactions on Microwave Theory and Techniques*, vol. MTT-42, no. 12, pp. 2302-2310, Dec., 1994.

[46] L.W. Li and P.S. Kooi and M.S. Leong and T.S. Yeo, "Analytic representation of scattering dyadic Greens functions coefficients for cylindrically multilayered chiral media", *J. Electromagn. Waves Appli.*, vol. 9, no. 9, pp. 12071221, Spt. 1995

[47] C.T. Tai, *Dyadic Green's Function in Electromagnetic Theory*, Scranton, PA : Intext Educational, 1971.

[48] Collin, R.E., *Field Theory of Guided Waves*, IEEE Press, Piscataway, New Jersey, The 2nd, 1991.

[49] Le-Wei Li and Xiao-Kang Kang and Mook-Seng Leong, *Spheroidal Wave Functions in Electromagnetic Theory*,Wiley, New York, pp. 320, November, 2001.

[50] Le-Wei Li and Pang-Shyan Kooi and Mook-Seng Leong and Tat-Soon Yeo, "On the eigenfunction expansion of dyadic Green's function in planarly stratified media", *J. Electromagn. Waves Applic.*, vol. 8, no. 6, pp. 663-678, June, 1994.

[51] Le-Wei Li and Mook-Seng Leong and Tat-Soon Yeo and Pang-Shyan Kooi, "Electromagnetic Dyadic Green's Functions in Spectral Domain for Multilayered Cylinders", vol. 14, no. 7, pp. 961-986, July, 2000.

[52] Le-Wei Li and Pang-Shyan Kooi and Mook-Seng Leong and Tat-Soon Yeo, "Electromagnetic dyadic Green's function in spherically multilayered media", *IEEE Trans. Microwave Theory Tech.*, vol. 42, no. 12, pp. 2302-2310, Dec., 1994.

[53] Le-Wei Li and Mook-Seng Leong and Yeqin Huang, "Electromagnetic Radiation of Antennas in the Presence of an Arbitrarily Shaped Dielectric Object: Green Dyadics and Their Applications", *IEEE Transactions on Antennas and Propagation*, vol. 49, no. 1, pp. 84-90, Jan., 2001.

[54] Le-Wei Li and Mook-Seng Leong and Pang-Shyan Kooi and Tat-Soon Yeo, "Spheroidal vector eigenfunction expansion of dyadic Green's functions for a dielectric spheroid", *IEEE Trans. Antennas Propagt.*, vol. 49, no. 4, pp. 645-659, Apr., 2001.

[55] Le-Wei Li and Xiao-Kang Kang and Mook-Seng Leong and Pang-Shyan Kooi and Tat-Soon Yeo, "Electromagnetic dyadic Green's functions for multilayered spheroidal structures: I-Formulation", *IEEE Trans. Microwave Theory Tech.*, vol. 49, no. 3, pp. 532-541, Mar., 2001.

[56] C. Flammer, *Spheroidal wave functions*, Stanford Univ. Press, California, 1957.

[57] J.A. Stratton, P.M. Morse, L.J. Chu, J.D.C. Little, and F.J. Corbato, *Spheroidal wave functions*, John Wiley & Sons, New York, 1956.

[58] G. C. Kokkorakis and J. A. Roumeliotis, "Electromagnetic eigenfrequencies in a spheroidal cavity.", *J. Electromagn. Waves Appl.*, vol. 11, pp. 279–292, 1997.

[59] M. Alam and Y. Massoud, "A closed-form analytical model for single nanoshells", *IEEE Trans. Nanotech.*, vol. 5, no. 3, pp. 265-272, May 2006.

[60] S. Oldenburg, R. D. Averitt, S. Westcott, and N. J. Halas, "Nanoengineering of Optical Resonances", *Chem. Phys. Lett.*, vol. 288, pp. 243, 1998.

[61] Surbhi Lal, Stephan Link and Naomi J. Halas, "Nano-optics from sensing to waveguiding", *Nature Photonics*, vol. 1, pp. 641-648, 2007.

[62] Narayanan Subramaniam, "Wave Propagation Through Curved Shells and the Validity of the Plan – Stab Approximation", *IEEE Transactions on Antennas and Propagation*, vol. 39, no. 9, pp. 1265-1271, Sept., 1991.

[63] Pinchas D. Einziger and Leopold B. Felsen, "Rigorous Asymptotic Analysis of Transmission Through a Curved Dielectric Slab", *IEEE Transactions on Antennas and Propagation*, vol. AP-31, no. 6, pp. 863-870, Nov., 1983.

[64] Pinchas D. Einziger and Leopold B. Felsen, "Ray Analysis of Two-Dimensional Radomes", *IEEE Transactions on Antennas and Propagation*, vol. AP-31, no. 6, pp. 870-884, Nov., 1983.

[65] E. Arvas and A. Rahhalarabi and U. Pekel and E. Gundogan, "Electromagnetic Transmission Through a Small Radome of Arbitrary Shape", *Proc. Inst. Elect. Eng.*, vol. 137, no. 6, pp. H, Dec., 1990.

[66] E. Arvas and E. Gundogon, "Electromagnetic Transmission Through a Small Radome of Arbitrary Shape", *Technical Report TR-90-3*, Department of Electrical and Computer Engineering and The New York Center for Advanced Technology in Computer Application and Software (CASE), Syracuse Universityyear, 1990.

[67] D.C.F. Wu and R.C. Rudduck, "Plane Wave Spectrum – Surface Integration Technique for Radome Analysis", *IEEE Transactions on Antennas and Propagation*, vol. AP-22, no. 5, pp. 497-500, May, 1974.

[68] Richard K. Gord0n and Raj Mittra, "Finite Element Analysis of Axisymmetric Radomes", *IEEE Transactions on Antennas and Propagation*, vol. AP-41, no. 7, pp. 975-981, Jul., 1993.

[69] Demetrius T. Paris, "Computer-Aided Radome Analysis", *IEEE Transactions on Antennas and Propagation*, vol. AP-18, no. 1, pp. 7-15, Jan., 1970.

[70] Jiin-Chiou Jeng, *Electromagnetic Transmission Effect Through a Elliptical Dielectric Shell*, The Institute of Communication College of Engineering, National Chiao Tung University, Taiwan, 1985.

[71] P.L. Overfelt, "Superspheroids: A new family of Radome Shapes", *IEEE Transactions on Antennas and Propagation*, vol. 43, no. 2, Dec., 1995.

[72] Constantine A. Balanis, *Antenna Theory : Analysis and Design*, John Wiley and Sons Inc, 1997.

[73] L.W. Li, M.S. Leong, P.S. Kooi, and T.S. Yeo, "Electromagnetic Dyadic Green's Function in Spherically Multilayered Media", *IEEE Transactions on Microwave Theory and Techniques*, vol. 42, no. 12, pp. 2302-2310, Dec., 1994.

[74] Tapan K. Sarjar, "A Note on the Choice Weighting Functions in the Methods of Moments", *IEEE Transactions on Antenna and Propagation*, vol. AP-33, no. 4, April, 1985.

[75] Tapan K. Sarjar, Antonije R. Djordjevic, and Ercument Arvas, "On the choice of Expansion and Weighting Functions in the Numerical Solution of Operator Equations", *IEEE Transactions on Antenna and Propagation*, vol. AP-33, no. 9, Sep., 1985.

[76] Wei-Jiang Zhao, Le-Wei Li, Yeow-Beng Gan, "Efficient analysis of antenna radiation in the presence of airborne dielectric radomes of arbitrary shape", *IEEE Transactions on Antennas and Propagation*, vol. 53, no. 1, pp. 442-449, Jan. 2005.

[77] The Computational Laboratory of the National Applied Mathematics Laboratory National Bureau of Standards, *Tables Relating To Mathieu Functions*, New York: Columbia University Press, 1951.

[78] McLachlan N.W., *Theory and Application of Mathieu Functions*, Oxford,Clarendon Press, 1947.

[79] J. A. Stratton and P. M. Morse and L. J. Chu and R. A. Hunter, *Elliptic Cylinder and Spheroidal Wave Functions*, New York: John-Wiley and Sons Inc., 1941.

[80] P. Moon and D.E. Spencer, *Field Theory Handbook*, Springer-Verlag, Berlin, The 3rd edition, 1988.

[81] G. C. Kokkorakis and J. A. Roumeliotis, "Electromagnetic eigenfrequencies in a spheroidal cavity: calculation by spheroidal eigenvectors.", *J. Electromagn. Waves Appl.*, vol. 12, pp. 1601–1624, 1998.

[82] M. Born and E. Wolf, *Principles of Optics*, edited, (Cambridge University Press, Cambride, 1999).

[83] R. G. Grainger, J. Lucas, G. E. Thomas, and G. B. L. Ewen, "Calculation of Mie derivatives," *Appl. Opt.*, vol. 43, no. 28, pp. 5386-5393, Oct. 2004.

[84] C. F. Bohren and D. E. Huffman, *Absorption and Scattering of Light by Small Particles*, edited, (Wiley, New York, 1983).

[85] H. C. Van De Hulst, *Light Scattering by Small Particles*, edited, (Dover, New York, 2000).

[86] A. L. Aden and M. Kerker, "Scattering of electromagnetic waves from two concentric spheres," *J. Appl. Phys.*, vol. 22, no. 10, pp. 1242-1246, Oct. 1951.

[87] R. Bhandari, "Scattering coefficients for a multilayered sphere: analytic expressions and algorithms," *Appl. Opt.*, vol. 24, no. 13, pp. 1960-1967, Jul. 1985.

[88] B. R. Johnson, "Light scattering by a multilayer sphere," *Appl. Opt.*, vol. 35, no. 18, pp. 3286-3296, Jun. 1996.

[89] L.-W. Li, D. You, M.-S. Leong, and J. A. Kong, "Electromagnetic scattering by an inhomogeneous chiral sphere of nonlinear varying permittivity: A discrete analysis using multilayered model (Abstract), *J. Electromagn. Waves Applic.*, vol. 13, no. 9, pp. 12031205, September 1999, The full text appears in *Progress In Electromagnetics Research*, vol. 23, pp. 237-261, 1999, EMW Publishing: Cambridge, Boston.

[90] L.-W. Li, D. You, M.-S. Leong, and J. A. Kong, "Plane wave scattering by an achiral sphere in an infinitely extended chiral host medium (Abstract), *J. Electromagn. Waves Applic.*, vol. 15, no. 8, pp. 10431045, August 2001, The full content appears in, *Progress In Electromagnetics Research*, vol. 33, pp. 261-298, 2001, EMW Publishing: Cambridge, Boston.

[91] M. Kerker, *The Scattering of Light and Other Electromagnetic Radiation*, edited, (Academic, New York, 1969).

[92] L.-W. Li, P.-S. kooi, M.-S. Leong and T.-S. Yeo, "Electromagnetic dyadic Green's function in spherically multilayered media," *IEEE Trans. Microwave Theory Tech.*, vol. 42, no. 12, pp. 2302-2310, Dec. 1994, Part A.

[93] L.-W. Li, M.-S. Leong, P.-N. Jiao, and W.-X. Zhang, Analysis of a passive circular loop antenna radiating in the presence of a layered chiral sphere using method of moments, *J. Electromagn. Waves Applic.*, vol. 16, no. 11, pp. 1593-1611, November 2002 .